Propagation of Coronal Mass Ejections in the Interplanetary Space

（惑星間空間中でのコロナ質量放出の伝搬）

Tomoya Iju
伊集 朝哉

A Dissertation for the Degree of Doctor of Science

Graduate School of Science
Nagoya University

January 2015

Abstract

Coronal mass ejections (CMEs) are a transient phenomenon in which a large mass of magnetized coronal plasma is expelled from the Sun into the interplanetary space and propagate through the solar wind which is a continuous outflow of the solar corona. Because Earth-reached CMEs are the main driver of intense geomagnetic storms to affect the operation of satellite, radio communication, and power grid, the understanding of their propagation is very important for the space weather forecasting to predict when a geomagnetic disturbance begins. To achieve this goal, we investigate the interplanetary propagation of CMEs in the inner heliosphere during 1997 – 2011. By comparing observations from a space-borne coronagraph, interplanetary scintillation at 327 MHz, and plasma spectrometers on satellites, we identify 46 interplanetary CMEs (ICMEs) which could be tracked from the Sun to the Earth. We examine kinematic properties of 15 fast ($V_{\rm SOHO} - V_{\rm bg} > 500$ km s^{-1}), 25 moderate (0 km s$^{-1} \leq V_{\rm SOHO} - V_{\rm bg} \leq 500$ km s^{-1}), and 6 slow ($V_{\rm SOHO} - V_{\rm bg} < 0$ km s^{-1}), where $V_{\rm SOHO}$ and $V_{\rm bg}$ are the initial speed of ICMEs and the speed of the ambient solar wind, respectively. Examinations of their kinematics yield the following results: i) Fast ICMEs rapidly decelerate, moderate ICMEs show a little decelerating motion, and slow ICMEs accelerate, and their radial speeds converge on the speed of the solar wind during their outward propagation. ii) The acceleration and deceleration are nearly complete by 0.34 ± 0.03 and 0.79 ± 0.04 astronomical units from the Sun, respectively, and those are ended when the ICMEs reach 479 ± 126 km s^{-1}. These results support the assumption that the radial motion of ICMEs is affected by the drag force(s) due to interaction with the solar wind. From comparison between drag force models and observations, we find that a linear drag model $a = -\gamma_1(V - V_{\rm bg})$ with $\gamma_1 = 6.58\ (\pm 0.23) \times 10^{-6}$ s^{-1} gives a good approximation for the kinematics of ICMEs with 0 km s$^{-1} \leq V - V_{\rm bg} < 1000$ km s^{-1}, where a and V are the acceleration and radial speed of ICMEs, respectively, while a quadratic drag model $a = -\gamma_2(V - V_{\rm bg})|V - V_{\rm bg}|$ with $\gamma_2 = 2.36\ (\pm 1.13) \times 10^{-11}$ m^{-1} is appropriate for describing the motion of slow ICMEs. From a careful examination, we find a modified drag equation $a = -2.07 \times 10^{-12}(V - V_{\rm bg})|V - V_{\rm bg}| - 4.84 \times 10^{-6}(V - V_{\rm bg})$ for the kinematics of the fast and moderate ICMEs. From the viewpoint of fluid mechanics, we interpret this equation as indicating that massive ICMEs ($10^{12} - 10^{13}$ kg) with 0 km s$^{-1} \leq V - V_{\rm bg} < 2300$ km s^{-1} are controlled mainly by the hydrodynamic Stokes drag force, while the aerodynamic drag force is a predominant factor for more faster ICMEs.

Acknowledgements

I would like to express my sincere gratitude to my supervisor, Professor Munetoshi Tokumaru, for the continuous support of my doctoral study, for his great patience, encouragement, deep knowledge, and informative discussion in connection with my research. Professor Tokumaru introduced me to the radio scintillation theory, remote sensing technique of interplanetary scintillation (IPS), and many interesting topics of the solar-terrestrial physics. His appropriate guidance greatly helped me in all the time of research and writing of this thesis. I would like to greatly acknowledge the other members of the advisory committee on my dissertation, Professor Kanya Kusano and Associate Professor Satoshi Masuda in the Solar-Terrestrial Environment Laboratory (STEL) and Associate Professor Takeru Suzuki in the Laboratory of Theoretical Astronomy and Astrophysics, Nagoya University for their valuable commets on this dissertation. I offer my sincere appreciation to Assistant Professor Ken'ichi Fujiki for teaching the computer programing and giving many piece of advice and the continuous support of my study. I would like to express my appreciation to Emeritus Professor Masayoshi Kojima for his helpful comments and discussion on my research. I would like to acknowledge the engineering support of Mr. Kazuo Maruyama and Mr. Yasushi Maruyama who maintain radio telescopes and associated equipment for STEL IPS observations.

I offer my sincere appreciation to Professor Bernard V. Jackson in the University of California, San Diego, for his informative discussion, fruitful suggestions on my research, and for useful comments in revision of my published article. I would like to express my gratitude to I would like to express my appreciation to Professor Kiyoto Shibasaki and Dr. Kazumasa Iwai in the Nobeyama Solar Radio Observatory, National Astronomical Observatory of Japan, Professor Kazuyuki Hakamada in Chubu University, Dr. Haruichi Washimi in the Center for Space Plasma and Aeronomic Research, the University of Arabama, Huntsville, and Dr. Daikou Shiota in STEL for giving many interesting topics of the solar physics and for insightful suggestions on my research. I would like to express my gratitude to Professor Periasamy K. Manoharan in the Tata Institute of Fundamental Research, Professor Juan Americo Gonzalez-Esparza in el Instituto de Geofísica, Universidad Nacional Autónoma de México, Dr. Neel Savani in the Naval Research Laboratory, and Dr. Hsiu-Shan Yu in the University of California, San Diego, for their valuable discussions and suggestions. I offer my appreciation to Professor Tomoko Nakagawa in Tohoku Institute of Technology for helpful comments on my study.

I wish to acknowledge Ms. Junko Okaniwa and Ms. Shigemi Nakagawa for their office working. I wish to thank labmates and senior and junior members in STEL, Ms. Ayako Sawazaki (Tempōrin), Mr. Hiroaki Higasihoka, Dr. Tetsuya Yamamoto, Dr. Yūji Tsuji, Dr. Manabu Yagi, Dr. Hiroaki Ito, Dr. Yūya Nagai, Dr. Fusa Miyake, Dr. Satoshi

Kurita, Dr. Naritoshi Kitamura, Mr. Momotaro Noda, Ms. Maria Hirota, Ms. Mai Ōuchi, Ms. Yumi Bamba, Mr. Kouki Arimi, Mr. Tomoya Shimoyama, Mr. Daiki Satonaka, and Mr. Hirofumi Nakano for their friendship at STEL, helpful discussions and enjoyable conversations. I also thank other persons who are working in STEL.

The IPS observations were carried out under the solar wind program of the Solar-Terrestrial Environment Laboratory (STEL), Nagoya University. The IPS observations were supported by the Inter-university Upper Atmosphere Global Observation Network (IUGONET) project by the Ministry of Education, Culture, Sports, Science, and Technology (MEXT), Japan. I am thankful to scientists and engineers of the *Solar and Heliospheric Observatory* (SOHO) spacecraft for use of coronal mass ejection (CME) images obtained by the *Large Angle and Spectrometric Coronagraph* (LASCO) onboard SOHO. SOHO is a project of international cooperation between the European Space Agency (ESA) and National Aeronautics and Space Administration (NASA). I acknowledge use of the SOHO/LASCO CME catalog; this CME catalog is generated and maintained at the CDAW Data Center by NASA and the Catholic University of America in cooperation with the Naval Research Laboratory. I thank Space Physics Data Facility of NASA/Goddard Space Flight Center (GSFC) for use of the OMNIWeb service and OMNI data. I thank the IDL Astronomy User's Library for the use of IDL software. I acknowledge I. G. Richardson and H. V. Cane for use of the comprehensive ICME catalog. An original map of Chūbu region in Japan used in Chapter 1 is adopted from the web page "Sekai Chizu". I am thankful to S. Gunn and S. Patel for providing a LaTeX template of doctoral thesis. This work was supported by Grant-in-Aid for the Nagoya University Global COE Program "Quest for Fundamental Principles in the Universe: From Particles to the Solar System and the Cosmos" from the Japan Society for the Promotion of Science and MEXT, Japan.

Finally, I would like to express my deep appreciation to my parents, Tomotoshi and Keiko Iju, for their continuous support and encouragement throughout my student life.

Contents

List of Figures

List of Tables

To my parents, and to precious others of mine

Chapter 1

Introduction

The Sun emits not only electromagnetic waves including the visible light, radio wave, and X-ray but also the magnetized plasma in all directions at any time. This continuous outflow of plasma is called the solar wind. The solar wind is disturbed occasionally by blasts called coronal mass ejections (CMEs). CMEs are a transient event in which large amounts of magnetized plasma are expelled from the solar corona. CMEs move outward from the Sun through the solar wind. Because some of them reach the Earth and often cause intense geomagnetic disturbances, the understanding of their propagation is very important for the space weather forecasting. From a large number of satellite-based and ground-based observations for the last several decades, it has been suggested that the interplanetary propagation of CMEs is affected by the interaction with the solar wind. In this chapter, we review the current knowledge of the solar wind, CMEs, and their associated solar activities and observations as the bases of our study, and introduce the outline of this dissertation.

1.1 The Solar Wind

1.1.1 Brief History of the Solar Wind

An idea that a continuous emission of substance from the Sun was proposed by some scientists in the late 19th century. One of them, the Norwegian physicist K. Birkeland argued this hypothesis from the research on the Northern Lights. In 1901, Birkeland constructed a vacuum chamber with a magnetized sphere and performed discharge experiments using that in his laboratory, which named "terrella" experiments (Egeland, 2009). From these experiments, Birkeland (1908) suggested that electric corpuscle rays

emitted from the Sun to the interplanetary space and then they made the Aurora Borealis by an interaction with the Earth's magnetosphere. He also imagined that such rays originated in the region surrounding sunspots and formed narrow streams; these were different from the current description of the solar wind. This corpuscle-flow hypothesis did not be accepted at the community of physicists in those days, and appeared again in the 1950s (Meyer-Vernet, 2007). The comet have two kind of tail called the dust tail and ion tail, respectively; the former consists of the dust grains while the latter is made of the ionized gas. In the 1940s, the cometary ion-tail was well known to be oriented away from the Sun with a deviation angle of less than 10° between the tail axis and Sun–comet line (Hoffmeister, 1943). Furthermore, it was also known that the internal structure of the ion tail such as rays or jets requires the electrodynamic forces to explain its shape (see Wurm, 1968 and references therein). From these, Biermann (1951) suggested that the cometary ion-tail was produced by the charged particle emission from the Sun. Because the comet's orbit passed at all heliolatitudes and the ion tail was observable during approaching the Sun, it was verified that the Sun is emitting charged particles in all direction at any time (Antrack et al., 1964). At around the same time, an upper limit of electron density in the interplanetary space was estimated to be $8 \times 10^2 - 1 \times 10^3$ cm^{-3} at one astronomical unit (AU) from the observation of zodiacal light (Whipple and Gossner, 1949). These studies brought a new view of the interplanetary space.

On the other hand, a research on the solar corona gave a different conclusion. The solar corona is the outer atmosphere of the Sun. Grotrian (1933; 1939) and Edlén (1943) found that spectral lines at 530.3 nm and 637.4 nm in coronal spectra were emitted from highly ionized atoms, namely the Fe XIV and Fe X, respectively. Here, the Fe XIV and Fe X represent the thirteenth-order and the ninth-order charged ions of iron, respectively. Existence of these ions indicates that the corona has a high temperature of $\approx 10^6$ K (Miyamoto, 1949). Figure 1.1 shows variations of the temperature and number density with height in the chromosphere, transition region, and corona. As shown in this figure, the temperature of solar atmosphere rapidly increases from $\approx 10^4$ K at the chromosphere corresponding to the inner atmosphere of the Sun to 10^6 K at the corona through the thin transition region. Under the such high temperature, the hydrogen gas being the primary component of the Sun is fully ionized, and then becomes the plasma, which is a proton-electron mixture. The thermal conductivity of coronal plasma reaches $\approx 10^4$ W m^{-1} K^{-1} (Meyer-Vernet, 2007), which is two orders of magnitude higher than the thermal conductivity of the brass at room temperature. Because of the high thermal conductivity, the corona have a small temperature gradient. The British physicist S. Chapman and his colleague calculated the thermal conductivity and the distance dependence of coronal temperature in an ideal corona comprising protons and electrons with the same number density (Chapman and Zirin, 1957). They also

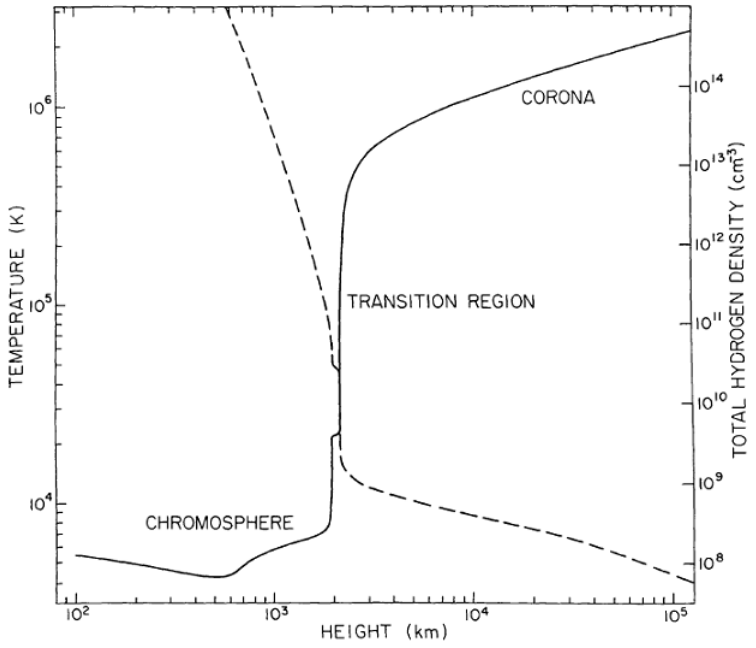

FIGURE 1.1: The temperature and density variations of ionized material with height in the solar chromosphere, transition region, and corona (adopted from Withbroe and Noyes, 1977).

calculated variations of the pressure and number density by assuming a static equilibrium of the ideal corona. From these calculations, they found exponential decreases of the pressure and density with an increase of distance and finite limits of those, which were three orders of magnitude or more larger than the interstellar medium (e.g. Spitzer, 1941). They also suggested that the coronal temperature variation with the solar activity caused an outward or inward movement of the coronal plasma. The Chapman's solution did not show the continuous flow of the ionized gas from the Sun.

The American physicist E. N. Parker also examined the hydrostatic equilibrium of the solar corona, and then found that it was not possible for the solar corona because a gas pressure in the static equilibrium could not balance the interstellar gas pressure. Therefore, Parker (1958a) claimed that the solar corona was stationary expanding. He solved equations of mass conservation and momentum for an isothermal and spherically symmetric corona, and revealed that the coronal plasma was flowing steadily into the interplanetary space with a radial velocity of 450 km s^{-1} at the Earth's orbit. The constant expansion of the solar corona was consistent with not only the charged particle emission proposed by Birkeland and Biermann but also the requirement in which the terminal pressure should balance the interstellar gas pressure. This continuous outward flow of the coronal plasma was named the "solar wind" (Parker, 1958b).

1.1.2 Fundamental Concept of the Solar Wind

From a viewpoint of the fluid dynamics, the solar corona obeys the following set of equations for the conservation of mass and momentum:

$$\frac{1}{r^2}\frac{\mathrm{d}}{\mathrm{d}r}r^2 N m_\mathrm{p} V_\mathrm{bg}(r) = 0, \tag{1.1}$$

and

$$N m_\mathrm{p} V_\mathrm{bg}(r)\frac{\mathrm{d}V_\mathrm{bg}(r)}{\mathrm{d}r} = -\frac{\mathrm{d}p}{\mathrm{d}r} - G\frac{N m_\mathrm{p} M_\odot}{r^2}, \tag{1.2}$$

where N, m_p, r and $V_\mathrm{bg}(r)$ are the number density, mass of proton, radial distance from the solar center, and the flow speed, respectively, p is the pressure, G is the gravitational constant, and $M_\odot$ is the solar mass. Because the mass of electron is about eighteen hundred times smaller than the proton, the contribution of electrons to the total mass of plasma is negligible. Here, the solar corona is assumed to be in the spherical symmetry, and then its physical properties are functions of r only. In addition to this, the Lorentz force is ignored in Equation (1.2). If $V_\mathrm{bg}(r) = 0$, which satisfies Equation (1.1), Equation (1.2) describes the hydrostatic equilibrium. However, this solution yields an unrealistic pressure of the interplanetary medium at infinity as shown by Chapman and Zirin (1957).

On the other hand, $r^2 N m_\mathrm{p} V_\mathrm{bg}(r) = C$, where C is a constant which is non-zero, is also applicable to Equations (1.1). It is multiplies by 4π to obtain

$$4\pi r^2 N m_\mathrm{p} V_\mathrm{bg}(r) = I, \tag{1.3}$$

where I is just the mass flux through the sphere with r. The plasma pressure is given by $p = 2Nk_\mathrm{B}T$, where k_B and T are the Boltzmann constant and coronal temperature, respectively, because protons and electrons are assumed to have the same density and temperature in the ideal corona (Hundhausen, 1995). Substituting these expressions into Equation (1.2) with the weaker distance dependence of plasma temperature in the corona, the momentum equation is modified as follows:

$$\left[V_\mathrm{bg}(r)^2 - \frac{2k_\mathrm{B}T}{m_\mathrm{p}}\right]\frac{1}{V_\mathrm{bg}(r)}\frac{\mathrm{d}V_\mathrm{bg}(r)}{\mathrm{d}r} = \frac{4k_\mathrm{B}T}{m_\mathrm{p}r} - \frac{GM_\odot}{r^2}. \tag{1.4}$$

This equation was found by Parker (1958a) as describing the stationary expansion of the solar corona. For any realistic quantity of T, the right-hand side of Equation (1.4) retains negative between the base of the corona and the critical radius

$$r_\mathrm{c} = \frac{GM_\odot m_\mathrm{p}}{4k_\mathrm{B}T}, \tag{1.5}$$

and becomes positive at a larger distance than that. This fact means that the coronal plasma lying below r_c is gravitationally bound, while a parcel of charged particles being above that may escapes from the Sun against the solar gravity. If $V_{bg}(r)$ satisfies the equation

$$V_{bg}(r)^2 - \frac{2k_B T}{m_p} \begin{cases} < 0 & \text{at } r < r_c \\ = 0 & \text{at } r = r_c, \\ > 0 & \text{at } r > r_c \end{cases} \tag{1.6}$$

$dV_{bg}(r)/dr$ maintains positive anywhere, namely the velocity of charged particles can continue to increase with the heliocentric distance. With this condition, Equation (1.4) is solved as (Hundhausen, 1995):

$$V_{bg}(r)^2 - \frac{2k_B T}{m_p} - \frac{2k_B T}{m_p} \ln\left(\frac{m_p V_{bg}(r)^2}{2k_B T}\right) = \frac{8k_B T}{m_p} \ln\left(\frac{r}{r_c}\right) + 2GM_\odot \left(\frac{1}{r} - \frac{1}{r_c}\right). \tag{1.7}$$

This is the solar wind solution. Figure 1.2 shows variations of $V_{bg}(r)$ derived from Equation (1.7) with various values of T. From this figure, one may find that the solar wind driven by the thermal energy only has its velocity range from 550 to 800 km s^{-1} around the Earth's orbit for the realistic coronal temperature between 1.0×10^5 and 2.0×10^6 K. Equation (1.7) also shows a rapid acceleration of the coronal plasma stream in the near-Sun region below 2.0×10^7km and a gradual increasing of the flow speed in the interplanetary space in Figure 1.2. As the radial distance becomes larger, the number density reaches asymptotically zero because of Equation (1.3) with the mass flux conservation. Hence, the plasma pressure also approaches zero with an increase in distance. The solar wind solution satisfies a request that the coronal plasma pressure must be equal to the low pressure of the interstellar medium at the boundary of the solar system.

The magneto-hydro dynamics (MHD) tells us that the solar magnetic field is "frozen" in the coronal plasma because it has not only the high thermal but also the high electrical conductivities. Therefore, Parker (1958a) suggested that the solar wind brought the coronal magnetic field into the interplanetary space, and the field line was taken an Archimedean spiral configuration by the solar rotation because an end of that was fixed on the solar surface.

1.1.3 Confirmation of the Solar Wind

The Parker's solar wind theory was strongly supported by observations of the cometary ion-tail and direct plasma measurements. Lüst (1961; 1963) verified from observations of cometary tails that the particle stream was emitted continuously from the Sun with

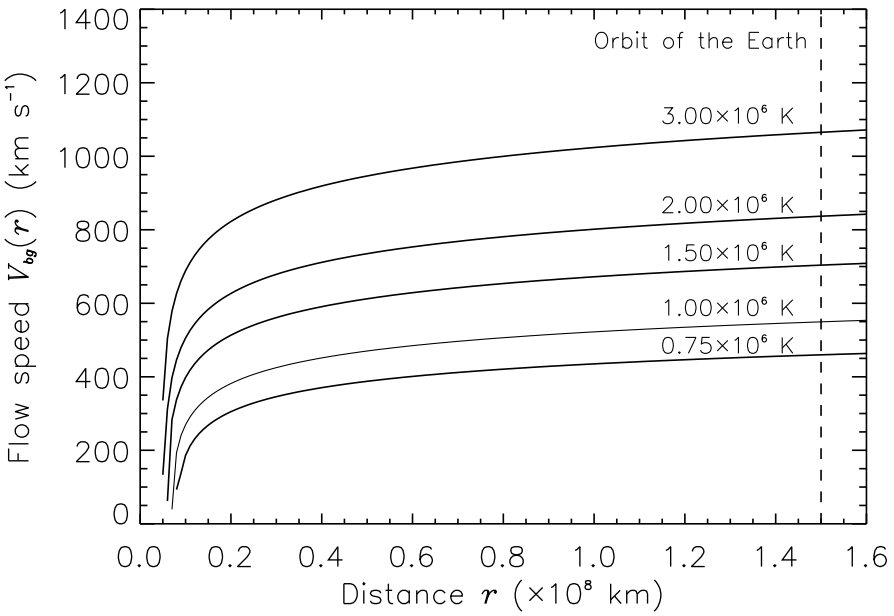

FIGURE 1.2: Radial speed evolution of the solar wind derived from an isothermal corona model with coronal temperatures of 0.75, 1.00, 1.50, 2.00 and 3.00×10^6 K. The vertical broken line indicates the Earth's heliocentric distance (after Parker, 1958a).

a speed of 300 – 400 km s^{-1} even in time for low solar activity. In 1957, the space age was begun by the launch of the first satellite *Sputnik-1*. The satellite technology enabled us to probe the interplanetary space. The moon probe *Luna-2* detected a proton flux with an energy of > 25 eV outside of the Earth's magnetosphere in 1959 (Gringauz et al., 1960). Although the direction of the particle flux could not be confirmed, this was the first detection of the solar wind by a spacecraft. The first clear measurement was given in 1962 by the Venus probe *Mariner-2* (Neugebauer and Snyder, 1962). The *Mariner-2* carried the charged-particle spectrometer which always pointed to the Sun, and made plasma measurements in the interplanetary space using that during August 29 – October 31, 1962. The *Mariner-2* data of ion spectra showed that most of the plasma flux had the velocity of 464 – 563 km s^{-1} (Neugebauer and Snyder, 1962). Such solar particle streams were also corroborated by observations using another satellite. The *Interplanetary Monitoring Platform 1* (IMP-1) was launched in 1963 and observed the Earth's magnetosphere and interplanetary medium with a plasma detector. From analyzing plasma data obtained by IMP-1, Wolfe et al. (1966) found that the average velocity of the solar wind was 378 km s^{-1}, and its significant flux was observed inside an azimuthal sector including the solar direction. The spiral configuration of the interplanetary magnetic field was also confirmed by spacecraft observations (e.g. Wilcox, 1968; Thomas and Smith, 1981).

Careful analysis for *Mariner-2* observations revealed that the actual solar wind was more complex than the Parker's ideal one. Neugebauer and Snyder (1966) reported that

the solar wind comprised its low ($\approx$ 400 km s^{-1}) and high ($\approx$ 700 km s^{-1}) speed streams, which made the 27-days recurrence pattern. They also found that the number density of the solar wind generally reached a maximum on the leading edge of a fast stream. This feature related to the co-rotating interaction region, which will be explained briefly in Section 1.2. The slow and fast streams of the solar wind were examined in detail in later years. The solar source of the fast wind remained a mystery for a while. A detection of the fast wind often related to the absence of sunspots in the vicinity of the solar disk center. Before discovering the solar wind, it was already known that the recurrence of geomagnetic storms could not relate to any visible features on the Sun including sunspots. The geomagnetic storm is an extraordinary fluctuation of the Earth's magnetic field, which was discovered in the mid-18th century (Gonzalez et al., 1994). Bartels (1932) assumed special areas, which were responsible for recurrent geomagnetic disturbances, and called this areas "M-regions". Neugebauer and Snyder (1966) also pointed out that the 27-days recurrence of the fast solar wind may be associated with the M-regions. Unmasking the M-regions required observations of high-energy electromagnetic waves in space. Munro and Withbroe (1972) discovered the "coronal hole" as the low emissive area of the coronal extreme-ultraviolet (EUV) from an satellite experiment. The relationship between the coronal holes and fast-wind stream was identified by Krieger et al. (1973). Sheeley et al. (1976) proved clearly from comparison between the coronal hole, solar wind speed, and geomagnetic index that coronal holes were responsible for recurrent magnetic storms. From these findings, it was established that the large coronal hole was the solar source of the fast wind. Some investigators reported that the slow solar wind was emitted from the vicinity of the coronal hole boundary or the edge of the active region (e.g. Kojima et al., 1999; Sakao et al., 2007).

1.1.4 Properties of the Solar Wind

Properties of the slow and fast solar wind have been investigated using in situ measurements. A series of IMP spacecraft have made observations of the interplanetary plasma in the vicinity of the Earth since 1963. Bame et al. (1977) analyzed plasma data from IMP-6, IMP-7, and IMP-8. They examined the variability of the solar wind characteristics and then found that parameters of the fast wind such as the density and temperature were less variable than the slow wind. Table 1.1 summarizes the physical properties of the solar wind near the Earth's orbit. The solar wind contains not only ionized hydrogens but also other heavy ions such as helium, oxygen, and iron ions. It is known that the abundance of these ions depends on the speed of the solar wind. Richardson and Cane (2004) studied the relationship between the ratio of heavy ions and wind speed. Table 1.2 gives velocity dependences of the mean Fe charge $\langle Q_{Fe} \rangle$ and

TABLE 1.1: Average physical properties of the slow and fast solar wind near 1 AU (adopted from Bame et al., 1977).

	Average with standard deviation	
Property	Slow wind	Fast wind
Flow speed $V_{\rm bg}$ (km s^{-1})	327 ± 15	702 ± 32
Density N (cm^{-3})	11.9 ± 4.5	3.9 ± 0.6
Proton temperature T (K)	$3.4(\pm 1.5) \times 10^4$	$2.3(\pm 0.3) \times 10^5$

TABLE 1.2: Velocity dependences of the mean Fe charge $\langle {\rm Q_{Fe}} \rangle$ and the O VIII / O VII ratio in the solar wind without disturbances (adopted from Richardson and Cane, 2004).

Ratios	Relationship with $V_{\rm bg}$
$\langle {\rm Q_{Fe}} \rangle$	$11.2 - 0.000857 V_{\rm bg}$
O VIII / O VII	$3.004 \exp(-0.00578 V_{\rm bg})$

the O VIII / O VII ratio found by them. Here, the O VIII and O VII represent the seventh and sixth-order charged ions of oxygen, respectively.

The time evolution of the solar wind velocity was studied by combining satellite observations of plasma streams during a part of a solar cycle. Gosling et al. (1971) examined the solar wind data from eight satellites during 1962 – 1970 and found that the frequency distribution of the wind velocity varied with a phase of the solar cycle. Bame et al. (1976) showed an anti-correlation between the average maximum speed of the solar wind and the relative sunspot number during 1962 – 1974. These examinations suggested that the velocity structure of the solar wind was not stable but variable with the solar activity.

As shown in Figure 1.2, the Parker's solar wind theory suggested that the coronal plasma stream accelerated rapidly in the near-Sun region and subsequently propagated with its final speed in the interplanetary space. The propagation of the solar wind in the interplanetary space was investigated using a pair of the *Helios* solar probes. *Helios* were a unique set of spacecraft which approached ≈ 0.3 AU to study the solar wind in the near-Sun region. Using their plasma data, Schwenn et al. (1981) examined radial variations of plasma parameters for the fast and slow wind. Figure 1.3 shows radial evolutions of the wind speed and proton temperature observed by *Helios* between 0.3 and 1 AU. They found that the average speed of the solar wind gradually increased up to 51 ± 11 km s^{-1} in 0.3 – 1 AU for the slow wind, while remained nearly constant in the interplanetary space for the fast solar wind; these were consistent with the Parker's theory. Proton temperatures of the fast and slow wind decreased as $r^{-0.69 \pm 0.08}$ and $r^{-1.21 \pm 0.1}$, respectively. Sheeley et al. (1997) studied the velocity profile of the slow solar wind around the solar equator from tracking plasma blobs using a coronagraph.

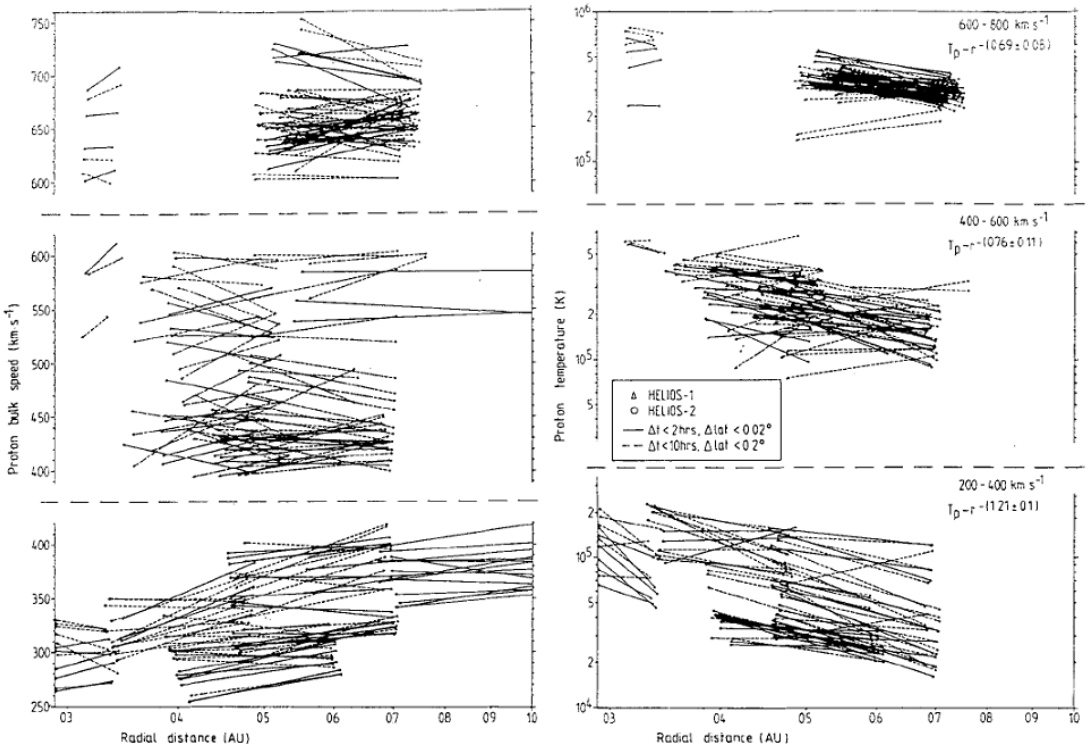

FIGURE 1.3: Radial evolutions of the flow speed (left) and proton temperature (right) observed by the *Helios* solar probes between 0.3 and 1 AU for each velocity range of the solar wind. Top, middle, and bottom rows correspond to the fast (600 – 800 km s^{-1}), moderate (400 – 600 km s^{-1}), and slow (200 – 400 km s^{-1}) solar wind, respectively (adopted from Schwenn et al., 1981).

From this investigation, they found that the slow wind approached its final speed ($\approx$ 300 km s^{-1}) within a distance of 1.74×10^7 km (0.12 AU).

1.2 Co-rotating Interaction Regions

Co-rotating interaction regions (CIRs) are an interface between the fast and slow solar wind, where the plasma density is enhanced. An idea of CIRs originated with an attempt to explain the cause of geomagnetic storms. In 1929, an investigation of the weak and medium magnetic storms revealed the 27-days periodicity of the geomagnetic activity; the weak and medium magnetic storms generated $\Delta H < 180$ nT, where ΔH was a variation in the horizontal magnetic intensity (Greaves and Newton, 1929). Because the Sun had the relative rotational period of $\approx$ 27 days for the Earth, it seemed that the sunspot activity was responsible for the recurrence of geomagnetic storm. However, most of geomagnetic storms excluding intense events were associated with no sunspots. Chapman and Ferraro (1931a; 1931b) presented their theory in which a slab-shaped stream of ionized gas caused the geomagnetic storm by an interaction with the Earth's

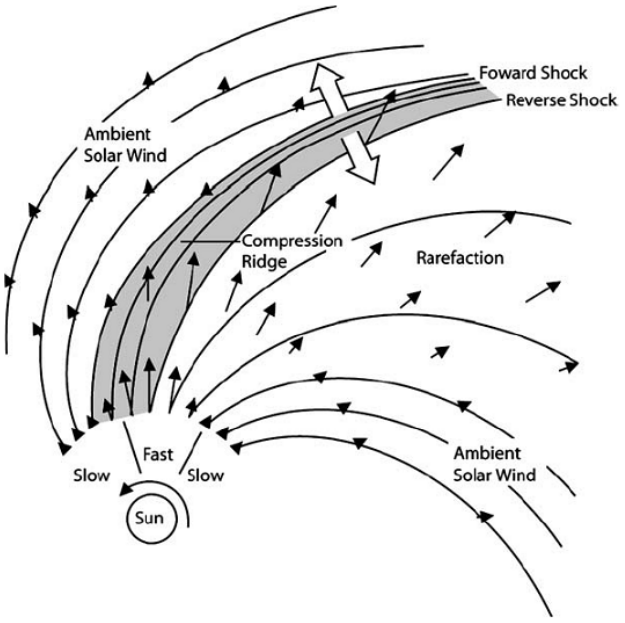

FIGURE 1.4: Two-dimensional drawing of the co-rotating interaction region on the solar equatorial plane. A posterior fast wind overtakes a prior slow wind, and therefore the plasma is compressed at an interface between them to form shocks (adopted from Jian et al., 2006a; the original is in Pizzo, 1978).

magnetosphere. It was assumed that this stream was emitted from a certain area on the solar surface. CIRs were discovered from in situ observations of the space plasma in the early years of the space age. Neugebauer and Snyder (1966) identified the low and high speed solar wind and that the plasma density generally reached a maximum on the interface between them. They also reported that observed density enhancements had not yet form shocks between 0.7 and 1 AU. Beyond 1 AU, Smith and Wolfe (1976) found from plasma observations of the *Pioneer-10* and *Pioneer-11* spacecraft that "interaction regions" were accompanied by shocks, which were called "co-rotating shocks".

Figure 1.4 shows an interaction between the slow and fast solar wind to form the co-rotating shocks. As illustrated in this figure, the solar rotation and a set of the fast and slow wind are responsible to form a CIR. As the Sun spouts radially the low and high speed wind while rotating, the fast solar wind catches up with the prior slow one, and hence the plasma is compressed to develop shocks at the leading edge of a fast wind stream. CIRs trace out an Archimedean spiral which co-rotate with the Sun (Siscoe, 1972). The Earth often encounters few CIRs during 27 days.

1.3 Solar Flares and Prominence Eruptions

Solar flares are one of the most intense outburst for the Sun, which emit electromagnetic-waves and energetic particles. It occurs in active regions where the strength of the magnetic field is high and then sunspots are generally seen. The British amateur astronomer R. Carrington saw intensely bright patches suddenly appear on a large sunspot on September 1, 1859. This spectacle which faded out within five minutes was sketched by him (Carrington, 1859). This transient event is referred to as the white-light flare at present, which is observed using an optical telescope without any filter. Because the white-light flare was a very rare event to occur, the flare research had not progressed until 1892. The American astronomer G. E. Hale invented the spectroheliograph to enable us to observe solar phenomena by a specific spectral line and taken photographs of a solar flare using that (Hale, 1892). The systematic flare observation had been made using the spectroheliograph and spectrohelioscope which could take movies of the solar flare and prominence since the 1930s (Švestka and Cliver, 1992). This ground-based flare patrol had observed visible spectral emissions such as the hydrogen-Hα (656.3 nm) and calcium-K (393.4 nm) lines. In the 1960s, the X-ray emission of solar flares was confirmed by the balloon (e.g. Anderson and Winckler, 1962) and satellite (e.g. Hudson et al., 1969) experiments. At present, solar flares have been monitored using the X-ray sensor onboard the *Geostationary Operational Environmental Satellite* (GOES), and their energy is estimated from the X-ray flux. Solar flares are classified as B ($10^{-6}-10^{-7}$ W m^{-2}), C ($10^{-5}-10^{-6}$ W m^{-2}), M ($10^{-4}-10^{-5}$ W m^{-2}), and X ($10^{-3}-10^{-4}$ W m^{-2}) according to the peak X-ray flux. Intense solar flares have a peak flux between 10^{-5} and 10^{-3} W m^{-2}, which correspond to the M and X classes. Since 1957, the largest flare occurred on November 4, 2003, which emitted the energy flux of $\approx 2.8 \times 10^{-3}$ W m^{-2} classified as X28 (Cliver and Svalgaard, 2004). Many investigators have considered that the flare energy is supplied from the coronal magnetic field via the magnetic reconnection (see, e.g. Sweet, 1969).

Solar flares sometimes accompany by prominence eruptions. Solar prominences are a dense cloud of the cooler plasma (number density $\approx 10^{11}$ cm^{-3}, temperature $\approx 10^4$ K) than the corona, which are maintained in the solar corona by the magnetic field (Hirayama, 1985). Solar prominences are classified into two types, namely the quiescent and eruptive prominences. The former may changes to the latter when a supporting magnetic field becomes unstable by some physical mechanisms which are not yet well understood (van Ballegooijen and Martens, 1989). Eruptive prominences show their different motion from each other; some ones accelerate rapidly to reach velocities of $300-1000$ km s^{-1} (Tandberg-Hanssen et al., 1980), and others show a little acceleration. Figure 1.5(a) shows a picture of a solar flare with three prominences, which was obtained

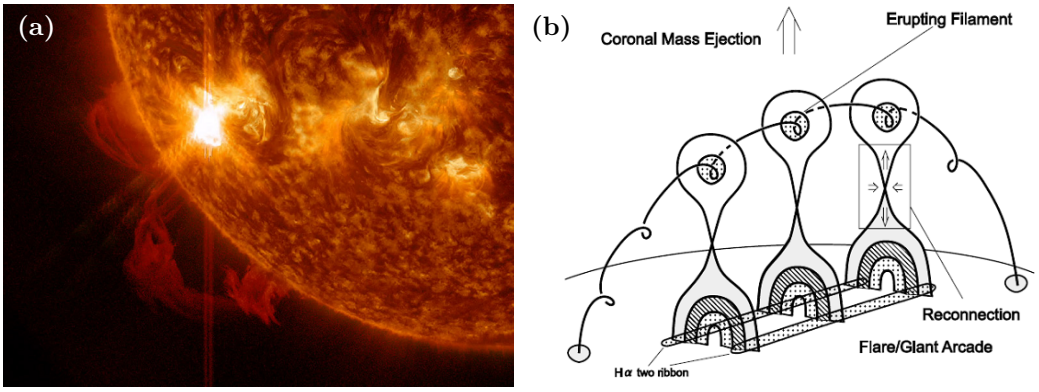

FIGURE 1.5: (a) Solar flare (the brightest region) and prominences (above the solar limb) observed using the *Atmospheric Imaging Assembly* (AIA) onboard the *Solar Dynamics Observatory* (SDO) on July 28, 2012 (Courtesy of NASA/SDO and the AIA science team). (b) Schematic explanation of the CSHKP flare model (adopted from Shiota et al., 2005).

by an EUV imaging from the *Solar Dynamics Observatory* (SDO) on July 28, 2012. In this picture, a solar flare emits a strong light, and one of the prominences exhibits its arch-shaped structure. The relationship between solar flares and prominence eruptions is often explained by the Carmichael, Sturrock, Hirayama, Kopp and Pneuman (CSHKP) model (Carmichael, 1964; Sturrock, 1966; Hirayama, 1974; Kopp and Pneuman, 1976; see also Shibata and Magara, 2011). Figure 1.5(b) explains schematically CSHKP model in which an ascending prominence (filament) stretches magnetic loops to lead to the reconnection at field crossing points. Shiota et al. (2005) proposed a self-consistent HMD model, which explained the formation of a cusp-shaped arcade with a prominence eruption. These phenomena lead to coronal mass ejections which are explained in the next section.

1.4 Coronal Mass Ejections

1.4.1 Brief History of Coronal Mass Ejections

Coronal mass ejections (CMEs) are a transient phenomenon in which a large lump of magnetized coronal plasma erupts from the Sun into the interplanetary space. Hence, CMEs are different from the solar wind as a continuous flow of plasma, and sometimes accompany with solar flares. The presence of such events had been predicted from the relationship between solar flares and geomagnetic storms. A solar flare and a subsequent magnetic storm are firstly referred by Carrington (1859). Maunder (1904a; 1904b) pointed out that the occurrence rate of "great" magnetic storms which generated $\Delta H > 300$ nT was correlated with the variation of the sunspot number. These

findings suggested the solar origin of intense geomagnetic storms. In the first half of the twentieth century, it had generally been known that magnetic storms on the Earth followed solar flares with a time lag between < 1 and 3 days (e.g. Hale, 1931; Newton, 1943). This fact implied that something which caused magnetic storms was not an enhanced radiation traveling at the speed of light but a sporadic emission of charged particles from the Sun (Chapman, 1950). Gold (1959) discussed a material eruption with magnetic fields resulting from a solar outburst. His description of eruption, i.e. magnetic arches expanding with the velocity of 1000 km s^{-1}, was close to the present picture of CMEs. Parker (1961) elucidated from solving the hydrodynamic equations that the coronal plasma heated by a large flare could generate a blast wave, which moved out through the interplanetary space with a speed of 1500 km s^{-1}. The observational confirmation of such eruptions required to develop a solar observing instrument.

The coronagraph was invented by the French astronomer B. Lyot, and the first monochromatic photo of corona was obtained using this telescope in 1939 (Lyot, 1945). In the coronagraph field-of-view (FOV), the bright solar surface was hidden by a circular disk to see the faint corona. This instrument allowed us to monitor the solar corona without waiting for a total solar eclipse. Sporadic ejections of the solar material suggested from theoretical studies were discovered by space-borne coronagraph observations in 1971 (Tousey, 1973). Tousey et al. (1974) observed 19 outward-moving clouds in the corona using the white-light coronagraph (Koomen et al., 1975) onboard the *Orbiting Solar Observatory 7* (OSO-7) between October 1971 and May 1973. Similar phenomena were also monitored using a ground-based coronagraph and radio observations. DeMastus et al. (1973) investigated data of the coronal Fe XIV emission obtained using the Sacramento Peak Observatory six-inch filter coronagraph during 1956 – 1972 and identified 30 "rapid green-line events" such as oscillations and disruptions. They found that 18 of them showed a material ejection. Smerd and Dulk (1971) examined the characteristics of 12 moving type-IV radio bursts detected by the 80 MHz radioheliograph at the Culgoora Observatory between February 1968 and April 1970 and found that some of them were associated with prominence eruptions. At that time, the above events in the solar corona were called "coronal transients" (Tousey et al., 1974) or "coronal disturbances" (DeMastus et al., 1973). According to Howard (2011), a famous term of "coronal mass ejection" appeared for the first time in Gosling et al. (1976).

Since 1971, CMEs have been observed mainly using space-borne coronagraphs. OSO-7 operated for CME observations before its re-entry in 1974 (Howard, 2011). The United States space station *Skylab* was launched in 1973. The *Skylab* carried a white light coronagraph as one of six experiments on the *Apollo Telescope Mount* (ATM) instrument package (MacQueen et al., 1974). During 227 days of *Skylab* mission, 77 CMEs were identified using this coronagraph (Munro et al., 1979). In the 1980s, CME observations

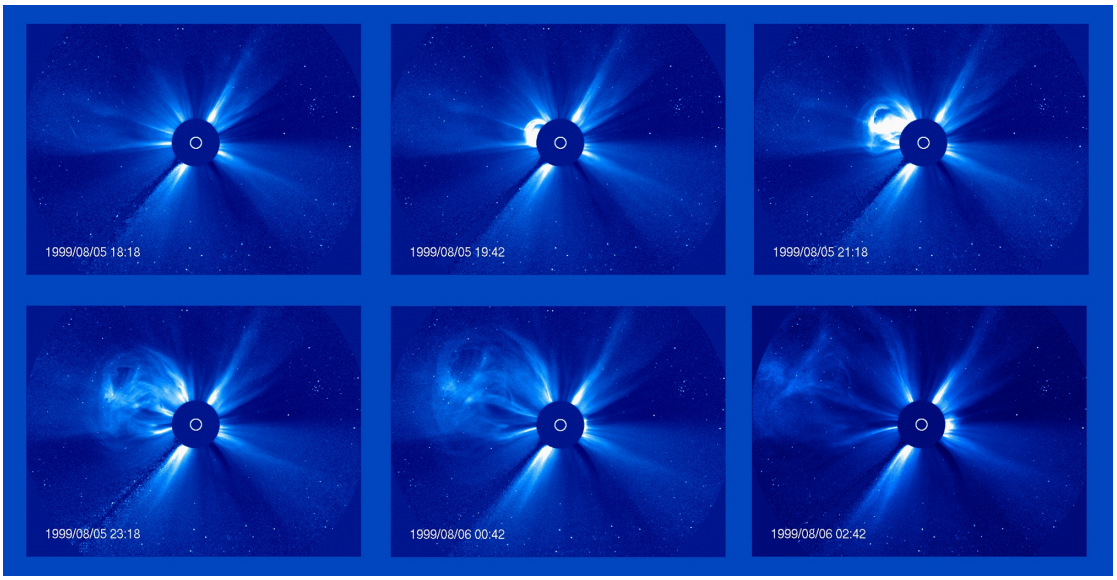

FIGURE 1.6: Successive pictures of a coronal mass ejection observed by the *Large Angle and Spectrometric Coronagraph* (LASCO) onboard the *Solar and Heliospheric Observatory* (SOHO) between August 5 at 18:18 and 6 at 02:42, 1999. In each panel, the Sun is hidden by a circular disk and its position is indicated by the white circle. (Courtesy of SOHO/LASCO consortium of ESA and NASA).

were continued using two satellites. The US Air Force's *P78-1* satellite with the *Solwind* coronagraph was launched in 1979 and operated until 1985 (Howard, 2011). The *Solar Maximum Mission* (SMM: Bohlin et al., 1980) carried the *Coronagraph/Polarimeter* (C/P: MacQueen et al., 1980) and observed many CMEs during 1980 – 1989 without a data gap from 1981 to 1983. After seven years for the absence of CME observations, the *Solar and Heliospheric Observatory* (SOHO) spacecraft began to operate in 1996. SOHO carried the *Large Angle and Spectrometric Coronagraph* (LASCO: Brueckner et al., 1995) instrument for CME observations. Since then, SOHO has identified more than 8000 CMEs (Gopalswamy, 2004) to enable us to make an exhaustive study of them. Figure 1.6 shows successive pictures of a CME taken by SOHO/LASCO in August 1999. It is seen that a balloon-shaped structure as a CME expands in the north-east direction of the Sun.

1.4.2 Solar Source and Morphology of CMEs

In the late 1970s, it was already known from CME observations using space-borne coronagraphs that CMEs were associated with solar flares and prominence eruptions. Munro et al. (1979) examined the relationship between 77 CMEs which observed by the white-light coronagraph on *Skylab*/ATM and other solar activities. From this examination, they found that 34 CMEs were accompanied by Hα phenomena on the solar surface, and

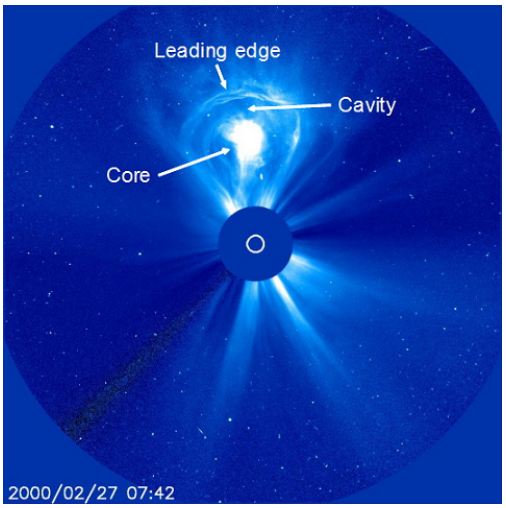

FIGURE 1.7: Three part structure of a representative CME observed on February 27, 2000 (Courtesy of SOHO/LASCO consortium of ESA and NASA).

40% of them were associated with solar flares while 50% were associated with prominence eruptions without flares. Webb and Hundhausen (1987) studied the relationship between CMEs and other solar phenomena using SMM observations and confirmed results presented by Munro et al. (1979). Gopalswamy et al. (2003) found that out of 186 prominence eruptions observed by the Nobeyama Radioheliograph during 1996 – 2001, 134 (72%) events were associated with CMEs. On the other hand, Kahler (1977) investigated the relationship between X-ray flares and coronal transients and found that long-duration X-ray events (LDEs) correlated with CMEs. Sheeley et al. (1983) pointed out that the probability of CME occurrence monotonically increased with the X-ray duration, and all solar flares with durations more than six hours had CMEs.

A mass of chromospheric and coronal materials expelled by a solar flare or prominence eruption is observed as a CME when it comes into the coronagraph FOV. Some CMEs have the three-part structure, namely the leading edge, cavity, and core, as shown in Figure 1.7. Hundhausen (1987) pointed out that prominence-associated CMEs had this structure. They also suggested from a comparison between SMM C/P and the Mauna Loa prominence monitor observations that the core corresponded to a prominence, and the leading edge was a compressed coronal plasma by an expansion of the cavity. The cavity has been thought to be the magnetic flux rope of which its both ends anchored on the solar surface (Gopalswamy, 2004). Indeed, the three-part structure is often observed in CMEs associated with prominence eruptions from quiet regions (Gopalswamy, 2004), and considered to be the standard configuration of CMEs. However, it is indicated from observations that only $\approx$ 30 % of CMEs have the complete three-part structure (Chen, 2011). Most of CMEs are consist of the leading edge and cavity without the core (Low, 2001).

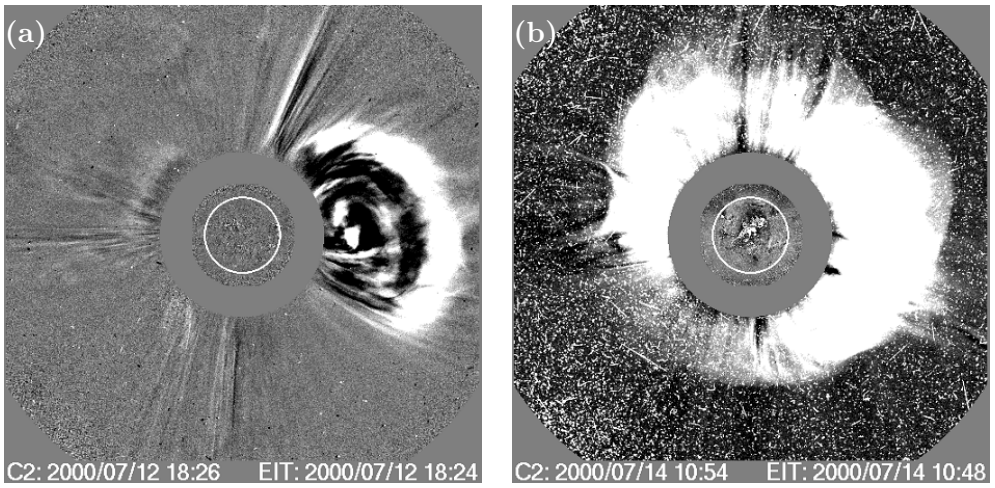

FIGURE 1.8: (a) Normal and (b) full-halo CMEs observed by SOHO/LASCO. (a) and (b) were observed on July 12 and 14, 2000, respectively. In each panel, the white circle represents the Sun. The normal CME has a width of $\leq 120°$, which erupts in the west direction of the Sun. The full-halo CME is expelled toward the Earth, and then the Sun is seen to surround itself with the CME material in the sky plane. (adopted from the web page of the SOHO/LASCO CME catalog).

An aspect of CMEs is changed due to not only the relationship with solar phenomena but also their source position. If a solar flare or prominence eruption occurs when its source is around the center of the solar disk, an associated CME would be expelled toward the Earth. Earth directed and anti-Earth directed CMEs are called "halo" CMEs because they appear to an observer on the Earth as if the CME material would surround the Sun. Full-halo CMEs have an apparent width of 360°. On the other hand, CMEs show their balloon-shaped structure when their source region is near the solar limb. Figure 1.8 shows a normal and full-halo CMEs observed in July 2000. Here, "normal" means that the appearance of CMEs is neither a halo nor a "partial halo". Partial-halo CMEs are defined as CMEs with a width of $> 120°$, but they never completely surround the Sun in the coronagraph FOV (Yashiro et al., 2004). Almost all of CMEs which reached the Earth are observed either as halo or partial-halo CMEs.

1.4.3 General Properties of CMEs

Basic characteristics of CMEs are the apparent speed ($V_{\rm SOHO}$), apparent width (ψ), mass (m), and kinetic energy ($E_{\rm k}$). The apparent speed of CMEs is measured by tracking the leading edge for CMEs in the coronagraph FOV (Yashiro et al., 2004). The mass of CMEs is estimated from the ratio of the observed excess brightness over the brightness of a single electron deduced from the Thomson scattering function with the assumption of the plasma abundance, and the kinetic energy of CMEs is the mass times squares of the center-of-mass velocity (Vourlidas et al., 2000). It is noted that the center-of-mass

TABLE 1.3: Average, minimum, and maximum values for physical properties of CMEs identified using SOHO/LASCO during 1996 – 2006. The averages of mass and width are calculated from data of normal CMEs with width of $< 120°$ (adopted from Gopalswamy et al., 2009 and the web page of the SOHO/LASCO CME catalog).

Property	Average	Minimum	Maximum
Apparent speed $V_{\rm SOHO}$ (km s^{-1})	475	21	3387
Width ψ (deg)	44	1	360
Mass m (kg)	3.5×10^{11}	5.5×10^{7}	2.0×10^{14}
Kinetic energy $E_{\rm k}$ (J)	2.9×10^{22}	6.6×10^{17}	6.9×10^{25}

velocity is not equivalent to the apparent speed because of the CME expansion. These properties were already estimated in the early phase of the CME study with space-borne coronagraphs. Gosling et al. (1974) found 4×10^{12} kg for the mass and estimated 3.2×10^{23} J as the kinetic energy from *Skylab*/ATM observations of the 10 August 1973 CME. Gosling et al. (1976) made a systematic study of ejection speeds and revealed that the speed of CMEs ranged between < 100 km s^{-1} and ≈ 1200 km s^{-1} with the average value of 470 ± 50 km s^{-1}. Poland et al. (1981) analyzed *P78-1*/*Solwind* observations of six CMEs near the peak of a solar cycle and found that CMEs had masses of 7×10^{11} – 2×10^{13} kg and outward speeds of 150 – 900 km s^{-1}. They also found from comparison with earlier studies that the occurrence rate of CMEs near solar maximum tended to be higher than the rate during the declining phase of the solar cycle. The solar activity dependences of the CME occurrence rate and the average CME speed were confirmed by SOHO/LASCO observations in later years (Gopalswamy, 2004).

The estimation of CME properties depends on the sensitivity of instruments (Gopalswamy, 2004). Here, properties of CMEs derived from SOHO/LASCO observations are presented because SOHO/LASCO is the most sensitive instrument in space-borne coronagraphs had ever been used. Table 1.3 gives an average, minimum, and maximum values for the apparent speed, width, mass, and kinetic energy of CMEs, which estimated from SOHO/LASCO observations during 1996 – 2006. There were 37 CMEs with speeds exceeding 2000 km s^{-1} in the period of 1996 – 2006, and 23 of them were observed at and near the solar maximum (2000 – 2003). Properties of each CME are presented in the SOHO/LASCO CME catalog (Yashiro et al., 2004; Gopalswamy et al., 2009; available at `cdaw.gsfc.nasa.gov/CME_list/`). The largest speed ($V_{\rm SOHO} = 3387$ km s^{-1}) was observed for the 10 November 2004 halo CME with a large (X2.5 in classification) solar flare, while the smallest one ($V_{\rm SOHO} = 21$ km s^{-1}) was for a normal CME with no obvious flare on May 5, 2005.

As mentioned in Subsection 1.4.2, there are two types of CMEs, namely the flare-associated and prominence-associated CMEs. Further studies revealed that CMEs with flares had different properties from ones associated with prominence eruptions. Gosling

et al. (1976) pointed out that flare-associated CMEs had the average speed of 775 ± 110 km s^{-1}, while CMEs associated with eruptive prominences had the average speed of 330 ± 40 km s^{-1}. MacQueen and Fisher (1983) examined 12 CMEs using the Mauna Loa K-coronameter and found that flare-associated CMEs had high velocities with little accelerations, while prominence-associated CMEs exhibited large accelerations. From these results, they suggested that the acceleration mechanism acting on CMEs was different between flare-associated and prominence-associated CMEs. Moon et al. (2002) made a statistical study of the CME kinematics in the coronagraph FOV with huge sample of SOHO/LASCO CMEs and found that a median speed of CMEs with large flares was higher than that of CMEs with weak flares. They also pointed out that flare-associated CMEs tended to be more decelerated than CMEs associated with prominence eruptions.

Theoretical studies of the CME kinematics have appeared since the late 1970s. Mouschovias and Poland (1978) and Anzer (1978) proposed a model in which a loop containing the electric current or magnetic field expanded outward in the ambient plasma to explain the behavior of CMEs in the solar corona. From an examination of the model, Anzer (1978) concluded that CMEs might obtain their final velocity ranging between 100 and 600 km s^{-1} in a distance of 2.5 solar radii (1.74×10^6 km or 0.012 AU) from the solar center by the electromagnetic force. Adopting their ideas, Chen (1989) studied the motion of a toroidal current loop with the Lorentz force and showed as an example that a loop might expand at ≈ 1200 km s^{-1} by the magnetic energy dissipation of 6×10^{24} J in 30 minutes.

1.4.4 Interplanetary CMEs

CMEs propagate outward from the Sun to enter the interplanetary space. When they are at larger distances from the Sun, generally much larger distances than the coronagraph FOV, they are referred to as interplanetary CMEs (ICMEs: Howard, 2011). Some of them reach the Earth and often drive geomagnetic storms (e.g. Tsurutani et al., 1988; Gosling et al., 1990; Brueckner et al., 1998). Historically, therefore, ICMEs have been detected at the Earth by magnetic storms followed by solar flares since 1859. In the space age, ICMEs and their associated shocks have been observed directly by spacecraft around the Earth. Gosling et al. (1968) reported observations of two interplanetary shocks by the twin *Vela-3* satellites. These interplanetary shocks were detected as a sudden change of the plasma velocity and density on October 5, 1965, and January 20, 1966, respectively, which were associated with solar flares. Hundhausen et al. (1970) examined 19 flare-associated disturbances which were identified by the *Vela-3* and *Vela-4* satellites and found that the average values of their mass and kinetic energy were

TABLE 1.4: Average physical properties of near-Earth ICMEs deduced from in situ measurements during 1996 – 2009 (adopted from Richardson and Cane, 2010).

Property	Average with standard deviation
Speed (km s^{-1})	476 ± 6
Density (cm^{-3})	6.9 ± 0.2
Radial size (AU)	0.33 ± 0.01
Proton temperature ($\times 10^4$ K)	4.87 ± 0.29
Magnetic field strength (nT)	10.1 ± 0.3

3×10^{13} kg and 5×10^{24} J, respectively, at 1 AU. This result suggested that these near-Earth disturbances derived from coronal and chromospheric material expelled from the Sun by flares. A comparison between a near-Sun CME observed by *Skylab*/ATM and its related interplanetary disturbance detected by the *Pioneer-9* spacecraft was made by Gosling et al. (1975). They concluded from the comparison that estimated properties of the interplanetary disturbance ($m = 4.2 \times 10^{13}$ kg, $E_k = 1.2 \times 10^{25}$ J) at 1 AU agreed reasonably with those of the near-Sun CME ($m = 2.4 \times 10^{13}$ kg, $E_k = 1.1 \times 10^{25}$ J). This was the first confirmation of the connection between CMEs and near-Earth ICMEs. After that, similar studies had been made by many investigators (e.g. Schwenn, 1983; Lindsay et al., 1999).

At present, solar wind monitoring satellites such as IMP-8 (Paularena and King, 1999), the *Wind* (Acuña et al., 1995), and the *Advanced Composition Explorer* (ACE: Stone et al., 1998) have been used for in situ measurements of ICMEs near 1 AU (e.g. Cane and Richardson, 2003; Jian et al., 2006b). Because ICMEs have different plasma properties from the solar wind, they may be distinguished from the ambient medium by in situ measurements. ICMEs are characterized by higher charge-states of heavy ions (Bame et al., 1979), large enhancements in helium abundance (Borrini et al., 1982), magnetic flux ropes or magnetic clouds (Gosling, 1990; Burlaga et al., 1990), bidirectional electrons (Gosling et al., 1987) and others (see also Wimmer-Schweingruber et al., 2006). Richardson and Cane (2010) identified 322 ICMEs from in situ data with their characteristics during 1996 – 2009. Table 1.4 gives average properties of ICMEs at 1 AU determined by them.

The detection of ICMEs between the Sun and the Earth required the interplanetary probe and remote-sensing techniques. The *Mariner-2* spacecraft observed an abrupt increase of the plasma speed and magnetic field on October 7, 1962 when it was at 0.07 AU from the Earth (Sonett et al., 1964; Schubert and Cummings, 1967). This was the first detection of an interplanetary shock between the Sun and the Earth by the space probe. Lazarus et al. (1970) studied two interplanetary shocks using the *Mariner-5* space probe and the *Explorer-34* satellite which were at most 0.1 AU distant each

other along the Sun-Earth line and found that plasma parameters by the *Explorer-34* showed a good correlation with those by the *Mariner-5*. This result implied that the interplanetary shock retained its properties over radial distances of 0.1 AU. Twin *Helios* spacecraft, which approached ≈ 0.3 AU from the Sun, observed not only the solar wind but also an ICME. Dryer et al. (1982) reported the tracking of a CME/ICME from the solar surface to ≈ 0.7 AU by combining the ground-based Hα telescope, *P78-1*/*Solwind*, *Helios-2*, and the *Pioneer Venus Orbiter* (PVO) observations. Burlaga et al. (1982) examined an interplanetary magnetic cloud using the *Helios-1*, which was at 0.54 AU from the Sun on June 20, 1980, and revealed its physical properties. In these studies, researchers analyzed in situ measurements of ICMEs by the *Helios* solar probes. In contrast to the in situ measurement, remote sensing allows us to obtain a global picture of ICMEs. Jackson and Leinert (1985) and Jackson (1985a; 1985b) reported the remote-sensing of ICMEs using the zodiacal light photometers onboard the *Helios* spacecraft. From this observation, they estimated the mass of an ICME at 2.5×10^{13} kg (Jackson and Leinert, 1985). After their works, the *Solar Mass Ejection Imager* (SMEI: Eyles et al., 2003) onboard the *Coriolis* satellite and the *Heliospheric Imager* (HI: Eyles et al., 2009) onboard the *Solar-Terrestrial Relation Observatory* (STEREO: Kaiser et al., 2008) spacecraft have been used for the optical remote-sensing of ICMEs (e.g. Jackson et al., 2006; Howard and DeForest, 2012). Remote sensing using ground-based radio telescopes is also a useful means for the observation of ICMEs. The interplanetary scintillation (IPS) is a kind of the radio remote-sensing method. Figure 1.9 shows appearances of ICMEs reconstructed for the 20 September 1999 and 14 July 2000 disturbance events using radio remote-sensing by IPS (Tokumaru et al., 2006). The next section describes IPS observations and reviews studies of ICMEs by those briefly.

1.5 The Interplanetary Scintillation

1.5.1 Brief History of the Interplanetary Scintillation

In the Universe, there are various celestial objects such as the fixed star, galaxy, nebula, quasar, and pulser. Some of them emit not only the visible light but also the radio wave. Radio signals emitted from a distant object propagate through the interstellar and interplanetary space, and a small fraction of those reach the Earth. In 1962 and 1963, the British physicist A. Hewish and his colleagues found unusual fluctuations of the signal intensity for radio objects 3C119, 3C138, and 3C147 from 178 MHz observations. It was known that these radio objects had a small angular diameter. They investigated these phenomena, and revealed that radio fluctuations had a time scale of $1-2$ seconds, which could not be caused by ionospheric irregularities. Therefore, they considered

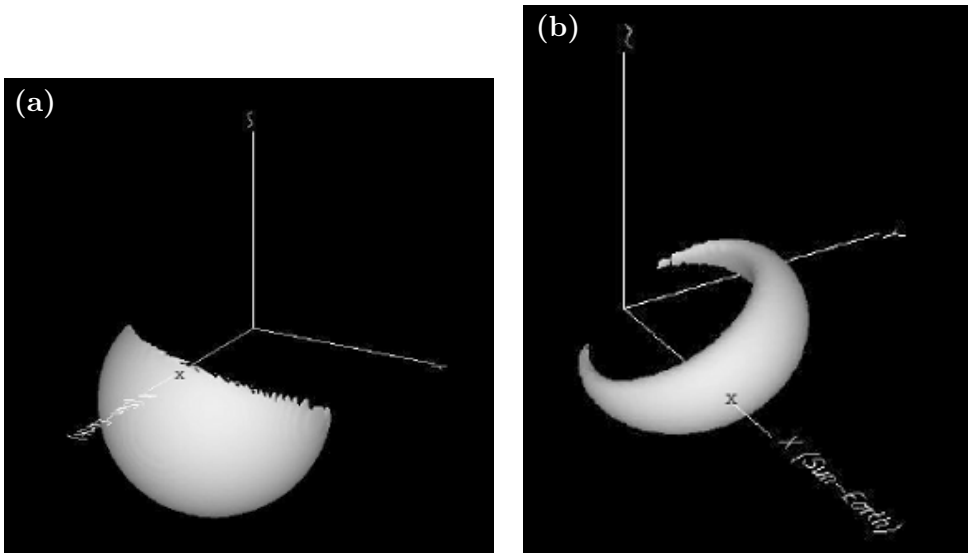

FIGURE 1.9: (a) Shell-shaped and (b) flux-rope structures of ICMEs reconstructed by fitting models to data of interplanetary scintillation observations. (a) and (b) are reconstructions for the 20 September 1999 and 14 July 2000 disturbance events, respectively. In each panel, the origin of coordinate axes is a position of the Sun, and the intersection of the boundary of shell/flux-rope with the x-axis (Sun-Earth line) is marked by a cross (adopted from Tokumaru et al., 2006).

a scintillation arising from irregularities of the interplanetary medium and referred to this phenomenon as the interplanetary scintillation (IPS: Hewish et al., 1964). Hewish et al. (1964) also pointed out that the IPS technique provided a useful means to observe the solar wind over a wider range of latitude, longitude, and distance, while the direct measurement of the solar wind using space probes were confined in the ecliptic plane. After their pioneering work, a large radio telescope, which was a two-dimensional array of the 480 m $\times$ 45 m aperture, was build at the Mullard Radio Astronomical Observatory in United Kingdom in 1967 to study IPS because of faint emissions of radio sources (Hewish et al., 1968). This radio array enabled to measure IPS of about 900 radio sources in each day and monitor then the solar wind and interplanetary disturbances (Duffett-Smith et al., 1980; Gapper et al., 1982). Similar instruments were constructed at the Pushchino Radio Astronomy Observatory in Russia (Vitkevich et al., 1976) and at el Instituto de Geofísica, Universidad Nacional Autónoma de México in Mexico (Mejia-Ambriz et al., 2010). For IPS observations in India, the Ooty Radio Telescope (ORT: Swarup et al., 1971) at the Radio Astronomy Centre had been used since 1986 (e.g. Manoharan and Ananthakrishnan, 1990) and was upgraded during 1991 – 1992 (Manoharan et al., 2000), which was a cylindrical parabolic antenna having the 530 m $\times$ 30 m aperture with the elevation drive system.

The IPS observation with a single radio-telescope is capable of the measurement of electron density irregularities in the interplanetary plasma (Antonova and Vitkevich,

1969). Burnell (1969) found from a northern sky survey of IPS at the Mullard Radio Astronomical Observatory that most of scintillation enhancements tended to recur with a period of 27 days and pointed out the relationship between these enhancements and co-rotating streams. Gapper et al. (1982) made maps of the enhanced scintillation across the sky, which enabled us to visualize ICMEs and CIRs. The multi-station IPS observation was also begun in the late 1960s, which could determine precisely the speed of the solar wind. Because the diffraction pattern of radio scattering is caused by irregularities of the interplanetary plasma and moved with those, one could estimate the speed of the solar wind from the time delay of scintillated signal received at two or more stations which are distant each other. Dennison and Hewish (1967) estimated the speed of the solar wind using IPS data which derived from a triangular arrangement of 81.5 MHz radio telescopes. Solar wind researchers in the University of California, San Diego began the IPS measurement with three stations of 74 MHz array in the 1970s (Armstrong and Coles, 1972; Coles et al., 1978). Vitkevich and Vlasov (1970) made simultaneous observations of the radio scintillation using three antennas in Russia and then determined the velocity and size of plasma irregularities in the interplanetary space.

At present, IPS observations are taking by researcher groups at el Instituto de Geofísica, Universidad Nacional Autónoma de México in Mexico, the P. N. Levedev Physical Institute of the Russian Academy of Science in Russia, the Tata Institute of Fundamental Research in India, the Korean Space Weather Center in Korea, and the Solar-Terrestrial Environment Laboratory (STEL), Nagoya University in Japan. The STEL IPS observation is detailed in the next subsection.

1.5.2 STEL IPS Observation

IPS observations in our country were begun to make at the Research Institute of Atmospherics, which was the predecessor of STEL, Nagoya University in 1969. In this year, the first radio telescope for IPS observation was constructed at the Toyokawa observatory. In 1971, the multi-station IPS observation at three separated observatories (Toyokawa, Fuji, and Sugadaira) was begun to investigate properties of the solar wind and interplanetary disturbances (Kakinuma et al., 1973). This early system comprised three two-dimensional dipole arrays operated at 69 MHz of the very high frequency (VHF), which was suitable to determine the speed and density irregularities of the solar wind between 0.5 and 1.3 AU (Watanabe and Kakinuma, 1984). To investigate the solar wind in the near-Sun region, new radio telescopes operated at 327 MHz of the ultra high frequency (UHF) were begun to construct at the same observatories in 1977 (Kojima et al., 1982) and to make simultaneous observations of radio scintillations in 1982. IPS observations at 327 MHz allowed us to determine the solar wind condition between 0.2

FIGURE 1.10: Locations of the Toyokawa, Fuji, and Kiso observatories and Nagoya city in the central region of Honshū island, Japan.

and 1 AU with a cadence of 24 hours. In 1993, the fourth UHF telescope for IPS observations was built at the Kiso observatory to make more extended observations (Asai et al., 1995).

At present, STEL IPS observations at 327 MHz are performing at the Toyokawa, Fuji, and Kiso observatories. Figure 1.10 shows locations of these observatories. Antenna stations are about 100 km distant from each other to take a cross-correlation analysis of IPS signals to determine the speed of the solar wind. Figures 1.11 and 1.12 exhibit antennas at the Fuji and Kiso observatories, which have a cylindrical parabolic reflector of $\approx$ 2000 m^2 aperture with the elevation drive system. The reflector is made of stainless-steel wires stretched through parabolic frames, and an array of dipoles with pre-amplifiers is equipped near the reflector's focal line. These antennas track radio sources by combining the mechanical rotation of reflector in the North-South direction and the electrical beam shifting with a phased array in the East-West direction. At the Toyokawa observatory, a similar UHF antenna was replaced by the Solar Wind Imaging Facility (SWIFT: Tokumaru et al., 2011) in 2007. Figure 1.13 shows a photo and sketch of SWIFT. This radio telescope has two cylindrical parabolic reflectors and two arrays of dipoles with pre-amplifiers, and can shifts the beam electrically with phased arrays in the North-South direction. Because this antenna is not steerable, SWIFT measures scintillations of radio sources around their local meridian transit.

(a)

(b)

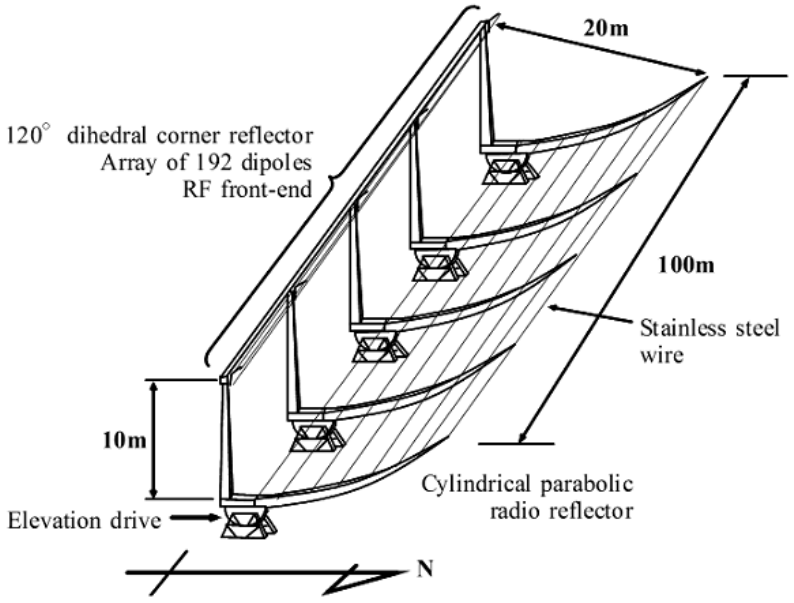

FIGURE 1.11: (a) A picture of the Fuji IPS Telescope (FIT) at the Fuji observatory and (b) a sketch of FIT.

(a)

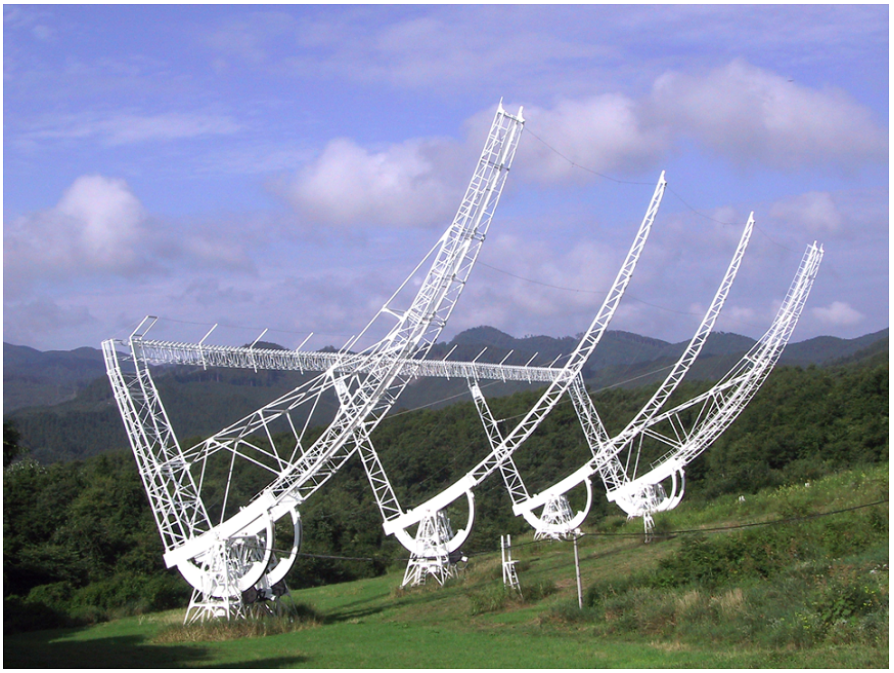

(b)

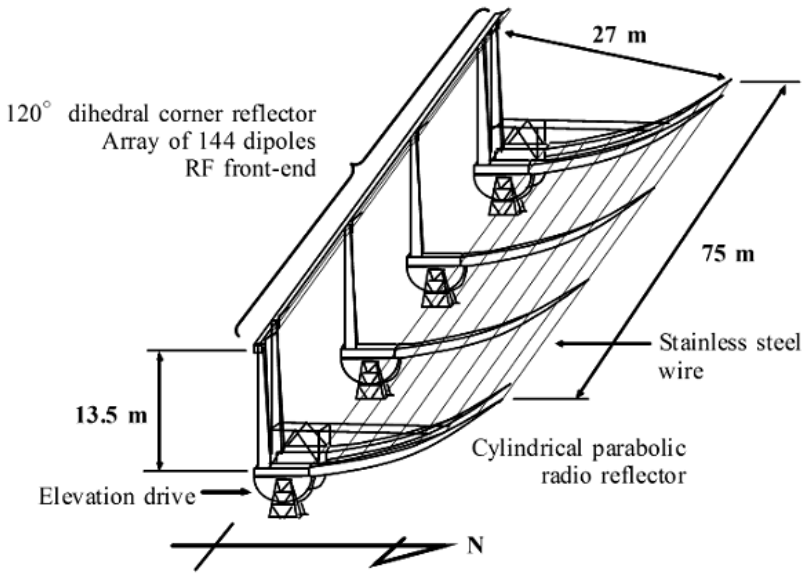

FIGURE 1.12: (a) A picture of the Kiso IPS Telescope (KIT) at the Kiso observatory and (b) a sketch of KIT.

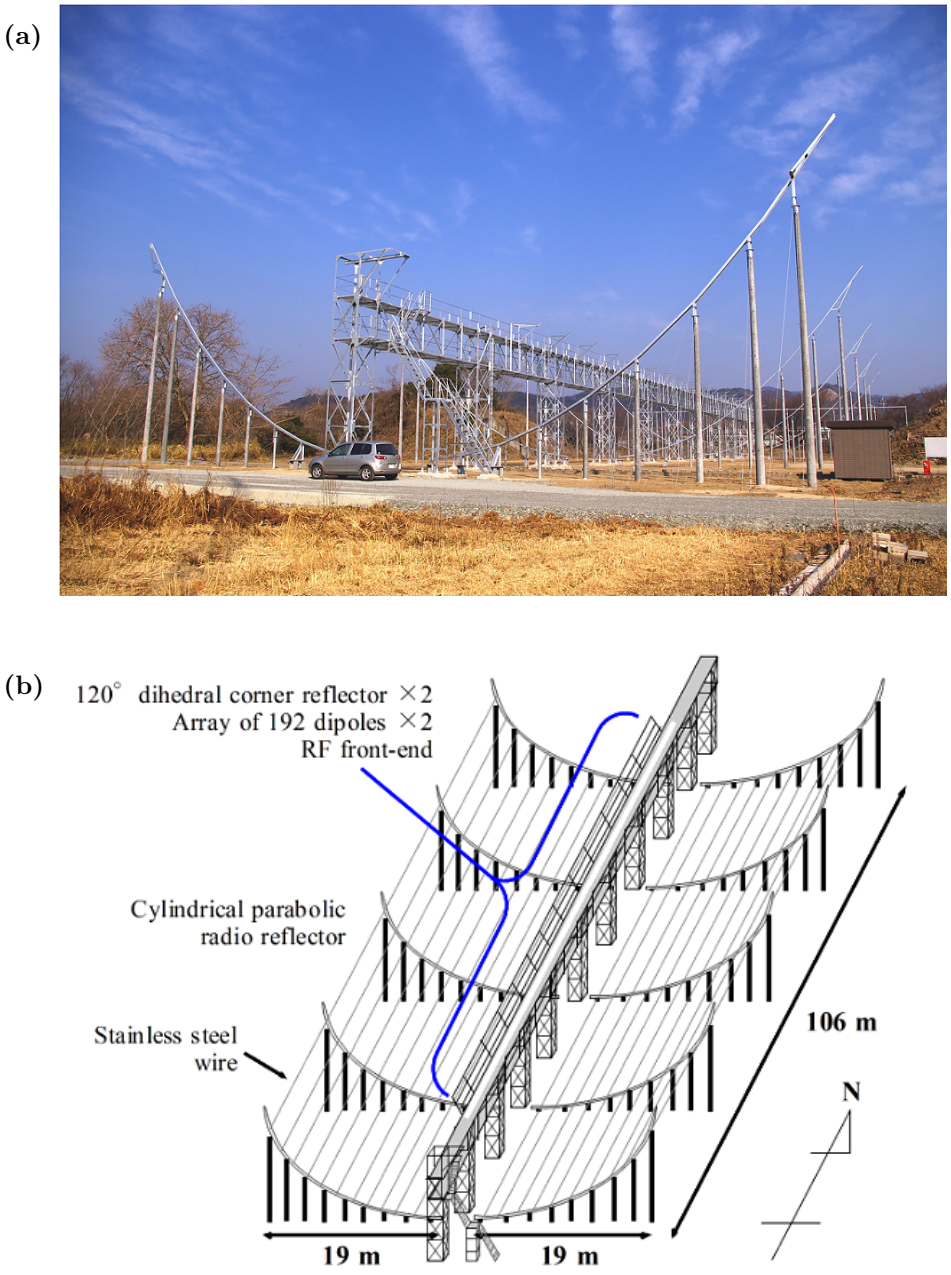

FIGURE 1.13: (a) A picture of the Solar Wind Imaging Facility (SWIFT) at the Toyokawa observatory and (b) a sketch of SWIFT.

1.5.3 ICME Investigations using IPS Observations

In IPS observations, an ICME or interplanetary shock is identified by an abrupt and short-lasted increase of the scintillation index. Sharp and Harris (1967) reported a large enhancement of scintillation associated with a solar flare on the radio source CTA 21. This was the first detection of ICMEs by IPS observations. Since 1970, many researchers made IPS observations of interplanetary shock waves (e.g. Wiseman and Dennison, 1972; Ward, 1975; Houminer, 1976; Pintér, 1982; Watanabe and Kakinuma, 1984). Tappin (1984) and Watanabe et al. (1989) made a connection between near-Sun CMEs and ICMEs from a combination of the coronagraph and IPS observations. For the kinematics of ICMEs, Rickett (1975) observed scintillation enhancements of few radio objects which related to a major solar flare on August 7, 1972 and found that this flare-associated interplanetary disturbance showed a less deceleration. Manoharan et al. (2001) examined an ICME associated with the 14 July 2000 flare event, which was particularly referred as the "Bastille day event", using ORT and other instruments and found its two-step deceleration. Yamashita et al. (2003) studied the interplanetary propagation of the 8 November 1997 and 12 July 2000 CMEs by STEL IPS observations and reported that their velocity evolution may be described by a power-law equation of distance.

1.6 Dissertation Outline

In this thesis, we focus on the propagation of ICMEs from the Sun to the Earth. Because ICMEs are the main driver of intense geomagnetic storms to affect the operation of satellite, radio communication, and power grid, the understanding of their propagation is very important for the space weather forecasting to predict when a geomagnetic disturbance begins. CMEs are initiated by prominence eruptions with or without solar flares and acquire the larger mass and volume than the initial state of eruptions by incorporating the coronal plasma with the prominence material in the solar corona. Subsequently, they enter the interplanetary space and propagate outward through the solar wind. Prominence eruptions and their associated CMEs are tracked by the Hα and EUV imagings and white-light coronagraph observations in the near-Sun region. ICMEs are generally detected by in situ observations around the Earth. These observations show that near-Sun CMEs have velocities ranging between few tens and $\approx$ 3000 km s^{-1} (Gopalswamy et al., 2009) while velocities of near-Earth ICMEs have an absolute difference of 30 – 615 km s^{-1} from the ambient solar wind (Jian et al., 2006b). Therefore, many investigators have considered that the interplanetary propagation of CMEs is affected by the interaction with the solar wind.

The fluid mechanics tells us that an object moving through a fluid undergoes the drag force(s) caused by an interaction with the fluid. Two types of drag force model have been proposed for the propagation of ICMEs. Chen and Garren (1993) applied a toroidal loop model (Chen, 1989) to interplanetary magnetic clouds to examine their kinematics. For the interplanetary motion of a toroidal loop, they considered a drag force ($F_{\rm d}$) which was described as follows:

$$F_{\rm d} = {\rm C_d}[N m_{\rm i} d_{\rm t} (V - V_{\rm bg})|V - V_{\rm bg}|], \tag{1.8}$$

where $\rm C_d$, N, $m_{\rm i}$, $d_{\rm t}$, V and $V_{\rm bg}$ are the drag coefficient, number density of ions outside the toroidal loop, ion mass, minor radius of the loop, radial velocity of the loop, and the local speed of the solar wind, respectively, in addition to the electromagnetic force. Their model calculation showed that a loop with a slower initial velocity accelerated to the speed of the solar wind in a distance of 60 solar radii (0.28 AU) from the solar surface. Cargill et al. (1995) studied the motion of a flux tube through a magnetized plasma using the MHD simulation with a drag force $F_{\rm d} \propto V|V|$. In the fluid mechanics, this type of drag force is referred as the frictional drag or aerodynamic drag, which operates on an object moving through a fluid for ${\rm Re} \gg 1$ (e.g. Cargill, 2004; Kundu et al., 2012). Here, Re is the Reynolds number, which is defined as ${\rm Re} = (\rho d U)/\mu$, where ρ, d, U, and μ are the mass density of a fluid, the size and speed of the object, and the viscosity of the fluid, respectively. On the other hand, Vršnak (2001a; 2001b) took a viscous drag force, which was written as follows:

$$F_{\rm d} = \gamma_1 (V - V_{\rm bg}), \tag{1.9}$$

where γ_1 is a coefficient, into account to explain the deceleration of solar eruptions. This drag force acts on an object for ${\rm Re} \ll 1$ and known as Stokes law of resistance (Kundu et al., 2012) or Stokes drag force (Collinson and Roper, 1995). Vršnak and Gopalswamy (2002) proposed a linear drag model ${\rm d}V/{\rm d}t = -\gamma_1 (V - V_{\rm bg})$ for the motion of ICMEs.

Drag force models have been tested by comparing with ICME observations (e.g. Reiner et al., 2003; Tappin, 2006; Byrne et al., 2010; Lara et al., 2011). However, these models are still controversial. Tappin (2006) pointed out that an additional force balancing was required to explain observations of the 5 – 7 April 2003 ICME using both linear and quadratic drag models. Maloney and Gallagher (2010) reported that a linear drag model reproduced well the kinematics of an ICME which had a larger velocity than the solar wind, while the aerodynamic drag model gave an appropriate explanation for the motion of a slow ICME. These earlier articles mainly presented analyses of dynamics for individual ICMEs. Although a case study of the ICME motion is important, we need to make a statistical study to understand general properties of the ICME propagation. A

reason why the kinematics of ICMEs are still not well understood is the smaller number of interplanetary observations between 0.1 and 1 AU than near-Earth in situ measurements. Since 1962, some spacecraft such as the *Mariner-2* and twin *Helios* gave valuable data of ICMEs in the inner heliosphere, while many solar wind observations made around the Earth in the ecliptic plane. Twin STEREO spacecraft bring HI which is a powerful instrument for the remote sensing of ICMEs. However, HI data are not available before 2006, and positions of STEREO are changed year by year because both spacecraft drift ahead and behind the Earth, respectively. It is desirable that observations are made using an instrument at a stationary point during a long period for the statistical study of ICMEs.

We take advantage of IPS observation to examine the kinematics of ICMEs with drag force models. STEL IPS observations at 327 MHz are capable of detecting interplanetary disturbances between 0.2 and 1 AU with a time resolution of 24 hours and then a useful means for the study of the ICME propagation. We analyze the solar wind disturbance factor, the so-called "g-value" (Gapper et al., 1982), obtained from our IPS observations during 1997 – 2011 to identify ICMEs. The SOHO/LASCO CME catalog is used for determination of kinematic properties of near-Sun CMEs. For estimation of properties of near-Earth ICMEs, we use an ICME list by Richardson and Cane (2010) during 1997 – 2009, and identify ICMEs ourselves using criteria of the ICME identification in 2010 and 2011 because there is no catalog. By combining SOHO/LASCO, IPS, and in situ observations, we make the tracking of CMEs/ICMEs from the Sun to the Earth. From statistical examinations of CMEs/ICMEs identified by combined observations, we find general properties of the ICME kinematics. In this study, we assume that the propagation of ICMEs is controlled by the drag force(s) due to interaction with the ambient solar wind, and that the magnitude of drag force(s) is proportional to the difference in speed between the ICME and the solar wind. We propose a modified drag-force equation and provide its physical implication.

This dissertation comprises the following chapters: Chapter 2 describes how do we identify ICMEs from SOHO/LASCO, IPS, and in situ observations and estimate their speeds and accelerations. It also provide analyses of ICMEs during 1997 – 2009 when g-value data were obtained using the Kiso IPS Telescope (KIT: Asai et al., 1995) and a simple expression describing the motion of ICMEs which are faster than the solar wind. The contents of this chapter were published as Iju et al. (2013a; 2013b). Chapter 3 provides analyses of ICMEs during 2010 – 2011 when SWIFT was used for collecting g-value data. In this chapter, we focus on the propagation of slow ICMEs and determine general properties of their kinematics. We also examine ICMEs which have larger velocities than the solar wind again and then propose a modified drag-force equation for their motion with an interpretation of that. The contents of Chapter 3 were published

as Iju et al. (2014). Finally, Chapter 4 summarizes main conclusions of this study and gives our suggestion for future study.

Chapter 2

Kinematics of ICMEs Faster Than the Solar Wind

2.1 Introduction

Coronal mass ejections (CMEs) are transient events in which large amounts of plasma are ejected from the solar corona (e.g. Gosling et al., 1974). Interplanetary counterparts of CMEs are called interplanetary coronal mass ejections (ICMEs). Since ICMEs seriously affect the space environment around the Earth, understanding of their fundamental physics, e.g. generation, propagation, and interaction with the Earth's magnetosphere, is very important for space weather forecasting (e.g. Tsurutani et al., 1988; Gosling et al., 1990). In particular, the dynamics of ICME propagation is one of the key pieces of information for predicting geomagnetic storms.

Propagation of ICMEs has been studied by various methods. Earlier studies combining space-borne coronagraphs with in situ observations revealed that ICME speeds significantly evolve between near-Sun and 1 AU. Schwenn (1983) reported the correlation between CMEs and interplanetary disturbances using the *P78-1/Solwind* coronagraph, the *Helios-1* and -2 solar probes, and a ground-based Hα coronagraph. He showed that fast CMEs associated with flares exhibit no acceleration into interplanetary space, while slow CMEs related to prominence eruptions accelerate. Lindsay et al. (1999) examined the relation between propagation speeds of CMEs observed by the *Solwind* coronagraph and SMM C/P and those of the ICMEs observed by the *Helios-1* and PVO for 31 CMEs and their associated ICMEs. They found a good correlation between the speeds of CMEs and those of ICMEs observed in interplanetary space between 0.7 and 1 AU. They also found that the speeds of most ICMEs range from 380 km s^{-1} to 600 km s^{-1}, while CME speeds show a wider range of from $\approx$ 10 km s^{-1} to 1500 km s^{-1}. These findings suggest

that the ICME speeds tend to converge to an average solar-wind speed as they propagate through interplanetary space. Gopalswamy et al. (2000) determined an effective acceleration for 28 CMEs observed by LASCO (Brueckner et al., 1995) onboard SOHO spacecraft between 1996 and 1998. On the assumption that the acceleration is constant, they found a very good anti-correlation between the accelerations and initial speeds of CMEs, and a critical speed of 405 km s^{-1}; this value is close to the typical speed of the solar wind in the equatorial plane. Following this research, Gopalswamy et al. (2001) described an empirical model for predicting of arrival of the ICMEs at 1 AU; this model is based on their previous work (Gopalswamy et al., 2000) and its accuracy is improved by allowing for cessation of the interplanetary acceleration before 1 AU. They showed that the acceleration cessation distance is 0.76 AU, and this result agrees reasonably well with observations by SOHO, ACE (Stone et al., 1998), and other spacecraft at 1 AU.

We expect that the acceleration or deceleration of ICMEs is controlled by a drag force caused by interaction between ICMEs and the solar wind. Vršnak and Gopalswamy (2002) proposed an advanced model for the motion of ICMEs; this model considered the interaction with solar wind using a simple expression for the acceleration:

$$a = -\gamma_1(V - V_{\rm bg}), \tag{2.1}$$

where γ_1, V, and $V_{\rm bg}$ are the coefficient, ICME speed, and speed of the background solar wind, respectively. They also compared their model with the drag acceleration of the following form:

$$a = -\gamma_2(V - V_{\rm bg})|V - V_{\rm bg}|, \tag{2.2}$$

where γ_2 is the coefficient for this equation; this expression is known as the aerodynamic drag force (e.g. Chen, 1996; Cargill, 2004). Both models have been tested by comparing with CME observations. Tappin (2006) studied the propagation of a CME that occurred on 5 April 2003 using observations by the SOHO/LASCO, SMEI onboard the *Coriolis* satellite, and the *Ulysses* spacecraft. Maloney and Gallagher (2010) derived the three-dimensional kinematics for three ICMEs detected between 2008 and 2009 using STEREO-A and -B spacecraft observations. Temmer et al. (2011) examined the influence of the solar wind on the propagation of some ICMEs using the STEREO-A and -B spacecraft. Although the propagation of ICMEs has been studied by many investigators, their dynamics is still not well understood. This is mainly due to the lack of observational data about ICMEs between 0.1 and 1 AU. Almost all ICME observations are currently limited to the near-Earth area in the equatorial plane.

Remote sensing using radio waves is a suitable method for collecting global data on ICMEs. For example, Reiner et al. (2007) derived kinematic parameters for 42

ICME/shocks from measurements of type-II radio emission. Woo (1988) studied the shock propagation using Doppler-scintillation measurements of radio waves emitted from planetary spacecraft, and showed the speed profiles of shocks between 0.05 and 0.93 AU. In addition to these measurements, interplanetary scintillation (IPS) is a type of remote sensing. IPS is a phenomenon where signals from a point-like radio source, such as quasars and active galactic nuclei, fluctuate due to density irregularities in the solar wind (Hewish et al., 1964). IPS observations allow us to probe the inner heliosphere using many radio sources, and this is a useful means to study the global structure and propagation dynamics of ICMEs in the solar wind (e.g. Tappin et al., 1983; Watanabe and Kakinuma, 1986; Janardhan et al., 1996; Tokumaru et al., 2000a, 2003; Manoharan et al., 2000; Jackson and Hick, 2002; Bisi et al., 2010; Jackson et al., 2011; Manoharan, 2010; see also Watanabe and Schwenn, 1989). For the kinematics of interplanetary disturbances, Vlasov (1988; 1992) reported that the radial dependence of speed can be represented by a power-law function ($V \approx R^{-\alpha}$) with α in the range $0.25 < \alpha < 1$ from analysis of all-sky scintillation-indices maps. Manoharan (2006) examined radial evolution of 30 CMEs observed by SOHO/LASCO, ACE, and ORT between 1998 and 2004. He showed that most CMEs tend to attain the speed of the ambient flow at 1 AU and also reported a power-law form of radial-speed evolution for these events.

We take advantage of IPS observation to determine the ICME speed and acceleration. In the current study, we analyze the solar wind disturbance factor (g-value) derived from IPS observations during 1997 – 2009 covering nearly the whole of Solar Cycle 23 and make a list of disturbance event days in the period. We define an "ICME" as a series of events including a near-Sun CME, an interplanetary disturbance, and a near-Earth ICME in this study. By comparing our list with that of CME/ICME pairs, we identify many events that are detected at three locations between the Sun and the Earth's orbit, i.e. near-Sun, interplanetary space, and near-Earth, and derive their radial speed profiles. We then analyze the relationship between the acceleration and speed difference for the ICMEs. The outline of this chapter is as follows: Section 2.2 describes the IPS observations made with the 327 MHz radio-telescope system of STEL, Nagoya University. Section 2.3 describes the criteria for ICME identification and the method for estimating ICME speeds and accelerations between the corona and 1 AU. Section 2.4 provides the radial-speed profiles of ICMEs and the analyses of the propagation properties. Section 2.5 discusses the results.

2.2 Observation and Data

STEL IPS observations have been carried out regularly since the early 1980s using multiple ground-based radio-telescope stations operated at 327 MHz (Kojima and Kakinuma, 1990; Asai et al., 1995). The IPS observations at 327 MHz allow us to determine the solar wind condition between 0.2 and 1 AU with a cadence of 24 hours. In our observations, nearly 30 radio sources within a solar elongation of 90° are observed daily between April and December. The IPS observations on a given day are made when each radio source traverses the local meridian.

The solar wind speed and disturbance factor, the so-called "g-value" (Gapper et al., 1982), are derived from IPS observations. A g-value is calculated for each source using the following equation:

$$g = \frac{\Delta S}{\Delta S_{\rm m}(\varepsilon)}, \tag{2.3}$$

where ΔS and $\Delta S_{\rm m}(\varepsilon)$ are the observed fluctuation level of radio signals and their yearly mean, respectively. $\Delta S_{\rm m}(\varepsilon)$ varies with the solar elongation angle (ε) for a line-of-sight (LOS) from an observed radio source to a telescope. When a radio signal is weakly scattered, the g-value is given by the following equation (Tokumaru et al., 2003, 2006):

$$g^2 = \frac{\int_0^\infty {\rm d}z\{\Delta N_{\rm e}(\theta,\phi,r)\}^2\omega(z)}{\int_0^\infty {\rm d}z\{\Delta N_{\rm e0}(\theta,\phi,r)\}^2\omega(z)}, \tag{2.4}$$

where, z is the distance along a LOS, θ and ϕ are the heliographic longitude and latitude respectively, r is the radial distance from the Sun, $\Delta N_{\rm e}(\theta,\phi,r)$ is the observed fluctuation level of plasma (electron) density, $\Delta N_{\rm e0}(\theta,\psi,r)$ is the yearly mean of $\Delta N_{\rm e}(\theta,\phi,r)$, and $\omega(z)$ is the IPS weighting function (Young, 1971) in a weak scattering condition. The $\omega(z)$ is given by the following formula (Tokumaru et al., 2003):

$$\omega(z) = \int_0^\infty {\rm d}k k^{1-q} \sin^2\left(\frac{k^2 z\lambda}{4\pi}\right) \exp\left(-\frac{k^2 z^2 \Theta^2}{2}\right), \tag{2.5}$$

where, k, q, λ, and Θ are the spatial wavenumber of density fluctuations, the spectral index of the density turbulence, the wavelength for observing frequency, and the apparent angular size of a radio source, respectively. We note that $\Delta N_{\rm e}$ is nearly proportional to the solar wind density ($N_{\rm e}$); $\Delta N_{\rm e} \propto N_{\rm e}$ (Coles et al., 1978), and the weak-scattering condition holds for $R > 0.2$ AU, where R is the radial distance from the Sun.

A g-value represents the relative level of density fluctuation integrated along a LOS. For quiet solar wind conditions, the g-value is around unity. With dense plasma or high turbulence as an ICME passes across a LOS, the g-value becomes greater than unity because of the $\Delta N_{\rm e}$ ($\propto N_{\rm e}$) increase. In contrast, a g-value less than unity indicates a

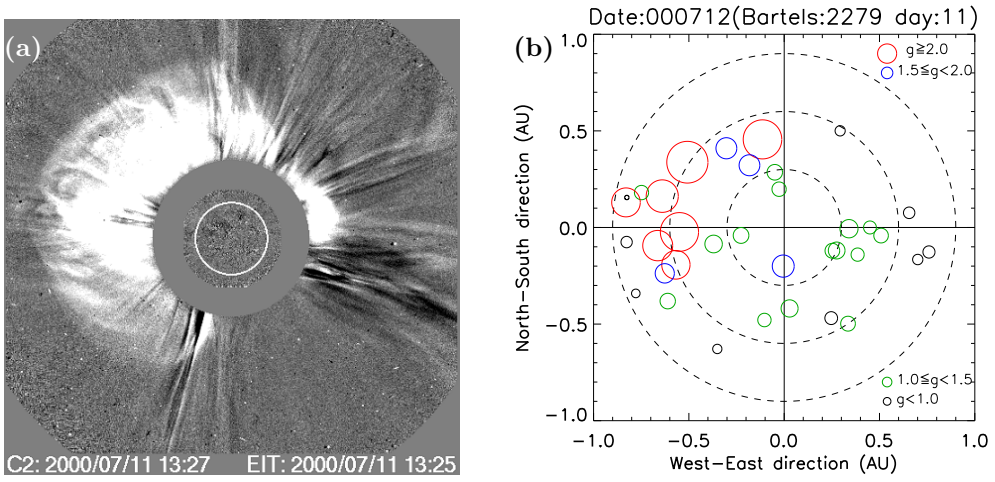

FIGURE 2.1: (a) White-light difference image for the halo CME on 11 July 2000 from the SOHO/LASCO-C2 coronagraph (adopted from the web page of the SOHO/LASCO CME catalog), and (b) a g-map obtained from our IPS observations on 12 July 2000. The g-map center corresponds to the location of the Sun, and concentric circles indicate radial distances of 0.3 AU, 0.6 AU, and 0.9 AU. Colored open solid circles indicate the locations of the closest point to the Sun (the P-point) on the line-of-sight (LOS) for the radio sources in the sky plane. The center of the colored circle indicates the heliocentric distance of the P-point on the LOS, and color and diameter represent the g-value level for each source. We use four bins of $g < 1.0$ (black), $1.0 \leq g < 1.5$ (green), $1.5 \leq g < 2.0$ (blue), and $g \geq 2.0$ (red) for the g-map. A group of P-points with red or blue circles indicates a disturbance related to the 11 July 2000 CME.

rarefaction of the solar wind. Hence, detecting an abrupt increase in g-value is a useful means to detect an ICME.

The location of the LOS for a radio source exhibiting a g-value enhancement in the sky plane indicates a turbulent region is present. A sky-map of enhanced g-values for the sources observed in a day is called a "g-map" (Gapper et al., 1982; Hewish and Bravo, 1986). This map provides information on the spatial distribution of ICMEs. Figure 1 shows an example of a g-map for a CME event. A white-light difference image of a CME observed by the SOHO/LASCO-C2 coronagraph is shown in the left-hand panel of Figure 2.1. As shown here, a bright balloon-like structure was observed on the northeast limb on 11 July 2000. This event was reported as an asymmetric halo CME in the SOHO/LASCO CME Catalog (Yashiro et al., 2004; Gopalswamy et al., 2009; available at `cdaw.gsfc.nasa.gov/CME_list/`). The right-hand panel of Figure 2.1 is a g-map derived from our IPS observation on 12 July 2000. The center of the map corresponds to the location of the Sun, and the horizontal and vertical axes are parallel to the East–West and North–South directions, respectively. The concentric circles indicate the radial distances to the closest approach of the LOS of 0.3 AU, 0.6 AU, and 0.9 AU. Since ten LOS between 0.4 and 0.7 AU in the eastern hemisphere (left-hand side of g-map) exhibit high g-values, a group of them is considered as the interplanetary counterpart of the 11 July 2000 CME event. This CME was also detected by in situ observation at 1 AU on

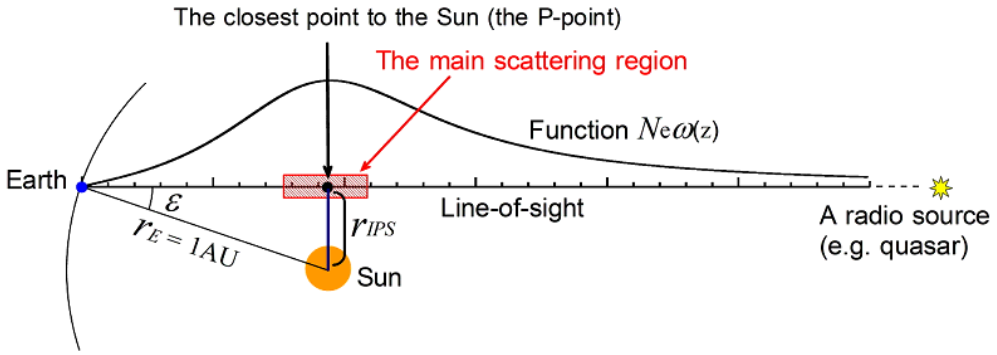

FIGURE 2.2: Schematic explanation of an IPS along a line-of-sight (LOS) and the P-point approximation. A function $N_e\omega(z)$ shows the contribution of radio wave scattering to the IPS with a distance along the LOS, which have a maximum at the closest point to the Sun (the P-point). For the P-point approximation, almost the entire of the wave scattering occurs in the main scattering region with a length of $\approx r_{\rm IPS}$, which contains the P-point.

13 July 2000 and reported as a near-Earth ICME (Richardson and Cane, 2010). In a g-map, the radial distance ($r_{\rm IPS}$) for each LOS is given by $r_{\rm IPS} = r_{\rm E} \sin\varepsilon$, where $r_{\rm E}$ is the distance between the Sun and the Earth, i.e. 1 AU and ε is the solar elongation angle for the LOS. This calculation is based on the approximation that a large fraction of IPS is given by the wave scattering at the closest point to the Sun (the P-point) on a LOS (Hewish et al., 1964). Figure 2.2 exhibits an explanation of an IPS along a LOS and the P-point approximation. In this way, a g-map can visualize an ICME between 0.2 and 1 AU. The g-value data have been available from our IPS observation since 1997 (Tokumaru et al., 2000b) and obtained by KIT between 1997 and 2009. To find the g-value enhancements due to ICMEs from the g-value data, we define criteria for the ICME identifications as mentioned in the next section.

2.3 Method

2.3.1 Criteria for ICME Identification

First, we define disturbance days due to an ICME in the IPS data. In this determination, we consider a threshold g-value and the number of sources exhibiting the threshold or beyond. The average (a_g) and standard deviation (σ_g) for the g-values obtained by STEL IPS observations between 1997 and 2009 are 1.07 and 0.47, respectively. From these, we regard a g-value for a disturbed condition on a given day to be $a_g + \sigma_g$ or more, and we decide to use 1.5 as this threshold. We also define an "observation day" as a day on which 15 or more sources are observed by our radio-telescope system; this minimum number is equal to half the mean number of sources observed in a day. In an observation

day, when five or more sources showed a disturbed condition, we judge that a disturbance had occurred. Combining the above criteria, we define an "IPS disturbance event day" (IDED) as a day on which $g \geq 1.5$ sources numbered five or more on an observation day. Using this definition, we find 656 IDEDs in the period of our research. From these, we eliminate periods with four or more consecutive IDEDs because they are likely related to CIRs (Gapper et al., 1982). However, we do not eliminate two periods including the 2000 Bastille Day and 2003 Halloween events from among the IDEDs above, because consecutive disturbances in them are caused by successive CMEs (e.g. Andrews, 2001; Gopalswamy et al., 2005). As a result, 159 out of 656 IDEDs are excluded, and the remaining 497 IDEDs are listed as candidates for ICME events.

Next, we examine the relationship between CME/ICME pairs and selected IDEDs. In this examination, we use the list of near-Earth ICMEs and associated CMEs compiled by Richardson and Cane (2010). This includes 322 ICMEs associated with a halo or a partial halo or normal CMEs during Solar Cycle 23; here, "normal" means that the exterior of CME is neither a halo nor a partial halo. In the above study, CMEs were observed by the SOHO/LASCO coronagraphs, and ICMEs were detected by in situ observation using spacecraft such as ACE and IMP-8. We compare the list of IDEDs with that of ICMEs using the assumption that an ICME is responsible for an IDED. When an IDED is between the appearance date of an associated CME and the detection date of a near-Earth ICME, we assume that the IDED was related to the ICME.

Using the above method, we find 66 IDEDs from our list that were probably related to ICMEs. However, we also find that 16 IDEDs of the 66 had multiple associated CMEs. For these 16 events, we identify the optimal one-to-one correspondence by comparing positions for LOS exhibiting high g-values in a g-map with the direction of the associated CME eruption in the LASCO FOV.

At the end of this selection, we identify 50 CMEs and their associated ICMEs that were detected by the SOHO/LASCO, IPS, and in situ observations. For these, we estimate radial speeds and accelerations in interplanetary space using the method described in the next subsection.

2.3.2 Calculations of ICME Kinematic Properties

The ICME radial speeds and accelerations are estimated in two interplanetary regions, i.e. the region between SOHO and IPS observations (the SOHO–IPS region, from 0.1 to $\approx$ 0.6 AU) and that between IPS and in situ observations (the IPS–Earth region, from $\approx$ 0.6 to 1 AU). In these estimations, we assume that locations of P-point on LOS for disturbed sources in a g-map give the location of an ICME. From IPS observations in

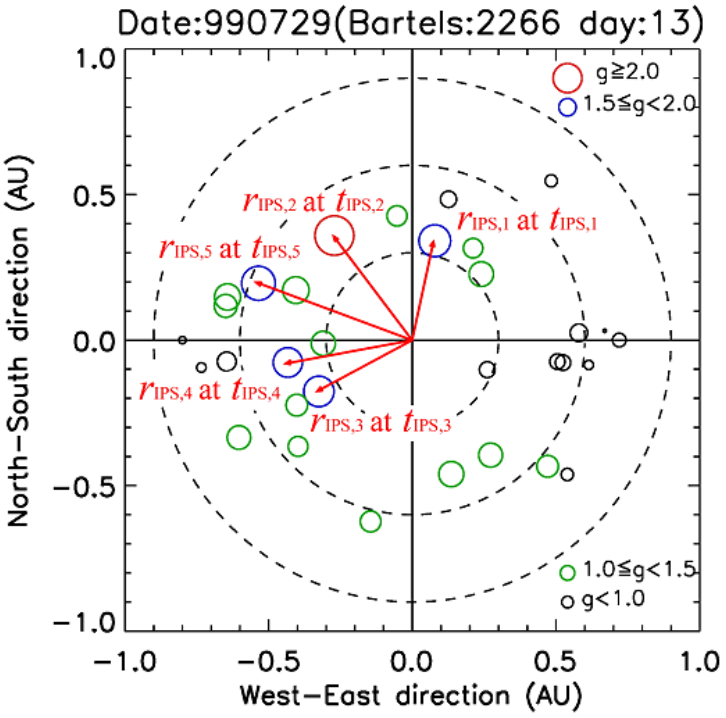

FIGURE 2.3: Radial distance of the P-point from the Sun ($r_{\rm IPS}$) and the observation time ($t_{\rm IPS}$) for each radio source with $g \geq 1.5$ in the 29 July 1999 g-map. In this g-map, five $g \geq 1.5$ sources are indicated by red and blue circles. Arrows from the the g-map center denote distances of the $g \geq 1.5$ sources.

a day, we derive the radial distance of P-point from the Sun ($r_{\rm IPS}$) and the observation time ($t_{\rm IPS}$) for each radio source with $g \geq 1.5$. Figure 2.3 shows the determination of $r_{\rm IPS}$ and $t_{\rm IPS}$ for five $g \geq 1.5$ sources in a g-map on July 29, 1999 as an example of that. In this way, we obtain values of $r_{\rm IPS}$ and $t_{\rm IPS}$ for all $g \geq 1.5$ sources on a given day.

First, we calculate radial speeds at reference distances for each ICME. For each radio source with $g \geq 1.5$ in a g-map, distances (r_1 and r_2) and radial speeds (v_1 and v_2) are derived from the following equations:

$$r_1 = \frac{r_{\rm S} + r_{\rm IPS}}{2}, \; v_1 = \frac{r_{\rm IPS} - r_{\rm S}}{t_{\rm IPS} - T_{\rm SOHO}} \text{ (for the SOHO–IPS region)}, \tag{2.6}$$

and

$$r_2 = \frac{r_{\rm IPS} + r_{\rm E}}{2}, \; v_2 = \frac{r_{\rm E} - r_{\rm IPS}}{T_{\rm Earth} - t_{\rm IPS}} \text{ (for the IPS–Earth region)}, \tag{2.7}$$

respectively. Here, $r_{\rm S}$ is the minimum radius of SOHO/LASCO-C2 FOV, i.e. 0.009 AU, $r_{\rm E}$ is the distance between the Sun and the Earth, i.e. 1 AU, $T_{\rm SOHO}$ is the appearance time of CME in the SOHO/LASCO-C2 FOV, and $T_{\rm Earth}$ is the onset time of near-Earth ICME by in situ observation. Using these values, the reference distances (R_1 and R_2)

and the radial speeds (V_1 and V_2) for the ICME are estimated as the arithmetric averages of r_1, r_2, v_1, and v_2 for all $g \geq 1.5$ sources, respectively, on a given day.

Next, we calculate accelerations using the above values. In these calculations, we use the approximation that the accelerations are constant within each region. The average accelerations, i.e. a_1 and a_2, for ICMEs were given by

$$a_1 = \frac{1}{n}\sum_{k=1}^{n}\frac{v_{\mathrm{IPS},k} - V_{\mathrm{SOHO}}}{t_{\mathrm{IPS},k} - T_{\mathrm{SOHO}}} \text{ (for the SOHO–IPS region)}, \tag{2.8}$$

and

$$a_2 = \frac{1}{n}\sum_{k=1}^{n}\frac{V_{\mathrm{Earth}} - v_{\mathrm{IPS},k}}{T_{\mathrm{Earth}} - t_{\mathrm{IPS},k}} \text{ (for the IPS–Earth region)}, \tag{2.9}$$

respectively. Here,

$$v_{\mathrm{IPS},k} = \frac{v_{1,k} + v_{2,k}}{2}, \tag{2.10}$$

$t_{\mathrm{IPS},k}$ is the observation time for each $g \geq 1.5$ source, n is the number of $g \geq 1.5$ sources, and V_{SOHO} and V_{Earth} are the radial speed of the CME and of the near-Earth ICME, respectively. For the value of V_{SOHO} in the halo or the partial halo CMEs, we use

$$V_{\mathrm{SOHO}} = 1.20 \times V_{\mathrm{POS}}, \tag{2.11}$$

where V_{POS} is the speed measured in the sky plane by the SOHO/LASCO, because the coronagraph measurement for them tends to underestimate the radial speed (Michalek et al., 2003), while we use $V_{\mathrm{SOHO}} = V_{\mathrm{POS}}$ for the normal ones. In this study, we use the linear speeds reported in the SOHO/LASCO CME Catalog (`cdaw.gsfc.nasa.gov/CME_list/index.html`) for those of V_{POS} with a 0.08 AU reference distance corresponding to half the LASCO FOV value. Those are derived from the bright leading edges of CME (Yashiro et al., 2004), while the associated shocks show a faint structure ahead of them (Ontiveros and Vourlidas, 2009), and then indicate the speeds of CME itself in the sky plane (Vourlidas et al., 2012). For values of V_{Earth}, we use the average ICME speeds listed by Richardson and Cane (2010). We note that the values of V_{SOHO} and V_{Earth} represent an average in the near-Sun and near-Earth regions, respectively, and V_1, V_2, a_1, and a_2 are averages in the interplanetary space. The ICME speeds in the near-Earth region are measured when the spacecraft passes through them. Thus, those are equivalent to the plasma flow speed on the trajectory of the spacecraft during the passage of an ICME, indicated by the enhancement of the charge state and the rotation of magnetic-field direction (Richardson and Cane, 2010). The speed of the solar wind measured by in situ observations is sometimes highly variable during the passage of an ICME. However, the majority of ICMEs listed by them have only < 100 km s^{-1}

difference between the peak and average speeds. Hence, we consider it justified that the average flow speed can be used as the propagation speed of ICMEs.

2.3.3 Classification of ICMEs

Here, we introduce $V_{\rm IPS}$, which is given as the average value of $v_{\rm IPS}$ for each ICME; the $v_{\rm IPS}$ is derived from Equation 2.10. In addition, we also introduce the speed of the background solar wind ($V_{\rm bg}$), which is estimated as the average speed of a plasma stream without ICMEs at the Earth. To determine the value of $V_{\rm bg}$, we use plasma data obtained by space-borne instruments including *Solar Wind Electron, Proton, and Alpha Monitor* onboard ACE (ACE/SWEPAM: McComas et al., 1998), *Solar Wind Experiment* on *Wind* (Wind/SWE: Ogilvie et al., 1995), *Massachusetts Institute of Technology Faraday cup experiment* on IMP-8 (IMP-8/MIT: Bellomo and Mavretic, 1978), and the *Comprehensive Plasma Instrumentation* on GEOTAIL (GEOTAIL/CPI: Frank et al., 1994); these are determined from the NASA/GSFC OMNI dataset through OMNIWeb Plus (`omniweb.gsfc.nasa.gov/`). From these data, we calculate the average solar wind speed between $T_{\rm SOHO}$ and $T_{\rm Earth}$ for each ICME event.

Using the values of $V_{\rm SOHO}$, $V_{\rm IPS}$, and $V_{\rm bg}$, we classify the 50 ICMEs into three types: fast ($V_{\rm SOHO}-V_{\rm bg} > 500$ km s^{-1}), moderate (0 km s^{-1} $\leq V_{\rm SOHO}-V_{\rm bg} \leq 500$ km s^{-1}), and slow ($V_{\rm SOHO}-V_{\rm bg} < 0$ km s^{-1}). In our results, the numbers of fast, moderate, and slow ICMEs are 19, 25, and 6, respectively. Here, we eliminate 5 of the 19 fast ICMEs and a moderate ICME because they show an extreme zigzag profile of propagation speeds, i.e. $V_1 - V_2 > 1000$ km s^{-1}. The value of $V_1 - V_2 > 1000$ km s^{-1} implies that the ICME has a strange acceleration, and then shows an unrealistic propagation. We also eliminate 4 of the 24 moderate ICMEs and one of the six slow ones because they exhibit the unusual values of $V_{\rm IPS}$ of $V_{\rm IPS} - V_{\rm bg} > 500$ km s^{-1} and $V_{\rm IPS} - V_{\rm bg} > 100$ km s^{-1}, respectively. The values of $V_{\rm IPS} - V_{\rm bg} > 500$ km s^{-1} for moderate and $V_{\rm IPS} - V_{\rm bg} > 100$ km s^{-1} for slow ICMEs imply that the ICME has a strange acceleration since $V_{\rm IPS}$ is larger than $V_{\rm SOHO}$ and $V_{\rm Earth}$, and an unrealistic ICME propagation that indicates a higher speed in the region beyond coronagraph distances, and less at 1 AU.

Finally, we obtain physical properties for 39 ICMEs which consist of 14 fast, 20 moderate, and five slow ones.

2.4 Results

2.4.1 Properties of the 39 ICMEs

Kinematic properties of the 39 ICMEs identified from our analysis are listed in Tables 2.1 and 2.2 which including $T_{\rm IPS}$, R_0, α, β, and $V_{\rm Tr}$ in addition to $T_{\rm SOHO}$, $V_{\rm POS}$, $V_{\rm SOHO}$, R_1, V_1, a_1, R_2, V_2, a_2, $T_{\rm Earth}$, $V_{\rm Earth}$, and $V_{\rm bg}$ above. Here, $T_{\rm IPS}$ and R_0 are the mean time and the average radial distance for an ICME detected by IPS observations; those are given as the averages of $t_{\rm IPS}$ and of $r_{\rm IPS}$ for the $g \geq 1.5$ sources, respectively. The α and β are the index and coefficient for a power-law form of the radial speed evolution described as

$$V = \beta R^{\alpha}, \tag{2.12}$$

where R is the heliocentric distance. $V_{\rm Tr}$ is the transit speed:

$$V_{\rm Tr} = \frac{r_{\rm E}}{T_{\rm Earth} - T_{\rm SOHO}}. \tag{2.13}$$

This is equivalent to the average speed of ICMEs between the Sun and the Earth. For the 39 ICMEs, their g-maps are presented in Figures A.1 – A.7 in Appendix A. In addition, we plot all of the speed profiles in order to show radial speed evolutions of ICMEs in Figure 2.4. Here, data points for each ICME are connected by solid lines instead of fitting in Equation (2.12). As shown here, ICME propagation speeds in the near-Sun region exhibit a wide range from 90 km s^{-1} to $\approx$ 2100 km s^{-1}, while those in the near-Earth region range from 310 km s^{-1} to 790 km s^{-1}. Moreover, the range of ICME propagation speeds in interplanetary space decreases with increasing distance. In addition, speeds of the background solar wind also show a relatively narrow span from 286 km s^{-1} to 662 km s^{-1}.

TABLE 2.1: Properties derived from SOHO/LASCO observations and those in the SOHO–IPS region derived from IPS observations for 39 ICMEs during 1997 – 2009.

No.	SOHO/LASCO						IPS									
									Disturbance		SOHO–IPS region					
	Date	Time	V_{POS}	V_{SOHO}	CME	PA	Date	Time	R_0 [AU]		R_1 [AU]		V_1 [km s^{-1}]		a_1 [m s^{-2}]	
	[ddmmmyyyy]	[hhmm]	[km s^{-1}]	[km s^{-1}]	Type	[deg]	[ddmmmyyyy]	[hhmm]	Aver.	σ	Aver.	σ	Aver.	σ	Aver.	σ
1	06 Dec 1997	1027	397	476	PH	317	09 Dec 1997	0115	0.61	0.13	0.35	0.07	399	93	− 0.34	0.36
2	29 Apr 1998	1658	1374	1649	FH	−99	01 May 1998	0358	0.51	0.22	0.29	0.11	584	243	− 7.55	1.47
3	04 Nov 1998	0754	523	628	FH	−99	06 Nov 1998	0259	0.60	0.10	0.34	0.05	570	116	− 0.95	0.45
4	05 Nov 1998	2044	1118	1342	FH	−99	07 Nov 1998	0143	0.55	0.16	0.32	0.08	782	257	− 7.20	1.36
5	13 Apr 1999	0330	291	349	PH	228	15 Apr 1999	0453	0.55	0.16	0.32	0.08	456	130	0.71	0.55
6	24 Jun 1999	1331	975	1170	FH	−99	26 Jun 1999	0114	0.61	0.10	0.35	0.05	705	135	− 4.96	0.61
7	28 Jul 1999	0430	361	433	PH	112	29 Jul 1999	0408	0.44	0.09	0.26	0.04	747	135	2.74	0.79
8	28 Jul 1999	0906	462	554	FH	−99	30 Jul 1999	0438	0.60	0.12	0.34	0.06	557	97	− 0.37	0.43
9	17 Aug 1999	1331	776	931	PH	61	19 Aug 1999	0403	0.60	0.14	0.34	0.07	635	138	− 3.04	0.67
10	21 May 2000	0726	629	755	PH	304	23 May 2000	0311	0.50	0.07	0.29	0.03	469	60	− 1.31	0.29
11	31 May 2000	0806	391	469	PH	46	03 Jun 2000	0417	0.52	0.18	0.30	0.09	312	105	− 0.32	0.37
12	07 Jul 2000	1026	453	544	FH	−99	09 Jul 2000	0345	0.57	0.20	0.33	0.10	559	180	− 0.49	0.80
13	11 Jul 2000	1327	1078	1294	FH	−99	12 Jul 2000	0459	0.56	0.17	0.32	0.09	1446	373	− 5.27	3.60
14	17 Jul 2000	0854	788	788	NM	95	19 Jul 2000	0421	0.59	0.10	0.34	0.05	557	78	− 0.65	0.56
15	06 Aug 2000	1830	233	280	PH	105	09 Aug 2000	0503	0.62	0.14	0.35	0.07	432	95	0.68	0.40
16	09 Aug 2000	1630	702	842	FH	−99	11 Aug 2000	0446	0.54	0.12	0.31	0.06	600	123	− 1.12	0.78
17	29 Aug 2000	1830	769	923	PH	347	01 Sep 2000	0106	0.70	0.06	0.39	0.03	530	57	− 2.65	0.19
18	08 Nov 2000	2306	1738	2086	PH	271	10 Nov 2000	0017	0.64	0.16	0.36	0.08	1053	283	−14.60	1.88
19	11 Apr 2001	1331	1103	1324	FH	−99	12 Apr 2001	0334	0.44	0.20	0.26	0.10	1239	477	− 6.38	4.77
20	14 Aug 2001	1601	618	742	FH	−99	16 Aug 2001	0341	0.44	0.08	0.26	0.04	507	97	− 1.57	0.45

(Continued from the previous page)

No.	SOHO/LASCO						IPS									
									Disturbance		SOHO–IPS region					
	Date	Time	V_{POS}	V_{SOHO}	CME	PA	Date	Time	R_0 [AU]		R_1 [AU]		V_1 [km s^{-1}]		a_1 [m s^{-2}]	
	[ddmmmyyyy]	[hhmm]	[km s^{-1}]	[km s^{-1}]	Type	[deg]	[ddmmmyyyy]	[hhmm]	Aver.	σ	Aver.	σ	Aver.	σ	Aver.	σ
21	25 Aug 2001	1650	1433	1720	FH	−99	27 Aug 2001	0337	0.64	0.11	0.36	0.06	758	122	− 7.85	0.85
22	28 Sep 2001	0854	846	1015	FH	−99	29 Sep 2001	0220	0.56	0.13	0.32	0.06	1334	359	− 2.72	2.84
23	22 Oct 2001	1826	618	618	NM	131	25 Oct 2001	0116	0.56	0.20	0.32	0.10	425	171	− 1.11	0.58
24	25 Oct 2001	1526	1092	1310	FH	−99	27 Oct 2001	0137	0.51	0.09	0.30	0.04	617	136	− 6.94	0.55
25	17 Nov 2001	0530	1379	1655	FH	−99	18 Nov 2001	0229	0.50	0.08	0.29	0.04	991	222	−12.23	1.45
26	29 Jul 2002	1207	562	674	PH	13	31 Jul 2002	0212	0.48	0.10	0.28	0.05	519	117	− 1.52	0.47
27	05 Sep 2002	1654	1748	2098	FH	−99	07 Sep 2002	0503	0.65	0.19	0.37	0.10	733	192	−10.98	1.13
28	28 May 2003	0050	1366	1639	FH	−99	29 May 2003	0210	0.51	0.15	0.30	0.07	838	275	− 8.72	2.05
29	14 Jun 2003	0154	875	1050	PH	26	15 Jun 2003	0311	0.63	0.10	0.36	0.05	1038	194	− 4.30	1.10
30	14 Aug 2003	2006	378	454	FH	−99	17 Aug 2003	0409	0.68	0.12	0.38	0.06	497	106	0.62	0.63
31	22 Jul 2004	0731	700	840	PH	66	23 Jul 2004	0406	0.62	0.12	0.35	0.06	1228	158	0.06	1.28
32	12 Sep 2004	0036	1328	1594	FH	−99	13 Sep 2004	0405	0.50	0.11	0.29	0.05	741	138	− 9.40	0.84
33	26 May 2005	1506	586	703	FH	−99	28 May 2005	0334	0.66	0.16	0.37	0.08	738	161	− 1.38	0.75
34	26 May 2005	2126	420	504	PH	144	29 May 2005	0522	0.70	0.08	0.39	0.04	513	49	− 0.57	0.18
35	07 Jul 2005	1706	683	820	FH	−99	09 Jul 2005	0347	0.47	0.12	0.27	0.06	549	132	− 1.44	0.74
36	05 Aug 2005	0854	494	593	PH	23	07 Aug 2005	0547	0.69	0.13	0.39	0.07	632	115	− 0.78	0.48
37	26 Aug 2006	2057	786	943	PH	164	28 Aug 2006	0425	0.57	0.19	0.32	0.09	736	250	− 3.83	1.17
38	12 Sep 2008	1030	91	91	NM	89	14 Sep 2008	0449	0.58	0.10	0.33	0.05	556	96	2.04	0.34
39	29 May 2009	0930	139	139	NM	258	01 Jun 2009	0148	0.56	0.18	0.32	0.09	353	116	0.72	0.32

Column: (1) Event number; (2) – (3) Appearance date [ddmmmyyyy] and time [hhmm] of an ICME–associated CME observed by SOHO/LASCO;(4) Speed in the sky plane measured by SOHO/LASCO with 0.08 AU of reference distance; (5) Radial speed estimated using $V_{SOHO} = 1.20 \times V_{POS}$; (6) Type of CME [FH, PH, and NM mean Full Halo, Partial Halo, and Normal CME, respectively]; (7) Position angle measured from solar North in degrees (counter-clockwise)[−99 means Full Halo]; (8) – (9) Observation date [ddmmmyyyy] and mean time [hhmm] of IPS disturbance event day ; (10) – (11) Average and standard errors for the distance of observed disturbance [R_0]; (12) – (13) Average and standard deviation for the reference distance [R_1] (in the SOHO–IPS region); (14) – (15) Average and standard error for the speed [V_1] (in the SOHO–IPS region); (16) – (17) Average and standard deviation for acceleration [a_1] (in the SOHO–IPS region).

TABLE 2.2: Properties in the IPS–Earth region derived from IPS observations, detection dates, times, and speeds obtained by in situ observations at 1 AU, fitting parameters and speeds of the background solar wind for 39 ICMEs during 1997 – 2009.

No.	IPS						in situ			Parameters for power-law equation			Background	
	IPS–Earth region													
	R_2 [AU]		V_2 [km s^{-1}]		a_2 [m s^{-2}]		Date	Time	V_{Earth}	Index	Coefficient	wind V_{Tr}	V_{bg} [km s^{-1}]	
	Aver.	σ	Aver.	σ	Aver.	σ	[ddmmmyyyy]	[hhmm]	[km s^{-1}]	α	β	[km s^{-1}]	Aver.	σ
1	0.81	0.07	401	153	−0.35	0.56	10 Dec 1997	1800	350	−0.102	366.9	401	354	24
2	0.75	0.11	809	335	−1.95	2.06	02 May 1998	0500	520	−0.374	547.2	692	369	47
3	0.80	0.05	391	105	−0.20	0.45	07 Nov 1998	2200	450	−0.167	426.9	482	385	27
4	0.78	0.08	399	145	−0.82	0.83	09 Nov 1998	0100	450	−0.478	411.5	544	385	27
5	0.78	0.08	495	165	−0.49	0.73	16 Apr 1999	1800	410	0.094	465.0	480	398	15
6	0.81	0.05	361	101	0.85	0.48	27 Jun 1999	2200	670	−0.340	483.9	516	306	31
7	0.72	0.04	587	80	−0.33	0.47	30 Jul 1999	2000	620	0.111	658.4	654	377	43
8	0.80	0.06	436	112	−0.12	0.49	31 Jul 1999	1900	480	−0.080	466.9	507	545	22
9	0.80	0.07	385	134	−0.32	0.60	20 Aug 1999	2300	460	−0.325	416.8	510	635	67
10	0.75	0.03	630	78	−0.17	0.38	24 May 2000	1200	530	−0.098	530.8	542	579	7
11	0.76	0.09	470	173	0.53	0.60	04 Jun 2000	2200	470	0.022	433.4	378	462	55
12	0.79	0.10	381	177	−0.18	0.71	11 Jul 2000	0200	440	−0.120	423.0	474	371	13
13	0.78	0.09	566	199	−3.46	1.75	13 Jul 2000	1300	610	−0.347	638.2	874	500	24
14	0.80	0.05	816	170	−2.12	1.18	20 Jul 2000	0100	530	−0.079	611.8	648	574	43
15	0.81	0.07	414	149	0.06	0.62	10 Aug 2000	1900	430	0.165	447.8	430	412	36
16	0.77	0.06	793	186	−1.33	1.17	12 Aug 2000	0500	580	−0.090	634.9	686	412	36
17	0.85	0.03	276	59	0.11	0.23	02 Sep 2000	2200	420	−0.398	340.2	417	529	47
18	0.82	0.08	473	218	0.25	1.49	11 Nov 2000	0800	790	−0.492	600.6	730	650	184
19	0.72	0.10	782	253	−2.69	2.28	13 Apr 2001	0900	730	−0.253	753.9	955	537	26
20	0.72	0.04	573	85	−0.27	0.40	17 Aug 2001	2000	500	−0.125	502.2	546	395	43

(Continued from the previous page)

No.	IPS						in situ			Parameters for power-law equation			Background	
	IPS–Earth region													
	R_2 [AU]		V_2 [km s^{-1}]		a_2 [m s^{-2}]		Date	Time	$V_{\rm Earth}$	Index	Coefficient	wind $V_{\rm Tr}$	$V_{\rm bg}$ [km s^{-1}]	
	Aver.	σ	Aver.	σ	Aver.	σ	[ddmmmyyyy]	[hhmm]	[km s^{-1}]	α	β	[km s^{-1}]	Aver.	σ
21	0.82	0.06	722	194	−3.43	1.44	28 Aug 2001	0000	490	−0.441	545.6	752	410	21
22	0.78	0.06	341	100	−1.78	0.92	01 Oct 2001	0800	490	−0.397	467.5	584	513	33
23	0.78	0.10	374	192	0.11	0.64	27 Oct 2001	0300	420	−0.175	379.7	397	393	32
24	0.76	0.04	298	61	−0.39	0.28	29 Oct 2001	2200	360	−0.569	306.2	405	393	32
25	0.75	0.04	477	83	−1.93	0.70	19 Nov 2001	2200	430	−0.553	435.4	644	399	20
26	0.74	0.05	414	81	−0.03	0.34	02 Aug 2002	0600	460	−0.175	424.9	462	428	34
27	0.83	0.10	609	266	−2.42	1.78	08 Sep 2002	0400	470	−0.562	482.9	703	400	22
28	0.76	0.07	858	274	−2.91	2.19	30 May 2003	0200	600	−0.344	649.3	844	662	32
29	0.82	0.05	277	73	−0.89	0.51	17 Jun 2003	1000	480	−0.434	410.4	518	520	44
30	0.84	0.06	666	265	−1.84	1.70	18 Aug 2003	0100	450	0.068	543.0	540	534	55
31	0.81	0.06	460	128	−2.33	0.78	24 Jul 2004	1400	560	−0.220	583.3	762	450	61
32	0.75	0.05	591	114	−0.93	0.66	14 Sep 2004	1500	550	−0.417	516.0	666	286	37
33	0.83	0.08	307	137	−0.38	0.60	30 May 2005	0100	460	−0.254	411.0	507	342	56
34	0.85	0.04	264	65	0.43	0.22	31 May 2005	0400	460	−0.141	370.6	405	342	56
35	0.73	0.06	731	154	−1.93	0.85	10 Jul 2005	1000	430	−0.166	516.8	640	332	11
36	0.85	0.07	300	127	0.09	0.51	09 Aug 2005	0000	480	−0.175	410.9	477	537	82
37	0.78	0.09	283	120	−0.48	0.58	30 Aug 2006	2000	400	−0.429	348.5	437	511	83
38	0.79	0.05	247	58	−0.01	0.20	17 Sep 2008	0400	400	0.486	425.8	366	406	107
39	0.78	0.09	256	103	0.02	0.28	04 Jun 2009	0200	310	0.276	327.7	304	327	26

Column: (1) Event number [identical with column (1) in Table 2.1]; (2) – (3) Average and standard deviation for the reference distance [R_2] (in the IPS–Earth region); (4) – (5) Average and standard deviation for the speed [V_2] (in the IPS–Earth region); (6) – (7) Average and standard deviation for the acceleration [a_2] (in the IPS–Earth region); (8) – (9) Detection date [ddmmmyyyy] and time [hhmm] of a near-Earth ICME by in situ observation at 1 AU; (10) Near-Earth ICME speed measured by in situ observation at 1 AU; (11) – (12); Index [α] and coefficient [β] for a power-law form of radial speed evolution; (13) 1 AU transit speed [$V_{\rm Tr}$] derived from the CME appearance and the ICME detection; (14) – (15) Average and standard deviation for the speed of the background wind [$V_{\rm bg}$] measured by spacecraft including ACE, *Wind*, IMP-8, and *GEOTAIL*.

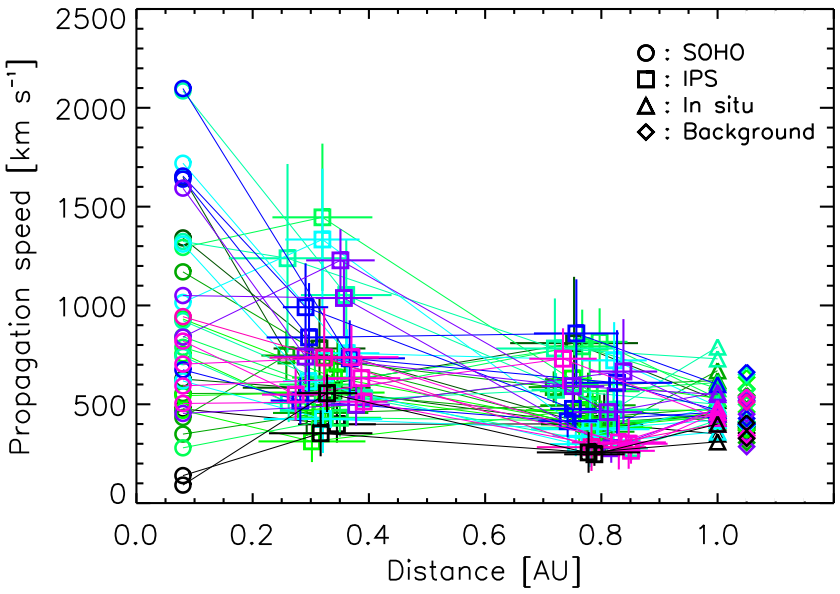

FIGURE 2.4: Radial evolution of propagation speeds for the 39 ICMEs in this study. Circles, squares, and triangles indicate speeds of ICMEs measured by SOHO/LASCO, IPS, and in situ observations, respectively. Symbols for each ICME are connected by solid lines with the same color. Diamonds indicate speeds of the background solar wind measured from in situ observations at 1 AU.

2.4.2 Fast, Moderate, and Slow ICMEs, and Their Accelerations

For the fast, moderate, and slow ICMEs, we show representative examples of speed profiles in Figures 2.5, 2.6, and 2.7, respectively. These are plotted using the values of $V_{\rm SOHO}$, R_1, V_1, R_2, V_2, $V_{\rm Earth}$, and $V_{\rm bg}$. Figure 2.5 shows a speed profile for a fast ICME observed as a halo by SOHO/LASCO on 5 November 1998, a subsequent disturbance from the IPS observations on 7 November 1998, and the event detected at 1 AU by in situ observations on 9 November 1998 (see No. 4 in Tables 2.1 and 2.2). These data show that the ICME speed rapidly decreases to the value of $V_{\rm bg}$ with an increase in radial distance; the initial speed $V_{\rm SOHO}$ value is 1342 km s^{-1}, while $V_{\rm bg}$ = 385 km s^{-1} for this ICME. This speed profile is well fit by a power-law function; the fitting-line has a value of $\alpha = -0.478$ from Equation (2.12). Figure 2.6 shows the speed profile for a moderate ICME; this ICME was observed as a normal event (neither a halo nor a partial halo) by SOHO/LASCO on 17 July 2000, on 19 July 2000 in IPS, and detected by in situ observations on 20 July 2000 (see No. 14 in Tables 2.1 and 2.2). As shown here, for this ICME, the 788 km s^{-1} initial speed gradually decreases to $V_{\rm bg}$ = 574 km s^{-1} with an increase in radial distance; we have a value of $\alpha = -0.079$. Figure 2.7 exhibits a speed profile for a slow ICME observed as a normal event by SOHO/LASCO on 29 May 2009, on 1 June 2009 by IPS observations, and detected by in situ observations on 4 June 2009 (see No. 39 in Tables 2.1 and 2.2). For this event, we confirm that

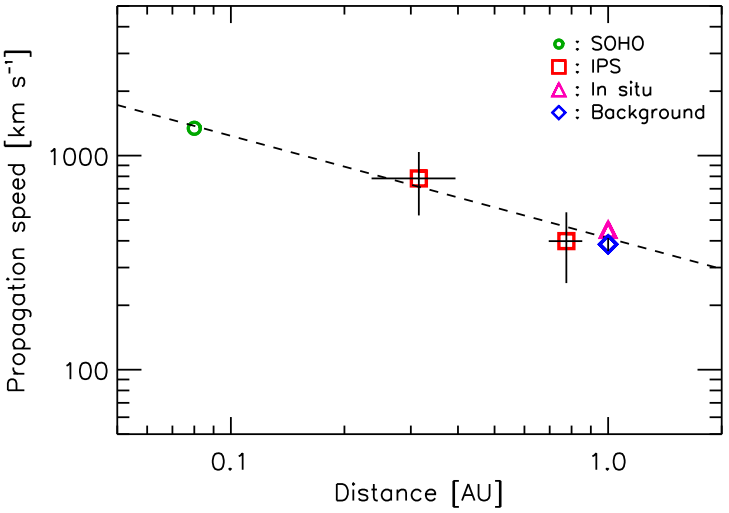

FIGURE 2.5: Speed profile for the ICME event between 5 and 9 November 1998. This is an example of a fast ICME. In this event, IPS disturbance event day is 7 November 1998. Open circle, square, and triangle denote measurements of ICME speed from SOHO/LASCO, IPS, and in situ observations, respectively. An open diamond indicates the speed of the background solar wind measured by in situ observations, and the dashed line represents the power-law fit to the data using Equation (2.12). Horizontal and vertical error bars are also plotted using σ values (standard deviation) for the reference distances (R_1 and R_2) and those for the speeds (V_1, V_2, and $V_{\rm bg}$).

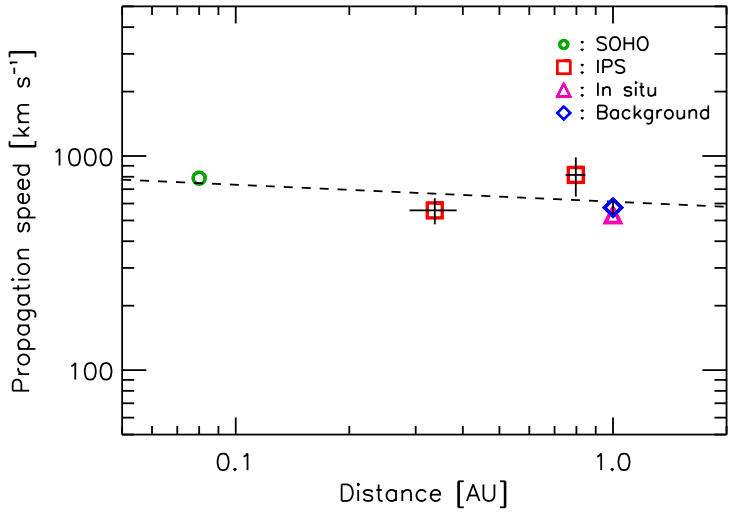

FIGURE 2.6: Speed profile for the ICME event between 17 and 20 July 2000. This is an example of a moderate ICME. In this event, IPS disturbance event day is 19 July 2000. Open circle, square, and triangle denote measurements of ICME speed from SOHO/LASCO, IPS, and in situ observations, respectively. An open diamond indicates the speed of the background solar wind measured by in situ observations, and a dashed line represents the power-law fit to the data using Equation (2.12).

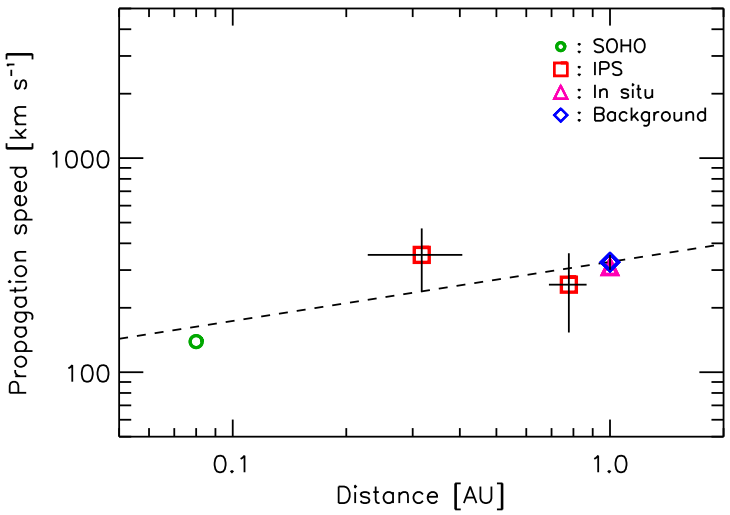

FIGURE 2.7: Speed profile for the ICME event between 29 May and 4 June 2009. This is an example of a slow ICME. In this event, IPS disturbance event day is 1 June 2009. Open circle, square, and triangle denote measurements of ICME speed from SOHO/LASCO, IPS, and in situ observations, respectively. An open diamond indicates the speed of the background solar wind measured by in situ observations, and a dashed line represents the power-law fit to the data using Equation (2.12).

$V_{\rm SOHO} = 139$ km s^{-1}, and that the propagation speed increases to $V_{\rm bg} = 327$ km s^{-1} with radial distance. This ICME shows acceleration, and the fit has a value of $\alpha = 0.276$.

Figure 2.8 shows the average radial acceleration for groups of fast, moderate, and slow ICMEs; the average acceleration in the two regions (a_1 and a_2) are calculated first using Equations (2.8) and (2.9) for each ICME, and each is subsequently averaged for respective groups. For all of them, the mean values of R_1 and R_2 with the standard errors are 0.33 ± 0.04 and 0.79 ± 0.04 AU, respectively. From this figure, we confirm that the acceleration levels vary toward zero with an increase in distance, and this trend is conspicuous for the group of fast ICMEs. We also confirm that the group of moderate ICMEs shows little acceleration.

2.4.3 Critical ICME Speed for Zero Acceleration

If ICMEs accelerate or decelerate by interaction with the solar wind, we expect that the acceleration will become zero when the propagation speed of ICMEs reaches the speed of the background solar wind. Therefore, it is important to know the ICME propagation speed in this situation in order to verify our expectations. Here, we call this speed "the critical ICME speed for zero acceleration". In Figures 2.9 and 2.10, we give information on this critical ICME speed for zero acceleration in two ways. In Figure 2.9, we show the relationship between initial ICME speeds ($V_{\rm SOHO}$) and indices (α). The α indicates

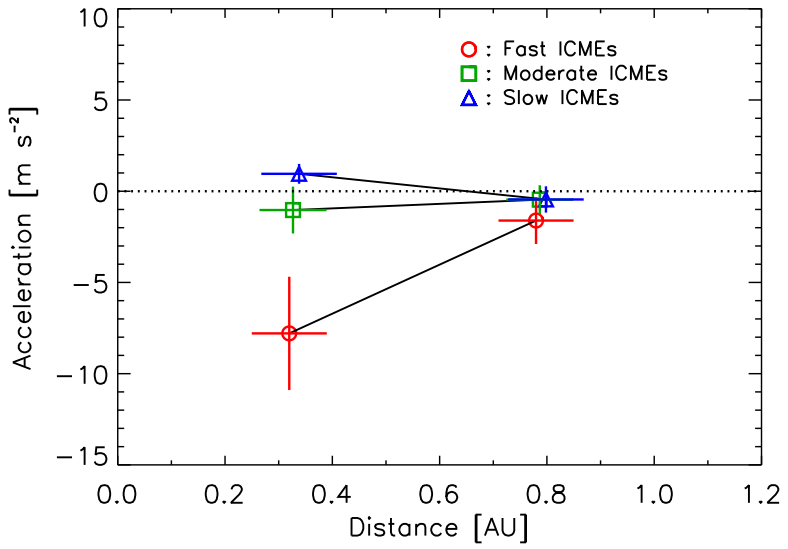

FIGURE 2.8: Average radial evolution of acceleration for the fast ($V_{\rm SOHO} - V_{\rm bg} > 500$ km s^{-1}), moderate (0 km s$^{-1} \leq V_{\rm SOHO} - V_{\rm bg} \leq 500$ km s^{-1}), and slow ($V_{\rm SOHO} - V_{\rm bg} < 0$ km s^{-1}) ICMEs in this study. Average accelerations are derived from Equations (2.8) and (2.9) with reference distances (R_1 and R_2) for each ICME. Open circle, square, and triangle symbols indicate data points that consist of (R_1, a_1) and (R_2, a_2) averaged for 14 fast, 20 moderate, and 5 slow ICMEs, respectively. Pairs of symbols are connected by solid lines.

TABLE 2.3: Mean values of coefficients (k_1, k_2, and k_3) for the best-fit quadratic curve $\alpha = k_1 + k_2 V_{\rm SOHO} + k_3 V_{\rm SOHO}^2$ and the critical ICME speed for zero acceleration [$V_{\rm c1}$], and their standard deviations, which were derived from the relationship between $V_{\rm SOHO}$ and α.

	k_1	k_2	k_3	$V_{\rm c1}$ [km s^{-1}]
Mean	4.31×10^{-1}	-1.06×10^{-3}	3.04×10^{-7}	471
Standard deviation	5.58×10^{-2}	1.16×10^{-4}	5.22×10^{-8}	19

the type of ICME motion, i.e. acceleration ($\alpha > 0$), uniform ($\alpha = 0$), and deceleration ($\alpha < 0$). As shown here, α ranges from 0.486 to -0.596 with an increase in $V_{\rm SOHO}$. Table 2.3 gives the mean values of the critical ICME speed for zero acceleration ($V_{\rm c1}$), coefficients (k_1, k_2, and k_3) for the best-fit curve, and their standard errors. Figure 2.10 shows the relationship between ICME speeds ($V_{\rm SOHO}$ and $V_{\rm IPS}$) and accelerations (a_1 and a_2). Table 2.4 presents the mean values of the critical ICME speed for zero acceleration ($V_{\rm c2}$) slope, and intercept for the best-fit line and their standard deviations, which are estimated using the FITEXY.pro from the IDL Astronomy User's Library (idlastro.gsfc.nasa.gov/homepage.html). From the above examinations, we find $V_{\rm c1} = 471 \pm 19$ km s^{-1} and $V_{\rm c2} = 480 \pm 21$ km s^{-1} as the critical ICME speed for zero acceleration.

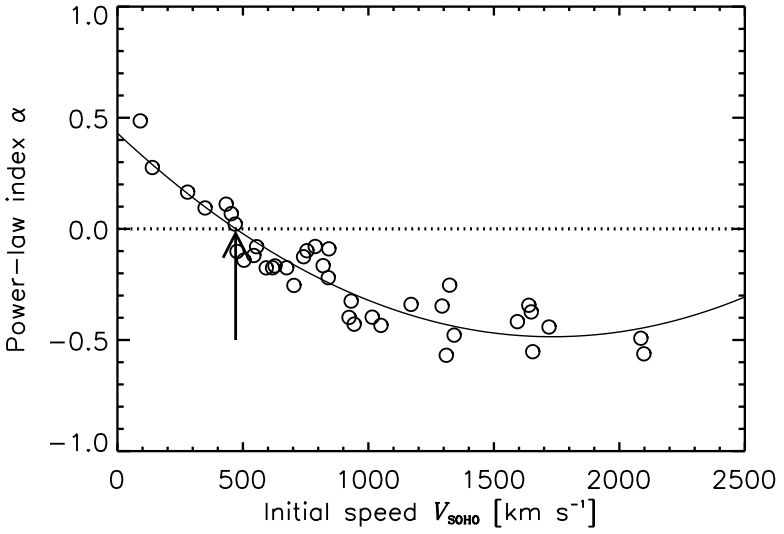

FIGURE 2.9: Relationship between estimated initial speeds ($V_{\rm SOHO}$) and indices (α) for Equation (2.12) for the 39 ICMEs in this study. Solid and dotted lines show the best-fit quadratic curve $\alpha = k_1 + k_2 V_{\rm SOHO} + k_3 V_{\rm SOHO}^2$ and the $\alpha = 0$ line. The intersection point of these lines is indicated by an arrow, and corresponds to the critical speed for zero acceleration ($V_{\rm c1}$), which is 471 ± 19 km s^{-1}.

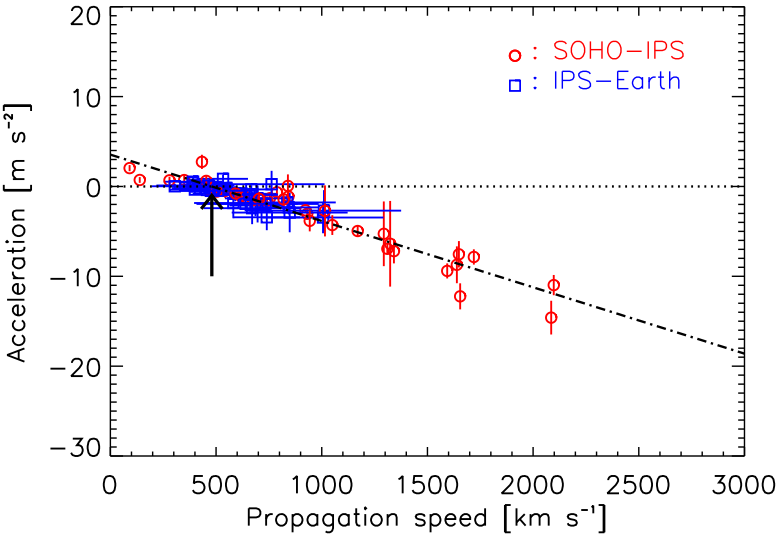

FIGURE 2.10: Relationship between propagation speeds and accelerations for the 39 ICMEs in this study. Accelerations are derived from Equations (2.8) and (2.9), while values of $V_{\rm SOHO}$ and $V_{\rm IPS}$ are used for the propagation speeds. Open circle and square symbols denote data points, which are ($V_{\rm SOHO}$, a_1) for the SOHO–IPS region and ($V_{\rm IPS}$, a_2) for the IPS–Earth region, respectively. Dash–dotted and dotted lines show the best-fit line and zero acceleration line, respectively. The arrow indicates the critical speed for zero acceleration ($V_{\rm c2}$), which is 480 ± 21 km s^{-1}.

TABLE 2.4: Mean values of slope and intercept for the best-fit line and the critical ICME speed for zero acceleration (V_{c2}) and their standard deviations, which were derived from the relationship between speeds and accelerations of ICMEs.

	Slope [s^{-1}]	Intercept [m s^{-2}]	V_{c2} [km s^{-1}]
Mean	-7.38×10^{-6}	3.54	480
Standard deviation	2.03×10^{-7}	1.24×10^{-1}	21

TABLE 2.5: Coefficients (γ_1 and γ_2), correlation coefficient (CC), and reduced χ^2 for the linear and quadratic equations.

Equation	Mean	Standard deviation	CC	χ^2
γ_1 [s^{-1}]				
Linear	6.58×10^{-6}	2.34×10^{-7}	-0.93	1.26
γ_2 [m^{-1}]				
Quadratic	6.10×10^{-12}	2.25×10^{-13}	-0.90	2.90

2.4.4 Relationship Between Acceleration and Difference in Speed

We investigated how the ICME acceleration relates to the difference in speed between it and the background solar wind. In this investigation, we attempted to show which is more suitable to describe the relationship between acceleration and difference in speed: Equations (2.1) or (2.2). Although it was assumed that the coefficients (γ_1 and γ_2) decrease with the heliocentric distance in the earlier study, for this analysis we assume that the values of coefficients are constants because we want as few variables as possible to describe the relationship. We also assume that the speed of the background solar wind is constant for heliocentric distances ranging from ≈ 0.1 to 1 AU. This assumption has been verified approximately between 0.3 and 1 AU by Neugebauer (1975) and Schwenn et al. (1981) (see Subsection 1.1.4). In Figure 2.11, the top panel shows the relationship between a and $(V - V_{\rm bg})$, and the bottom panel that between a and $(V - V_{\rm bg})|V - V_{\rm bg}|$ for ICMEs with $(V_{\rm SOHO} - V_{\rm bg}) \geq 0$ km s^{-1}, i.e. the fast and moderate ICMEs. Table 2.5 exhibits the values of γ_1 and γ_2, correlation coefficients, and reduced χ^2 derived from this analysis. It is noted that the γ_1, γ_2, and χ^2 are calculated using the FITEXY.pro. Although we also examined the slow ICMEs in the same way, we did not obtain a conclusive result. We discuss interpretations of these results in the next section.

2.5 Discussion

From Figures 2.5, 2.6, and 2.7, we confirm that fast and moderate ICMEs are rapidly and gradually decelerating during their outward propagation, respectively, while slow ICMEs are accelerating, and consequently all attain speeds close to those of the background solar

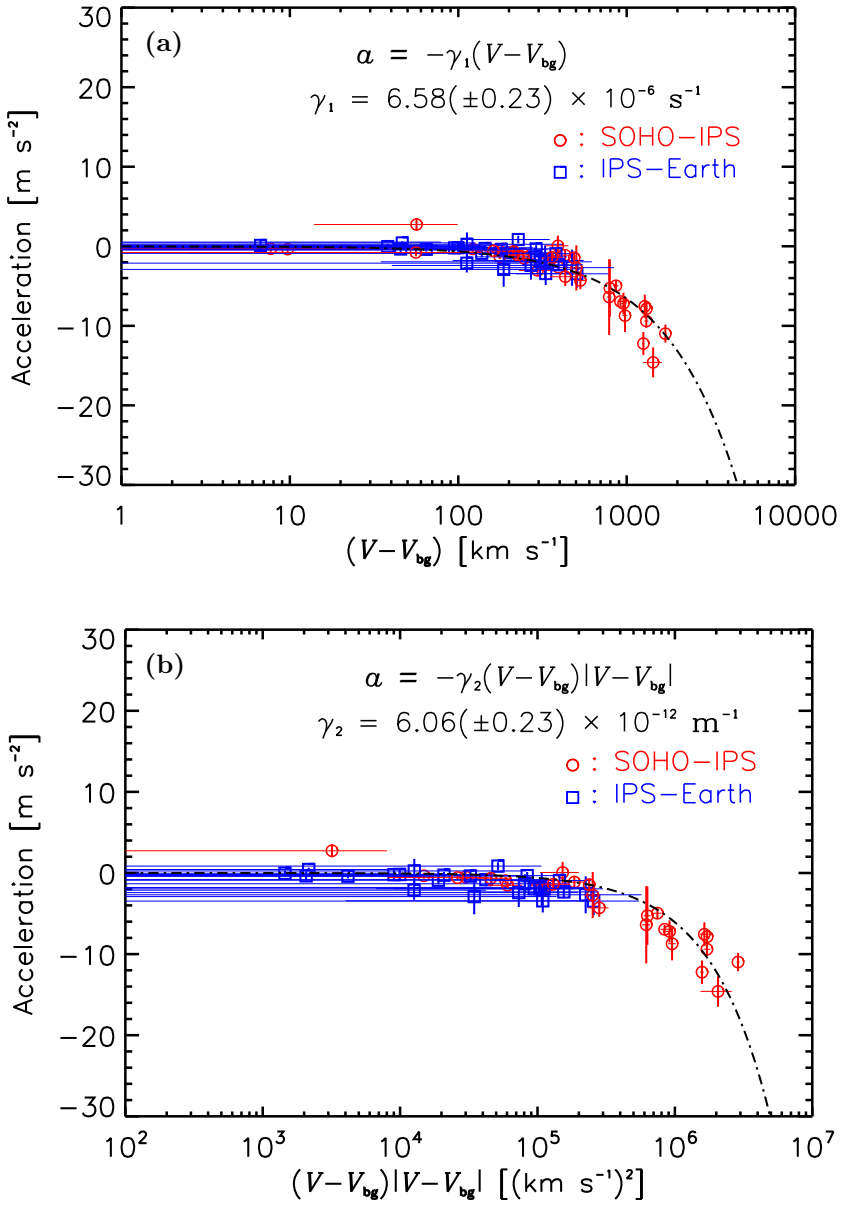

FIGURE 2.11: Relationships between (a) acceleration (a) and speed difference ($V - V_{\rm bg}$), and (b) between a and $(V - V_{\rm bg})|V - V_{\rm bg}|$, for 34 of the fast and moderate ICMEs (*i.e.* $V_{\rm SOHO} - V_{\rm bg} \geq 0$ km s^{-1}) in this study. Open circle and square symbols denote data points that consist of values of $(V_{\rm SOHO} - V_{\rm bg})$ and a_1 [or $(V_{\rm SOHO} - V_{\rm bg})|V_{\rm SOHO} - V_{\rm bg}|$ and a_1] for the SOHO–IPS region and those in which consist of values of $(V_{\rm IPS} - V_{\rm bg})$ and a_2 [or $(V_{\rm IPS} - V_{\rm bg})|V_{\rm IPS} - V_{\rm bg}|$ and a_2] for the IPS–Earth region, respectively. In each panel, the dash–dotted curve denotes the best-fit line shown as a curve because of the logarithmic x-axis scale.

wind. As shown in Figure 2.4, the distribution of ICME propagation speeds in the near-Sun region is wider than in the near-Earth region for all of the ICMEs identified in this study. This is consistent with the earlier study by Lindsay et al. (1999). We also confirm that the distribution of ICME propagation speed in the near-Earth region is similar to that of the background solar wind speed at 1 AU. We interpret these results as indicating that ICMEs accelerate or decelerate by interaction with the solar wind; the magnitude of the propelling or retarding force acting upon ICMEs depends on the difference between ICMEs and the solar wind. Thus, ICMEs attain final speeds close to the solar wind speed as they move outward from the Sun. Figure 2.4 also shows the radial evolution of ICME propagation speeds between 0.08 and 1 AU. We show that ICME speeds reach their final value at 0.79 ± 0.04 AU or at a solar distance slightly less than 1 AU. In addition, we confirm from Figure 2.8 that the acceleration at 0.79 ± 0.04 AU is much lower than at 0.33 ± 0.04 AU; this is the clearest for the group of fast ICMEs. From this, we thus conclude that most of the ICME acceleration or deceleration ends by 0.79 ± 0.04 AU. This is consistent with an earlier result obtained by Gopalswamy et al. (2001).

We expect that the critical speed of zero acceleration will be close to that of the background solar wind speed on the basis of the above. We derive two different critical speeds of $V_{c1} = 471 \pm 19$ km s^{-1} and of $V_{c2} = 480 \pm 21$ km s^{-1} from the observational data. Although there is agreement between them, both are somewhat higher than the ≈ 380 km s^{-1} reported to be the threshold speed by Manoharan (2006) and the 405 km s^{-1} reported by Gopalswamy et al. (2000). We suggest that this discrepancy is caused by the difference in our analysis methods and also the time interval chosen for the analysis. Because the properties of the background solar wind (e.g. speed and density) vary with the change in solar activity, we consider this discrepancy to be minor, and we note that both critical speeds in our result are within the typical speed of the solar wind: $V_{bg} = 445 \pm 95$ km s^{-1} from our sample. Here, we adopt the speed of 480 km s^{-1} as the critical speed for zero acceleration as a mean that is derived from the relationship between propagation speeds and accelerations without the assumption of a power-law form for the motion of the ICME.

Vlasov (1988; 1992) and Manoharan (2006) point out that the radial evolution of ICME speeds can be represented by a power-law function. A power-law speed evolution also applies to the ICMEs identified in this study as shown in Figures 2.5, 2.6, and 2.7. As indicated by Figure 2.9, the value of α varies from 0.499 (acceleration) to -0.596 (strongly deceleration) as ICME speeds increase. This result is consistent with that exhibited in Figure 2.10.

The relationship between acceleration and speed-difference for ICMEs is usually expressed by either of Equations (2.1) or (2.2). As shown in Figure 2.11, these equations are evaluated using the acceleration and speed-difference data derived from our observations. From this and Table 2.5, we find that the reduced χ^2 for the former relationship is smaller than for the latter. The assessment of the significance level shows that $\chi^2 = 1.26$ for the linear equation is smaller than the reduced χ^2 corresponding to the probability of 0.05 with 66 degrees of freedom, while $\chi^2 = 2.90$ for the quadratic one is larger. We therefore conclude that the linear equation is more suitable than the quadratic one to describe the kinematics of ICMEs with $(V_{\rm SOHO} - V_{\rm bg}) \geq 0$ km s^{-1}. From the viewpoint of fluid dynamics, a linear equation suggests that the hydrodynamic Stokes drag force (Collinson and Roper, 1995) is operating, while the quadratic equation suggests the aerodynamic drag force. Maloney and Gallagher (2010) found that the acceleration of a fast ICME showed a linear dependence on the speed difference, while that of a slow ICME showed a quadratic dependence. Our conclusion is consistent with their finding only for the fast and moderate ICMEs. We could not verify their result for the slow ICMEs because we lack sufficient observational data for the slow ICMEs in our sample. We expect to make a more detailed examination for the motion of slow ICMEs in a future study.

We also obtained the mean value of 6.58×10^{-6} s^{-1} for the coefficient γ_1 in our analysis. Substituting our value of γ_1 in our linear equation, we obtain the following simple expression:

$$a = -6.58 \times 10^{-6}(V - V_{\rm bg}), \tag{2.14}$$

as a useful way to determine the dynamics of fast and moderate ICMEs.

Last, we discuss why the linear equation with a constant γ_1 can explain the observational result. Our IPS radio-telescope system observes fluctuations of radio signals. These fluctuations are proportional to the solar wind (electron) density. Therefore, low-density ICMEs may not be detected by our system. Moreover, we used a threshold g-value more severe than that used by Manoharan (2006) and Gapper et al. (1982) for identification of ICMEs. Hence, it is conceivable that almost all detected ICMEs are high-density events in this study. In addition, from a theoretical study, Cargill (2004) indicated that with dense ICMEs, the factor γ and $C_{\rm D}$ (the dimensionless drag coefficient) become approximately constant for aerodynamic drag deceleration; here, $\gamma C_{\rm D} = \gamma_2$ in our notation. From this, we surmise that a constant value of $\gamma C_{\rm D}$ indicates that both interplanetary-space conditions and the properties of dense ICMEs are unchanged in the range from the Sun to the Earth. Therefore, γ_1 must also become approximately constant over the same range from the Sun to the Earth. Thus, to recapitulate, the

events detected using our IPS radio telescope system give results for dense ICMEs, and the dynamics of these are well explained by a linear equation with γ_1 = constant.

Chapter 3

Kinematics of Slow ICMEs and a Modified Drag Equation

3.1 Introduction

The Sun sometimes expels a large mass of plasma with magnetic fields into the interplanetary space with a wide range of speed, and this transient phenomenon is called CMEs. CMEs propagating far from the Sun are defined as ICMEs (Howard, 2011). Some of them reach the Earth and sometimes cause severe geomagnetic storms (Gosling et al., 1991; Brueckner et al., 1998; Cane et al., 2000). Therefore, understanding of ICME propagation is very important for space weather forecasting. It is known that the range of ICME speeds in the near-Earth region is narrower than that in the near-Sun region by space-borne coronagraphs and near-Earth in situ observations (e.g. Lindsay et al., 1999; Gopalswamy et al., 2000; Gopalswamy et al., 2001). On the basis of this fact, many investigators expect that ICMEs undergo an interaction with the ambient interplanetary medium. Although the motion of ICMEs is also affected by the Lorentz and gravity forces in the near-Sun region, it is expected that both forces become negligible at a large distance (Chen, 1996). Therefore, they take only the effect of drag force into account. Borgazzi et al. (2008; 2009) studied the dynamics of ICMEs in the solar wind using the hydrodynamic theory. They introduced two types of drag force depending on $V - V_{\rm bg}$ (a laminar drag) and $(V - V_{\rm bg})^2$ (a turbulent drag) to the equation of motion.

Drag force models have been tested by comparing with ICME observations. Reiner et al. (2003) examined the speed profile of a CME obtained by measurements of type-II radio bursts. Manoharan (2006) examined radial evolutions of 30 CMEs observed by SOHO/LASCO, ACE, and ORT between 1998 and 2004. Maloney and Gallagher (2010) derived three-dimensional kinematics of three ICMEs detected between 2008 and

2009 using the *Sun Earth Connection Coronal and Heliospheric Investigation* (SECCHI) instruments onboard STEREO-A and -B spacecraft. Temmer et al. (2011) also studied the influence of the solar wind on the propagation of three ICMEs using the same spacecraft. Lara et al. (2011) investigated the velocity profile of an ICME from the Sun to 5.3 AU using data from SOHO/LASCO, ACE, and *Ulysses*, and then estimated the drag coefficient and the kinematic viscosity for the ICME–solar wind interaction on the basis of fluid dynamics.

We assume that the radial motion of ICMEs is governed by the drag force(s) due to interaction with the background solar wind, and that the magnitude of the force is proportional to the difference in speed between the ICME and the solar wind. Our assumption should be tested using data obtained by interplanetary observations. We take advantage of IPS (Hewish et al., 1964) observations to determine the speeds and accelerations of ICMEs. Our IPS observations have been carried out since the early 1980s using the 327 MHz radio telescope system of STEL, Nagoya University (Kojima and Kakinuma, 1990). These observations allow us to probe into the inner heliosphere with a cadence of 24 h, and therefore are suitable for collecting global data on ICMEs.

In the previous chapter, we detected 39 ICMEs using the IPS observations by the Kiso IPS Telescope (KIT: Asai et al., 1995) during 1997 – 2009. Using the values of the initial speed ($V_{\rm SOHO}$) and $V_{\rm bg}$, we classified them into three types: fast ($V_{\rm SOHO} - V_{\rm bg} > 500$ km s^{-1}), moderate (0 km s^{-1} $\leq V_{\rm SOHO} - V_{\rm bg} \leq 500$ km s^{-1}), and slow ($V_{\rm SOHO} - V_{\rm bg} < 0$ km s^{-1}), and then examined their kinematic properties. From this examination, we found that fast and moderate ICMEs decelerate, while slow ones accelerate, and their radial speeds converge toward the speed of the solar wind as the distance increases. We also found that Equation (2.1) is more appropriate than Equation (2.2) to describe the kinematics of ICMEs that move faster than the solar wind.

In this chapter, we add new ICMEs identified between 2010 and 2011 to our list, and then examine their kinematics again on the assumption that ICMEs are controlled by the drag force(s) alone. Earlier observational studies focused mainly on the propagation of fast ICMEs, although the propagation of slow ICMEs was also studied (e.g. Shanmugaraju et al., 2009; Byrne et al., 2010; Maloney and Gallagher, 2010; Lynch et al., 2010; Temmer et al., 2011; Shen et al., 2011; Rollett et al., 2012; Vršnak et al., 2013). These earlier studies mainly presented case studies of slow ICMEs. However, understanding the general properties of their propagation requires a statistical study. Hence, in this article we focus on the kinematics of slow ICMEs, and determine their general properties by statistical analysis. We also examine fast and moderate ICMEs in more detail. Although we showed a simple equation for their motion in the previous chapter, we provide a modified one and its physical implications.

The outline of this chapter is as follows: Section 3.2 describes IPS observations, methods for event identification, and estimates of ICME speeds and accelerations. Section 3.3 provides the speed profiles of ICMEs and the analyses of the propagation properties. Section 3.4 discusses the propagation of slow ICMEs, a modified drag equation for fast and moderate ICMEs, and the estimated viscosity for the ICME–solar wind interaction.

3.2 Data and Analysis Method

The solar wind disturbance factor, the so-called "g-value" (Gapper et al., 1982), is derived from IPS observations, and represents the relative level of density fluctuation integrated along the LOS from an observed radio source to a telescope. When dense plasma passes across the LOS, the g-value becomes higher than unity while it is about unity for the quiet solar wind. In the current study, we use g-value data obtained between 2010 and 2011. The measurement of g-value has been carried out using the Solar Wind Imaging Facility (SWIFT: Tokumaru et al., 2011) since 2010 (see Subsection 1.5.2). SWIFT is capable of observing more sources than observed using KIT in a day. Therefore, we should use a different threshold of the number of observed sources for each telescope in order to keep the constant identification of disturbances. Averages and standard deviations for the number of observed sources in a day are $a_\mathrm{s} = 42$ and $\sigma_\mathrm{s} = 9$ for SWIFT. Here, we define "an observation day" as a day in which we observe $a_\mathrm{s} - 2\sigma_\mathrm{s}$ or more sources, and then decide to use 24 as this threshold for SWIFT. In addition, we also decide to use eight as a threshold of the number of $g \geq 1.5$ sources. From an examination of IPS data with these criteria, we found 260 disturbance days between 2010 and 2011, and made a list of them.

These disturbance days should be compared with CME/ICME pairs identified using SOHO/LASCO and in situ observations. Because there was no list of CME/ICME pairs between 2010 and 2011, we identified them ourselves using the SOHO/LASCO CME catalog (Yashiro et al., 2004; Gopalswamy et al., 2009; available at `cdaw.gsfc.nasa.gov/CME_list/`), 1 and 2 h averaged data of solar wind charge states obtained by SWICS (Gloeckler et al., 1998) onboard ACE (available at `www.srl.caltech.edu/ACE/ASC/`), and the criteria of ICME identification introduced by Richardson and Cane (2010). According to the these authors, the mean Fe charge $\langle \mathrm{Q_{Fe}} \rangle$ and the O VIII / O VII ratio are enhanced during the passage of an ICME. Hence, we define the detection of a near-Earth ICME as the enhancement in the charge state observed by ACE/SWICS within five days after the appearance of a major Earth-side CME in the SOHO/LASCO-C2 FOV. The start and end times of an ICME event correspond to those of the charge-state enhancement. Using this method, we made a list of CME/ICMEs found between 2010 and 2011.

We compared the list of disturbance days with that of CME/ICMEs by assuming that an ICME causes a disturbance day. We then identified seven ICMEs that were detected by SOHO/LASCO, IPS, and in situ observations between 2010 and 2011. For these, we calculated the average reference distances (R_1 and R_2), the average radial speeds (V_1 and V_2), and accelerations (a_1 and a_2). We also estimated the transit speed ($V_{\rm Tr}$) using the appearance time in the SOHO/LASCO-C2 FOV ($T_{\rm SOHO}$) and the detection time at 1 AU ($T_{\rm Earth}$). The initial speed of the associated CMEs ($V_{\rm SOHO}$) was estimated from their speed measured in the plane of the sky by SOHO/LASCO ($V_{\rm POS}$). The radial speed of near-Earth ICMEs ($V_{\rm Earth}$) is equivalent to the speed of plasma flow during the charge-state enhancement derived from in situ measurements. We note that $V_{\rm SOHO}$ and $V_{\rm Earth}$ represent the average values in the near-Sun and near-Earth regions. Likewise, V_1 and a_1 are averages in the SOHO–IPS region (from 0.1 to $\approx$ 0.6 AU), and V_2 and a_2 are averages in the IPS–Earth region (from $\approx$ 0.6 to 1 AU). To determine the speed of the background solar wind $V_{\rm bg}$, we used the OMNI dataset through OMNIWeb Plus (`omniweb.gsfc.nasa.gov/`). Using the value of $V_{\rm SOHO}$ and $V_{\rm bg}$, we classified seven ICMEs into fast ($V_{\rm SOHO} - V_{\rm bg} > 500$ km s^{-1}), moderate (0 km s^{-1} $\leq V_{\rm SOHO} - V_{\rm bg} \leq 500$ km s^{-1}), and slow ($V_{\rm SOHO} - V_{\rm bg} < 0$ km s^{-1}) ones. In our results, the numbers of fast, moderate, and slow ICMEs are 1, 5, and 1, respectively. Detailed methods of calculation for these properties are presented in Subsection 2.3.2.

3.3 Results

We list the properties of seven ICMEs detected by SWIFT between 2010 and 2011 in Tables 3.1 and 3.2 including R_0, $T_{\rm IPS}$, α, and β in addition to $T_{\rm SOHO}$, $V_{\rm POS}$, $V_{\rm SOHO}$, R_1, V_1, a_1, R_2, V_2, a_2, $T_{\rm Earth}$, $V_{\rm Earth}$, $V_{\rm Tr}$, and $V_{\rm bg}$. For the seven ICMEs, their g-maps are presented in Figures A.7 and A.8 in Appendix A. The catalog of 39 ICMEs detected by KIT during 1997 – 2009 was given in the previous chapter. We also provide a list of slow ICMEs in Tables 3.3 and 3.4. In total, we examined 46 ICMEs, which consist of 15 fast, 25 moderate, and 6 slow ones, identified during 1997 – 2011. In this investigation, we assumed that $V_{\rm bg}$ is constant for heliocentric distances ranging from $\approx$ 0.1 to 1 AU. This assumption is consistent with the speed profile of the solar wind estimated using coronagraph observations (Sheeley et al., 1997; Guhathakurta and Fisher, 1998). The constant speed of the solar wind has been verified between $\approx$ 0.3 and 1 AU by in situ measurements (Schwenn et al., 1981).

TABLE 3.1: Properties derived from SOHO/LASCO, IPS (SWIFT), and in situ observations for seven ICMEs during 2010 – 2011.

	SOHO/LASCO						IPS									
									Disturbance		SOHO–IPS region					
	Date	Time	V_{POS}	V_{SOHO}	CME	PA	Date	Time	R_0 [AU]		R_1 [AU]		V_1 [km s^{-1}]		a_1 [m s^{-2}]	
No.	[ddmmmyyyy]	[hhmm]	[km s^{-1}]	[km s^{-1}]	Type	[deg]	[ddmmmyyyy]	[hhmm]	aver.	σ	aver.	σ	aver.	σ	aver.	σ
1	07 Feb 2010	0354	421	505	FH	−99	11 Feb 2010	0117	0.81	0.20	0.45	0.10	359	92	−0.44	0.56
2	03 Apr 2010	1033	668	802	FH	−99	04 Apr 2010	0043	0.81	0.16	0.44	0.08	1030	236	−0.77	1.56
3	08 Apr 2010	0131	227	272	PH	76	11 Apr 2010	0240	0.67	0.22	0.37	0.11	374	122	0.90	0.84
4	24 May 2010	1406	427	512	FH	−99	26 May 2010	0251	0.63	0.19	0.35	0.09	466	135	−0.51	0.53
5	01 Aug 2010	1342	850	1020	FH	−99	03 Aug 2010	0356	0.77	0.21	0.43	0.11	563	160	−1.70	1.67
6	12 Nov 2010	0836	482	578	PH	170	15 Nov 2010	0201	0.80	0.16	0.44	0.08	501	105	−0.56	0.65
7	15 Feb 2011	0224	669	803	FH	−99	17 Feb 2011	0307	0.73	0.17	0.41	0.08	615	135	−1.49	0.87

Column: (1) Event number; (2) – (3) Appearance date [ddmmmyyyy] and time [hhmm] of an ICME–associated CME observed by SOHO/LASCO;(4) Speed in the sky plane measured by SOHO/LASCO at a reference distance of 0.08 AU; (5) Radial speed estimated using $V_{SOHO} = 1.20 \times V_{POS}$; (6) Type of CME (FH, PH, and NM mean Full Halo, Partial Halo, and Normal CME, respectively); (7) Position angle measured counter-clockwise from solar north in degrees (−99 means Full Halo); (8) – (9) Observation date [ddmmmyyyy] and mean time [hhmm] of IPS disturbance event day ; (10) – (11) Average and standard deviation for the distance of observed disturbance R_0; (12) – (13) Average and standard deviation for the reference distance R_1 in the SOHO–IPS region; (14) – (15) Average and standard deviation for the speed V_1 in the SOHO–IPS region; (16) – (17) Average and standard deviation for acceleration a_1 in the SOHO–IPS region.

TABLE 3.2: Properties derived from SOHO/LASCO, IPS (SWIFT), and in situ observations for seven ICMEs, and speeds of the background solar wind during 2010 – 2011.

	IPS						*in situ*			Parameters for power-law equation			Background	
	IPS–Earth region													
	R_2 [AU]		V_2 [km s^{-1}]		a_2 [m s^{-2}]									
No.	aver.	σ	aver.	σ	aver.	σ	Date [ddmmmyyyy]	Time [hhmm]	$V_{\rm Earth}$ [km s^{-1}]	Index α	Coefficient β	wind $V_{\rm Tr}$ [km s^{-1}]	$V_{\rm bg}$ [km s^{-1}] aver.	σ
1	0.91	0.10	356	376	0.62	2.29	12 Feb 2010	0000	410	−0.113	366.1	358	339	23
2	0.90	0.07	388	300	0.01	2.40	05 Apr 2010	1600	701	−0.160	599.7	776	540	90
3	0.83	0.11	640	445	−1.10	2.89	12 Apr 2010	0000	419	0.255	514.2	439	461	74
4	0.81	0.09	359	175	−0.25	0.68	28 Apr 2010	1600	373	−0.140	370.3	424	328	22
5	0.89	0.10	786	692	−1.62	7.97	04 Aug 2010	1000	592	−0.169	620.4	608	461	35
6	0.90	0.08	395	303	1.46	1.94	16 Nov 2010	1800	557	−0.080	468.7	476	534	72
7	0.87	0.08	466	298	−0.38	1.78	18 Feb 2011	0300	506	−0.203	487.3	572	534	46

Column: (1) Event number [identical with column (1) in Table 3.1]; (2) – (3) Average and standard deviation for the reference distance R_2 in the IPS–Earth region; (4) – (5) Average and standard deviation for the speed V_2 in the IPS–Earth region; (6) – (7) Average and standard deviation for the acceleration a_2 in the IPS–Earth region; (8) – (9) Detection date [ddmmmyyyy] and time [hhmm] of a near-Earth ICME by in situ observation at 1 AU; (10) Near-Earth ICME speed measured by in situ observation at 1 AU; (11) – (12); Index α and coefficient β for a power-law form of radial speed evolution; (13) 1 AU transit speed derived from the CME appearance and the ICME detection times; (14) – (15) Average and standard deviation for the speed of the background wind $V_{\rm bg}$ measured by spacecraft.

TABLE 3.3: Properties derived from SOHO/LASCO, IPS (KIT and SWIFT), and in situ observations for six slow ICMEs during 1997 – 2011.

	SOHO/LASCO						IPS									
							Disturbance				SOHO–IPS region					
	Date	Time	V_{POS}	V_{SOHO}	CME	PA	Date	Time	R_0 [AU]		R_1 [AU]		V_1 [km s^{-1}]		a_1 [m s^{-2}]	
No.	[ddmmmyyyy]	[hhmm]	[km s^{-1}]	[km s^{-1}]	Type	[deg]	[ddmmmyyyy]	[hhmm]	aver.	σ	aver.	σ	aver.	σ	aver.	σ
1	13 Apr 1999	0330	291	349	PH	228	15 Apr 1999	0453	0.55	0.16	0.32	0.08	456	130	0.71	0.55
2	06 Aug 2000	1830	233	280	PH	105	09 Aug 2000	0503	0.62	0.14	0.35	0.07	432	95	0.68	0.40
3	14 Aug 2003	2006	378	454	FH	−99	17 Aug 2003	0409	0.68	0.12	0.38	0.06	497	106	0.62	0.63
4	12 Sep 2008	1030	91	91	NM	89	14 Sep 2008	0449	0.58	0.10	0.33	0.05	556	96	2.04	0.34
5	29 May 2009	0930	139	139	NM	258	01 Jun 2009	0148	0.56	0.18	0.32	0.09	353	116	0.72	0.32
6	08 Apr 2010	0131	227	272	PH	76	11 Apr 2010	0240	0.67	0.22	0.37	0.11	374	122	0.90	0.84

Column: (1) Event number; (2) – (3) Appearance date [ddmmmyyyy] and time [hhmm] of an ICME-associated CME observed by SOHO/LASCO;(4) Speed in the sky plane measured by SOHO/LASCO at a reference distance of 0.08 AU ; (5) Radial speed estimated using $V_{SOHO} = 1.20 \times V_{POS}$; (6) Type of CME (FH, PH, and NM mean Full Halo, Partial Halo, and Normal CME, respectively); (7) Position angle measured counter-clockwise from solar north in degrees (−99 means Full Halo); (8) – (9) Observation date [ddmmmyyyy] and mean time [hhmm] of IPS disturbance event day ; (10) – (11) Average and standard deviation for the distance of observed disturbance R_0; (12) – (13) Average and standard deviation for the reference distance R_1 in the SOHO–IPS region; (14) – (15) Average and standard deviation for the speed V_1 in the SOHO–IPS region; (16) – (17) Average and standard deviation for acceleration a_1 in the SOHO–IPS region.

TABLE 3.4: Properties derived from SOHO/LASCO, IPS (KIT and SWIFT), and in situ observations for six slow ICMEs, and speeds of background solar wind during 1997–2011.

	IPS						*in situ*			Parameters for power-law equation			Background	
	IPS–Earth region													
	R_2 [AU]		V_2 [km s^{-1}]		a_2 [m s^{-2}]		Date	Time	$V_{\rm Earth}$	Index	Coefficient	wind $V_{\rm Tr}$	$V_{\rm bg}$ [km s^{-1}]	
No.	aver.	σ	aver.	σ	aver.	σ	[ddmmmyyyy]	[hhmm]	[km s^{-1}]	α	β	[km s^{-1}]	aver.	σ
1	0.78	0.08	495	165	−0.49	0.73	16 Apr 1999	1800	410	0.094	465.0	480	398	15
2	0.81	0.07	414	149	0.06	0.62	10 Aug 2000	1900	430	0.165	447.8	430	412	36
3	0.84	0.06	666	265	−1.84	1.70	18 Aug 2003	0100	450	0.068	543.0	540	534	55
4	0.79	0.05	247	58	−0.01	0.20	17 Sep 2008	0400	400	0.486	425.8	366	406	107
5	0.78	0.09	256	103	0.02	0.28	04 Jun 2009	0200	310	0.276	327.7	304	327	26
6	0.83	0.11	640	445	−1.10	2.89	12 Apr 2010	0000	419	0.255	514.2	439	461	74

Column: (1) Event number [identical with column (1) in Table 3.3]; (2) – (3) Average and standard deviation for the reference distance R_2 in the IPS–Earth region; (4) – (5) Average and standard deviation for the speed V_2 in the IPS–Earth region; (6) – (7) Average and standard deviation for the acceleration a_2 in the IPS–Earth region; (8) – (9) Detection date [ddmmmyyyy] and time [hhmm] of a near-Earth ICME by in situ observation at 1 AU; (10) Near-Earth ICME speed measured by in situ observation at 1 AU; (11) – (12); Index α and coefficient β for a power-law form of radial speed evolution; (13) 1 AU transit speed derived from the CME appearance and the ICME detection times; (14) – (15) Average and standard deviation for the speed of the background wind $V_{\rm bg}$ measured by spacecraft.

TABLE 3.5: Mean values of coefficients k_1 and k_2 for the best-fit line $\alpha = k_1 + k_2 V_{\rm SOHO}$, the speed at the zero-acceleration point ($V_{\rm c}$), and their standard deviations.

	k_1	k_2	$V_{\rm c}$ [km s^{-1}]
Mean	5.00×10^{-1}	-1.04×10^{-3}	479
Standard deviation	6.82×10^{-2}	2.34×10^{-4}	126

In the following figures, an error bar represents one standard deviation (1σ) of the mean for each parameter. Figure 3.1 shows speed profiles for six slow ICMEs identified in this study. As shown here, the ICME speeds increase with the radial distance, and those at 1 AU are close to the speed of the solar wind for all of them. From this, we claim that their speed profiles are well fit by a power-law function within the error bars, excluding the 12 September 2008 event (see No.4 in Tables 3.3 and 3.4). The 12 September 2008 event has the largest difference in speed ($V_{\rm SOHO} - V_{\rm bg} = -314$ km s^{-1}) in our sample, while the others have $V_{\rm SOHO} - V_{\rm bg} > -200$ km s^{-1}.

Figure 3.2 exhibits the relationship between the initial speed $V_{\rm SOHO}$ and the index α for slow ICMEs. As shown here, α decreases from 0.486 to 0.068 as $V_{\rm SOHO}$ increases. The intersection point between the best-fit line $\alpha = k_1 + k_2 V_{\rm SOHO}$ and the $\alpha = 0$ line is designated as $V_{\rm c}$ in the following. Manoharan (2006) studied the same relationship for 30 CMEs. Four of them are slow CMEs, which have a slower initial speed than the final. To compare them with our result, they are also plotted in Figure 3.2. We find that their values of α range from 0.58 to -0.06. The mean values of $V_{\rm c}$ and coefficients k_1 and k_2 for the best-fit line, and their standard deviations (1σ) are given in Table 3.5. From this examination, we find $V_{\rm c} = 479 \pm 126$ km s^{-1} as the threshold speed when α becomes zero, i.e. the slow ICMEs have zero acceleration.

In Figure 3.3, we plot all of their speed profiles to compare radial-speed evolutions of slow ICMEs. Here, data points for each ICME are connected by solid lines instead of fitting by Equation (2.12). We note that differences in speed ($V - V_{\rm bg}$) are used instead of ICME speeds in the y-axis, which correspond to $V_{\rm SOHO} - V_{\rm bg}$ in the near-Sun region, $V_1 - V_{\rm bg}$ in the SOHO–IPS region, $V_2 - V_{\rm bg}$ in the IPS–Earth region, and $V_{\rm Earth} - V_{\rm bg}$ in the near-Earth region. From the top panel, we find that the speed differences range from -314 km s^{-1} to -49 km s^{-1} in the near-Sun region, while they show a narrow range from -84 km s^{-1} to 11 km s^{-1} in the near-Earth region. The bottom panel shows the averaged profile for their propagation. Table 3.6 gives the average values of the distance and of the speed difference with the standard deviation in each region for the slow ICMEs.

We attempt to show which of Equations (2.1) and (2.2) is more suitable to describe the relationship between the acceleration and the difference in speeds for slow ICMEs.

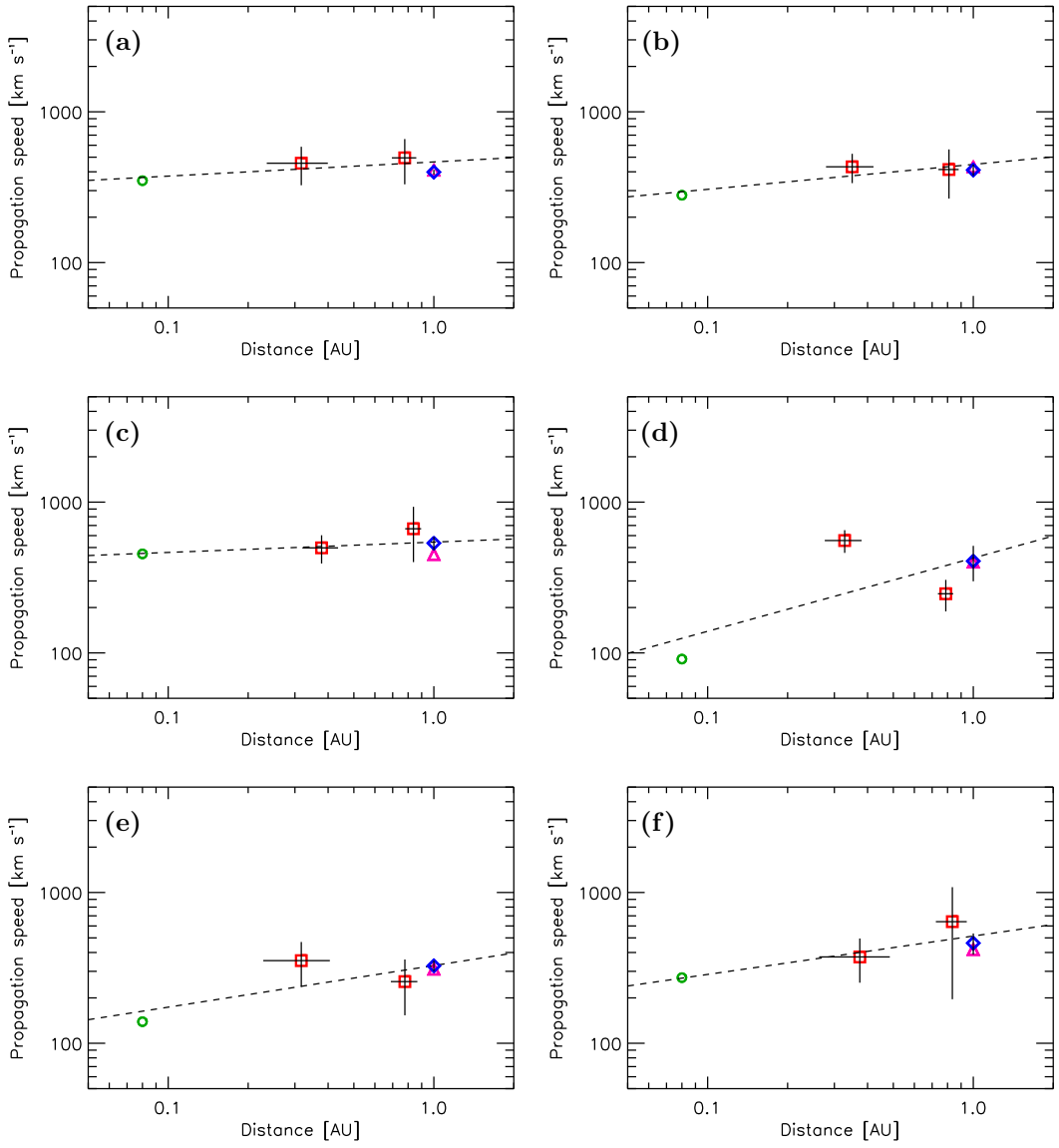

FIGURE 3.1: Speed profiles for six slow ICMEs detected between (a) 13 and 16 April 1999, (b) 6 and 10 August 2000, (c) 14 and 18 August 2003, (d) 12 and 17 September 2008, (e)29 May and 4 June 2009, and (f) 8 and 12 April 2010. In each panel, the circle (green, at 0.08 AU), squares (red, at R_1 and R_2), and triangle (purple, at 1 AU) denote measurements of ICME speeds from SOHO/LASCO, IPS, and in-situ observations, respectively. Diamonds (blue, at 1 AU) indicate the speed of the background solar wind measured by in-situ observations, and the dashed line represents the power-law fit to the data using a power-law equation for distance.

TABLE 3.6: Mean values of the distance and of the speed difference with a standard deviation in each region for the slow ICMEs.

Region	Distance [AU]	Difference in speed [km s^{-1}]
Near-Sun	0.08	-159 ± 95
SOHO–IPS	0.34 ± 0.08	22 ± 111
IPS–Earth	0.80 ± 0.08	30 ± 197
Near-Earth	1.00	-20 ± 38

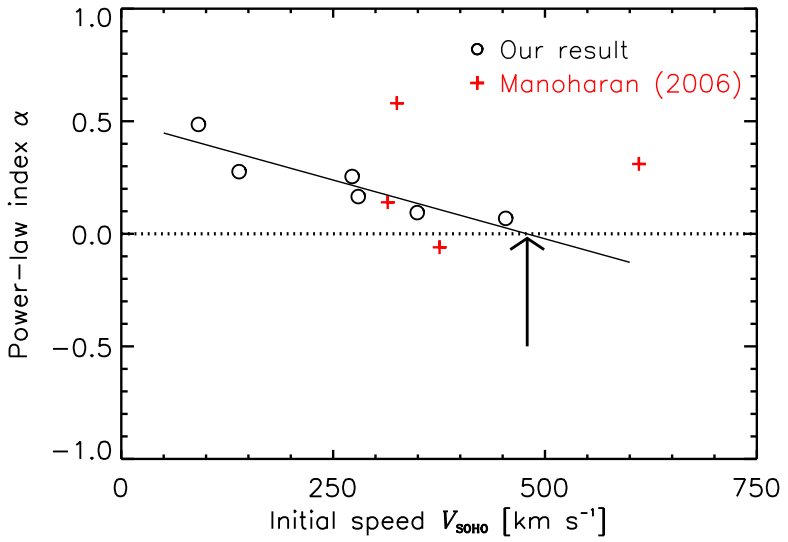

FIGURE 3.2: Relationship between the estimated initial speed $V_{\rm SOHO}$ and the index α [Equation (2.12)] for six slow ICMEs. Circles show our data points, and crosses indicate those for the four slow events studied by Manoharan (2006). The solid and dotted lines denote the best-fit line $\alpha = k_1 + k_2 V_{\rm SOHO}$ and the $\alpha = 0$ line, respectively. The arrow indicates the intersection of these two lines corresponding to the zero-acceleration point, $V_{\rm c} = 479 \pm 126$ km s^{-1}.

We assumed that γ_1 and γ_2 are constants because we need as few variables as possible to describe the relationship. In Figure 3.4, the top panel shows the relationship between a and $V - V_{\rm bg}$, while the bottom panel depicts that between a and $(V - V_{\rm bg})|V - V_{\rm bg}|$ for slow ICMEs. Data of $V_{\rm SOHO}$ and a_1 were used for the SOHO–IPS region, while those of $V_{\rm IPS}$ and a_2 were used for the IPS–Earth region. We derived the values of coefficients from the slopes of best-fit lines in this figure, and also calculated the reduced χ^2 values to assess the goodness of fit. We also take the same examination for the remaining 40 ICMEs. Table 3.7 gives values of the coefficients γ_1 and γ_2 and the reduced χ^2 values for each fitting. We find from this table that the χ^2 value of the linear equation is smaller than the quadratic one for the six slow ICMEs, and the group of fast and moderate ICMEs also has a similar result. Figure 3.5 shows the relationship between a and $V - V_{\rm bg}$ for a group of fast and moderate ICMEs. Data of $V_{\rm SOHO}$ and a_1 were used for the SOHO–IPS region, while those of $V_{\rm IPS}$ and a_2 were used for the IPS–Earth region. In this figure, we compare the acceleration-speed profiles of Equation (2.1) with $\gamma_1 = 6.51 \times 10^{-6}$ s^{-1} and Equation (2.2) with $\gamma_2 = 6.06 \times 10^{-12}$ m^{-1}. Values of γ_1 and γ_2 with standard deviations and the reduced χ^2 derived from this examination are also listed in Table 3.7.

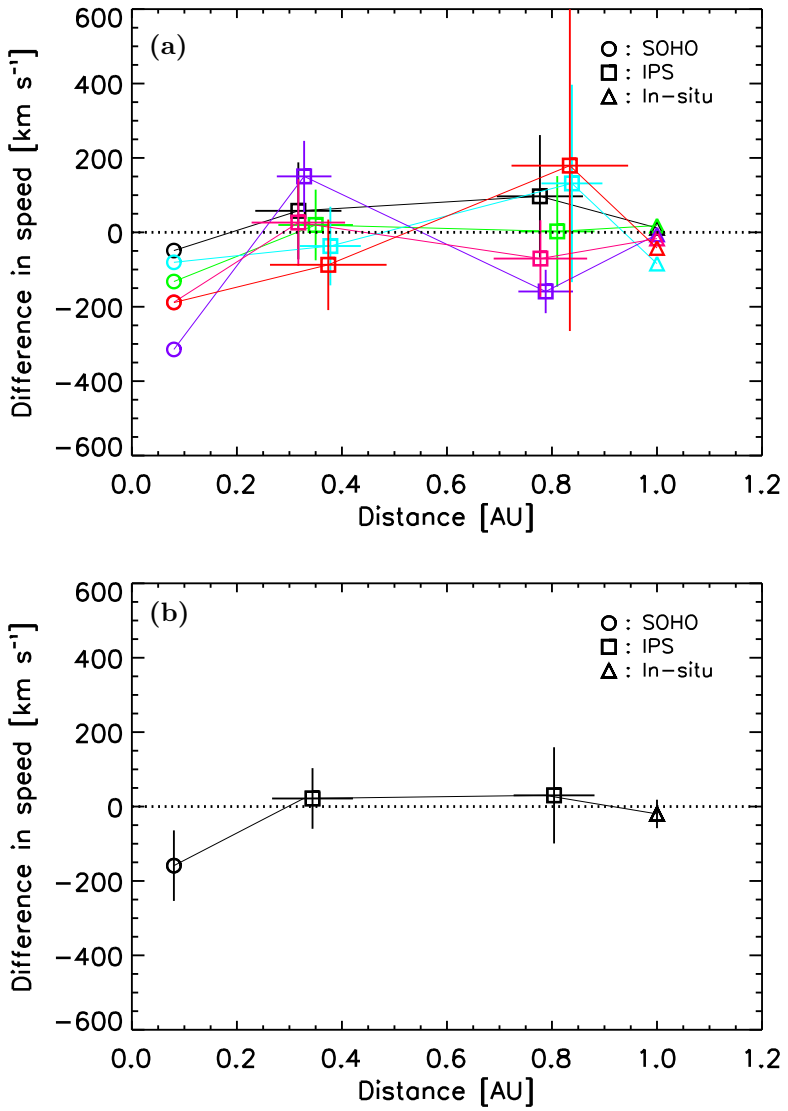

FIGURE 3.3: Radial evolution of (a) differences in speed ($V - V_{\rm bg}$) for six slow ICMEs and (b) their averaged profile. Circles, squares, and triangles indicate the values of $V - V_{\rm bg}$ for the ICMEs in near-Sun, interplanetary space, and near-Earth regions, respectively. Symbols for each ICME in panel (a) are connected by solid lines with the same color. The dotted line denotes the $V - V_{\rm bg} = 0$ line in each panel.

TABLE 3.7: Coefficients γ_1, γ_2, and reduced χ^2 values for the slow ICMEs and a group of moderate and fast ones.

Type of ICMEs and equation	Coefficient (Average and standard deviation)	χ^2
Slow ICMEs		
Linear	$\gamma_1 = 5.58(\pm1.77) \times 10^{-6}$ [s^{-1}]	0.24
Quadratic	$\gamma_2 = 2.36(\pm1.03) \times 10^{-11}$ [m^{-1}]	0.36
Fast and Moderate ICMEs		
Linear	$\gamma_1 = 6.51(\pm0.23) \times 10^{-6}$ [s^{-1}]	1.14
Quadratic	$\gamma_2 = 6.06(\pm0.23) \times 10^{-12}$ [m^{-1}]	2.50

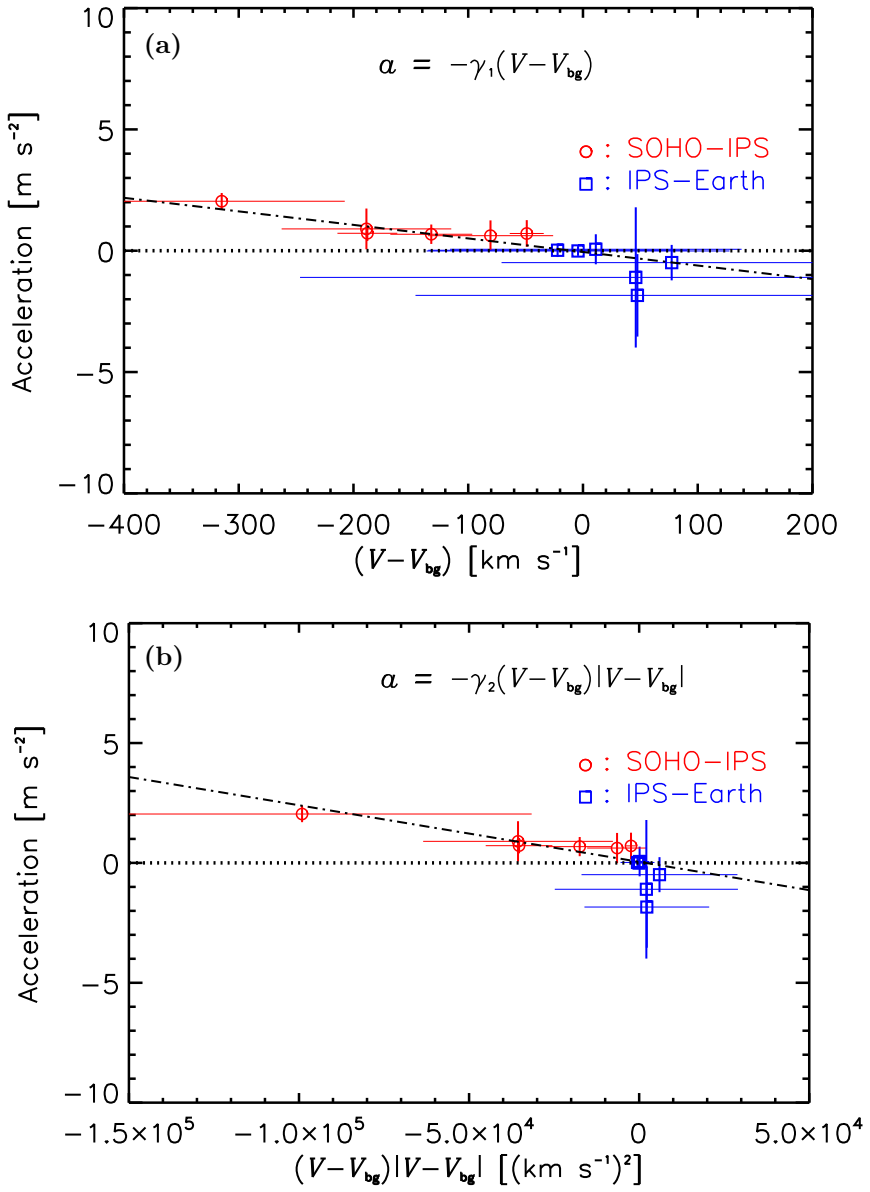

FIGURE 3.4: Relationships between (a) acceleration (a) and difference in speed ($V - V_{\rm bg}$) and (b) between a and $(V - V_{\rm bg})|V - V_{\rm bg}|$ for six slow ICMEs identified in this study. Circles (red) and squares (blue) denote data points in the SOHO–IPS and IPS–Earth regions, respectively. The dash–dotted line and the dotted line denote the best-fit line and the zero-acceleration line, respectively, in each panel.

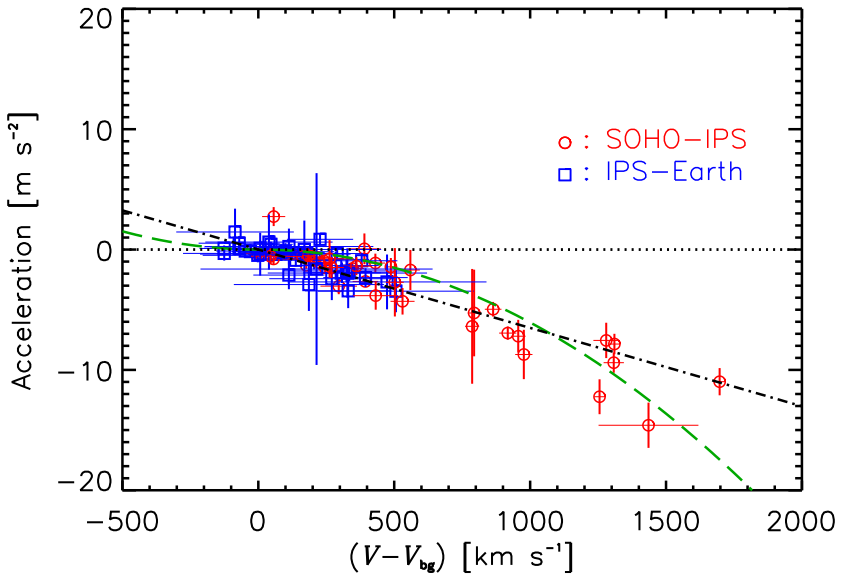

FIGURE 3.5: Relationship between acceleration a and difference in speed $(V - V_{\rm bg})$ for 40 fast and moderate ICMEs. Circles (red) and squares (blue) denote data points in the SOHO–IPS and IPS–Earth regions, respectively. The dotted line shows the zero-acceleration line. The dash–dotted (black) line and the dashed (green) line denote acceleration–speed profiles of Equation (2.1) with $\gamma_1 = 6.51 \times 10^{-6}$ s^{-1} and Equation (2.2) with $\gamma_2 = 6.06 \times 10^{-12}$ m^{-1}, respectively.

3.4 Discussion

3.4.1 Radial Evolution of Slow ICMEs

From Figure 3.1, we confirm that all of the slow ICMEs accelerate toward the speed of the background solar wind during their outward propagation. Figure 3.2 shows that the value of α decreases from 0.486 to 0.068 as the wind speed increases, up to the intersection point $V_{\rm c}$ where $\alpha = 0$. Our range of α is consistent with that reported by Manoharan (2006) for slow CMEs. As presented in Table 3.5, we derive the coefficients for the best-fit line and the value of $V_{\rm c}$ from the observational data. We find that our result ($\alpha = 0.50 - 0.0010 V_{\rm SOHO}$) is similar to $\alpha = 0.69 - 0.0012V$ reported by Shanmugaraju et al. (2009) for the best-fit line. We note that their result was obtained from SOHO/LASCO observations with a FOV of < 32 solar radii, while we studied the radial evolution of ICMEs in a wider region from the Sun to Earth. The similarity between these best-fit lines implies that slow ICMEs quickly adjust themselves to the speed of the solar wind. We also obtain $V_{\rm c} = 479 \pm 126$ km s^{-1} as the threshold speed where α becomes zero, which is consistent with results in the previous chapter. The mean value is somewhat lower than the threshold speed of 575 km s^{-1} derived from their best-fit equation, though the difference is within 1 σ.

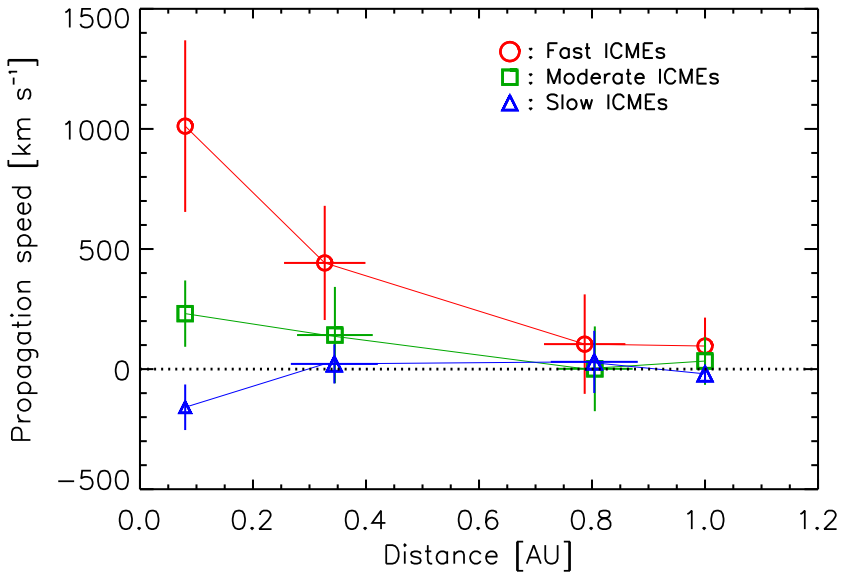

FIGURE 3.6: Radial evolutions of averaged propagation speed for the fast, moderate, and slow ICMEs in the solar wind frame of reference. Circles, squares, and triangles indicate the values of $V - V_{\rm bg}$ for the fast, moderate, and slow ICMEs, respectively. Symbols for each group of ICMEs are connected by solid lines with the same color. The dotted line denotes the $V - V_{\rm bg} = 0$ line.

Figure 3.3(a) shows that the distribution of speed differences in the near-Sun region is wider than in the near-Earth region. This and the above results justify our assumption that the motion of ICMEs is controlled by the drag force(s) due to interaction with the background solar wind. Temmer et al. (2011), Rollett et al. (2012), and Vršnak et al. (2013) reported that the acceleration of slow ICMEs attains the speed of the solar wind within 0.5 AU. Figure 3.3(b) and Table 3.6 show that the slow ICMEs attain their final speed by 0.34 ± 0.03 AU. These are consistent with the earlier studies. We emphasize that the acceleration cessation distance of ≈ 0.3 AU for slow ICMEs is different from ≈ 0.8 AU for fast ICMEs as presented by Gopalswamy et al. (2001) and the previous chapter. Figure 3.6 shows a comparison between averaged distance–speed profiles for the fast, moderate, and slow ICMEs in the solar wind frame of reference. We find from this figure that a velocity adjustment of slow ICMEs is more faster than that of the fast ones. From numerical MHD simulations, Vršnak et al. (2010) found that ICMEs having a large angular width adjust to the speed of the solar wind already close to the Sun.

We confirm that not only a group of fast and moderate ICMEs, but also slow ICMEs show that the χ^2 value for the linear equation is smaller than for the quadratic one. However, the assessment of significance levels shows that Equation (2.2) is more suitable than (2.1) to describe the relationship between a and $V - V_{\rm bg}$ for the slow ICMEs because the latter is too good to fit with data points. Maloney and Gallagher (2010) introduced an equation of motion $\mathrm{d}V/\mathrm{d}t = -\kappa R^{-\zeta}(V - V_{\rm bg})^{\xi}$ to describe the motion of ICMEs, where κ, ζ, and ξ are constants. They reported that a quadratic equation ($\xi = 2$) explained

the motion of a slow ICME, while a linear equation ($\xi = 1$) gave a better fitting than the quadratic one for the motion of a fast ICME. Byrne et al. (2010) also presented evidence that the aerodynamic drag force (Cargill, 2004) acted on a slow ICME of 12 December 2008. Our results are consistent with their studies for slow ICMEs. However, six events of slow ICMEs in our sample are not sufficient to investigate their kinematics in more detail, while we detected 40 events of fast and moderate ones during 1997 – 2011. We need to identify more slow ICMEs and then examine their propagation carefully.

3.4.2 Modified Drag Equation for Fast and Moderate ICMEs

For the group of fast and moderate ICMEs, we find values of the coefficients γ_1 and γ_2. Although the constancy of these coefficients is assumed in Equations (2.1) and (2.2), we also find a speed dependence in γ_1 and γ_2, as shown in Table 3.8. In Chapter 2, we showed a linear relationship between the acceleration and difference in speed for a group of fast and moderate ICMEs and then proposed the simple expression

$$a = -6.58 \times 10^{-6}(V - V_{\rm bg}) \tag{3.1}$$

as an equation of ICME motion on the assumption that the coefficient is constant in a speed range of $V_{\rm SOHO} - V_{\rm bg} \geq 0$ km s^{-1}. Now, we need to correct our assumption for the constancy of γ_1.

To analyze this point in detail, we calculated the mean values of γ_1 and difference in speed with 1σ for each classification of ICMEs. These values are presented in Table 3.8. In this analysis, slow ICMEs are excluded from consideration because of the conclusion presented in the previous subsection. Earlier studies (e.g. Vršnak and Gopalswamy, 2002; Maloney and Gallagher, 2010) assumed a distance dependence of γ_1 such as $\kappa R^{-\zeta}$. We also examined the difference between γ_1 in the SOHO–IPS region and in the IPS–Earth region for fast and moderate ICMEs. The mean values of γ_1 and the distance, with the standard deviation in each region, are given in Table 3.9. Figure 3.7 shows a speed dependence and distance dependence of γ_1. From comparison between the above results, we find that the speed dependence of γ_1 is more significant than its distance dependence. Therefore, we conclude that the former is a more remarkable factor than the latter in the following examination. We used the values of mean difference in speed and γ_1 for fast and moderate ICMEs, and drew a straight line through their data points on a x-y-chart in panel (a) in Figure 3.7. From the mean values of the slope and of the intercept in the y-axis, the relationship between γ_1 and mean $V - V_{\rm bg}$ can be approximated by the following equation:

$$\gamma_1 = 2.07 \times 10^{-12}(V - V_{\rm bg}) + 4.84 \times 10^{-6}. \tag{3.2}$$

TABLE 3.8: Mean values of coefficient γ_1 and the difference in speed with standard deviations for each group of ICMEs.

Type of ICMEs	$V_{\rm SOHO} - V_{\rm bg}$ [km s^{-1}]	γ_1 [$\times 10^{-6}$ s^{-1}]
Fast	1012 ± 357	6.94 ± 0.26
Moderate	231 ± 138	5.32 ± 0.40

TABLE 3.9: Mean values of coefficient γ_1 and the distance in the SOHO–IPS and IPS–Earth regions for each group of ICMEs, and their standard deviations.

	Distance	γ_1 [$\times 10^{-6}$ s^{-1}]	
Region	[AU]	Fast ICMEs	Moderate ICMEs
SOHO–IPS	0.34 ± 0.08	6.95 ± 0.27	5.36 ± 0.41
IPS–Earth	0.80 ± 0.08	6.20 ± 1.88	4.74 ± 1.66

We modified the expression for the ICME motion by taking the variability of γ_1 into account. Substituting Equation (3.2) into Equation (2.1), we obtain the following expression:

$$a = -2.07 \times 10^{-12}(V - V_{\rm bg})|V - V_{\rm bg}| - 4.84 \times 10^{-6}(V - V_{\rm bg}). \tag{3.3}$$

Speed–acceleration profiles given by Equations (3.1) and (3.3) were compared with observations in Figure 3.8. Data of $V_{\rm SOHO}$ and a_1 were used for the SOHO–IPS region, while those of $V_{\rm IPS}$ and a_2 were used for the IPS–Earth region. We confirm that the χ^2 value for Equation (3.3) is closer to unity than that for Equation (3.1), although both χ^2 values satisfy the statistical significance level of 0.05. Therefore, we conclude that Equation (3.3) is more appropriate than Equation (3.1) to describe the motion of ICMEs propagating faster than the solar wind. On the other hand, we also confirm that the speed–acceleration profile given by Equation (3.3) is very close to that of Equation (3.1) with a discrepancy of $< \pm 0.4$ m s^{-2} in a range of speed from 0 to ≈ 1000 km s^{-1}. This confirmation suggests that Equation (3.1) is a good approximation for kinematics of ICMEs with 0 km s^{-1} $\leq V - V_{\rm bg} <$ 1000 km s^{-1}.

Equations (2.1) and (3.2) are similar to a set of simultaneous equations in the "snow plough" model proposed by Tappin (2006). While he explained that ICMEs decelerate by the momentum transfer with piling-up mass in front of them, we here explain their acceleration in terms of fluid dynamics. When an object propagates in a fluid, the object suffers the drag force due to the interaction with the surrounding medium. The characteristics of drag force changes depending on the Reynolds number Re $= (\rho d U)/\mu = (dU)/\nu$, where ρ, d, U, and μ are the fluid density, the size and speed of the object, and the viscosity of the fluid, respectively, and ν is the kinematic viscosity defined as $\nu = \mu/\rho$.

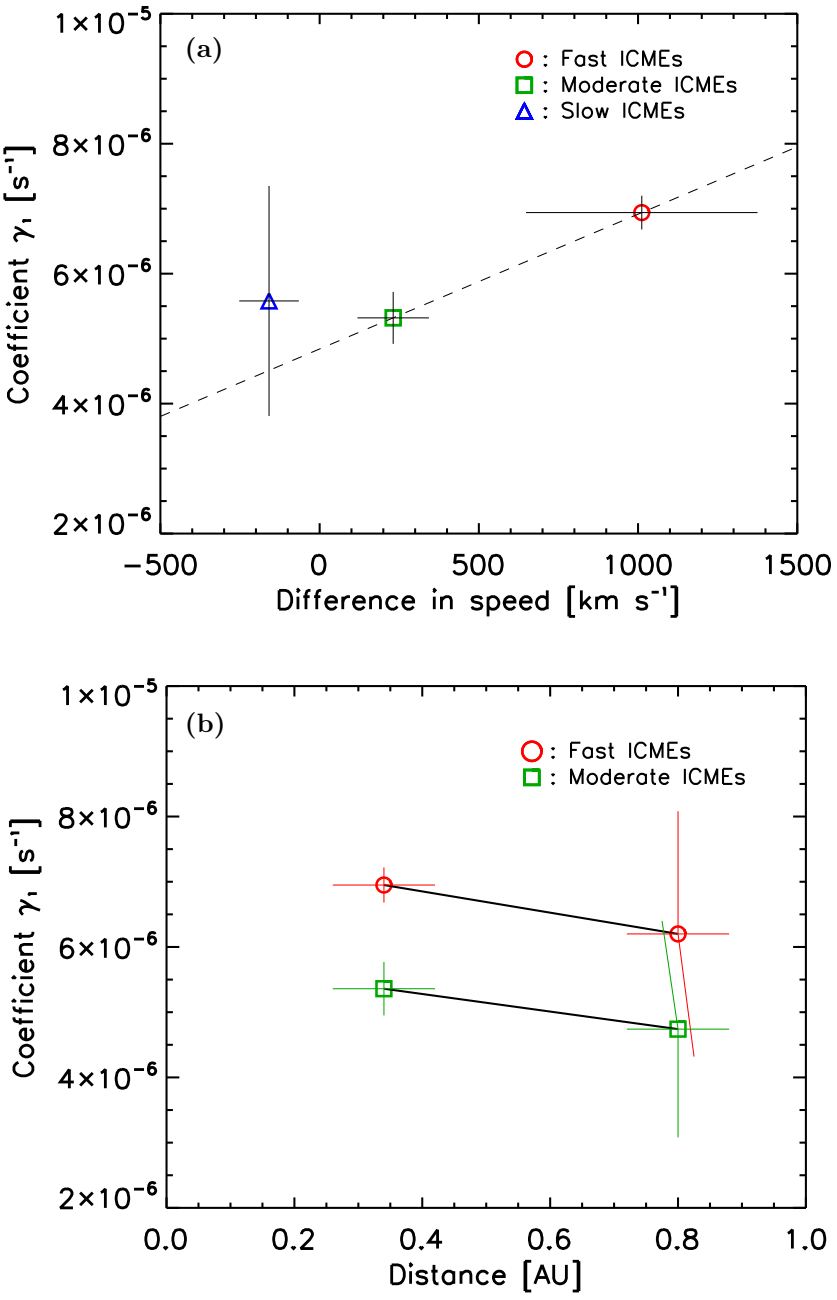

FIGURE 3.7: (a) Speed dependence and (b) distance dependence of coefficient γ_1. In each panel, circles, squares, and triangles indicate data-points for the fast, moderate, and slow ICMEs, respectively, and error bars represent 1σ of the mean for each parameter. In panel (a), the broken line denotes the straight line through data-points for the fast and moderate ICMEs. In panel (b), symbols for each group of ICMEs are connected by a solid line.

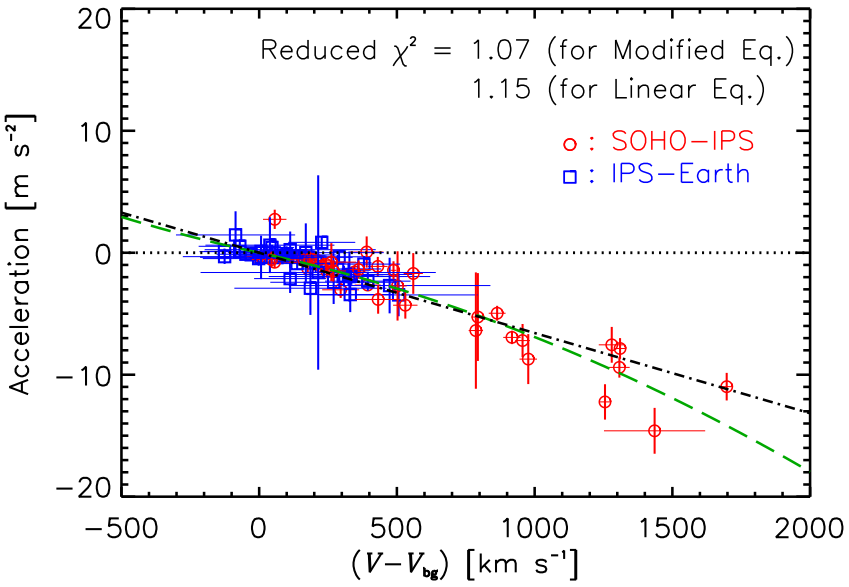

FIGURE 3.8: Comparison between drag-force models and observations for the 40 fast and moderate ICMEs. Circles (red) and squares (blue) denote data points in the SOHO–IPS and IPS–Earth regions, respectively. The dotted line shows the zero-acceleration line. The dash–dotted (black) line and the dashed (green) line denote acceleration–speed profiles of Equation (3.1) and Equation (3.3), respectively.

The drag force is proportional to U for Re $\ll 1$ and to U^2 for Re $\gg 1$. The former is called the hydrodynamic Stokes drag force (Collinson and Roper, 1995), while the latter corresponds to the aerodynamic drag force. Borgazzi et al. (2008; 2009) discussed the ICME propagation using a model involving both drag forces by assuming a spherical body of ICMEs. They assumed that ICMEs undergo both Stokes and aerodynamic drag forces during their propagation.

Here, we note that Equation (3.3) consists of quadratic and linear terms, which can be interpreted to be due to the aerodynamic and Stokes drag forces, respectively. To understand the character of this equation, we assessed the contribution from each term to the net acceleration. These contributions were calculated by applying various solar wind speeds to Equation (3.3), and are listed in Table 3.10. We confirm from this table that the contribution from each term varies with the difference in speed, and the linear term (Stokes drag force) contributes more than the quadratic term (aerodynamic drag force) to the net acceleration in a speed range of 0 km s^{-1} $\leq V - V_{\rm bg} \leq$ 2300 km s^{-1}. This result suggests that ICMEs with the above speed range are controlled mainly by the Stokes drag force, while the aerodynamic drag force is a predominant factor for the propagation of ICMEs with $V - V_{\rm bg} >$ 2300 km s^{-1}. This interpretation is consistent with the fundamental theory of fluid dynamics because Re $\propto V$. However, ICMEs with $V - V_{\rm bg} >$ 2300 km s^{-1} are extremely fast eruptions having the propagation speed exceeding 2800 km s^{-1}, and so are very rare (Gopalswamy et al., 2009). Therefore, we

TABLE 3.10: Contributions of linear and quadratic terms to the net acceleration versus the difference in speed $(V - V_{\rm bg})$ in Equation (3.3).

$(V - V_{\rm bg})$ [km s^{-1}]	Net acceleration [m s^{-2}]	Linear term contrib. [%]	Quadratic term contrib. [%]
100	−0.51	95.9	4.1
500	−2.94	82.4	17.6
1000	−6.91	70.1	29.9
1500	−11.92	60.9	39.1
2000	−17.97	53.9	46.1
2100	−19.30	52.7	47.3
2200	−20.68	51.5	48.5
2300	−22.09	50.4	49.6
2400	−23.55	49.4	50.6
2500	−25.05	48.4	51.6
3000	−33.16	43.8	56.2

conclude that the Stokes drag force will play the key role for almost all of the fast and moderate ICMEs.

3.4.3 Kinematic Viscosity and Drag Coefficient for ICME–Solar Wind Interaction

Furthermore, Equation (3.3) also implies that the effective kinematic viscosity of the solar wind ($\nu_{\rm SW}$) exhibits a high value in the ICME–solar wind interaction system. Now, we estimate the value of $\nu_{\rm SW}$. Borgazzi et al. (2008) pointed out that the drag force is represented by $F = -6\pi\nu\rho d(V - V_{\rm bg})$ for Re $\ll 1$ by assuming a spherical body of ICMEs. We applied this expression to the linear term in Equation (3.3), and found

$$\frac{6\pi\nu_{\rm SW}\rho_{\rm SW}d}{m} = 4.84 \times 10^{-6}\ {\rm s}^{-1}, \tag{3.4}$$

where $\rho_{\rm SW}$, d, and m are the solar wind density, radial size, and mass of ICMEs, respectively. Substituting the values of $d = 4.49 \times 10^{10}$ m (= 0.3 AU) (Richardson and Cane, 2010), $m = 1.7 \times 10^{12}$ kg (Vourlidas et al., 2002), and $\rho_{\rm SW} = 1.67 \times 10^{-22}$ kg m^{-3} (in other words, the total mass density of 10 protons per cubic centimeter) in the above equation, we obtain $\nu_{\rm SW} = 5.8 \times 10^{16}$ m^2 s^{-1}. This value is an order of magnitude smaller than the viscosity estimated by Lara et al. (2011). On the other hand, if we use the value of viscosity estimated by them, we may estimate the mass of ICMEs instead of $\nu_{\rm SW}$. Lara et al. (2011) reported $\nu_{\rm SW} = 1.55 \times 10^{17}$ m^2 s^{-1} (from the speed-matching method) and 2.60×10^{17} m^2 s^{-1} (from the time-matching method) as the value of viscosity. Substituting this value into Equation (3.4) with the above d and $\rho_{\rm SW}$ values, we obtain $m \approx 10^{13}$ kg. This value corresponds to the upper limit of CME mass observed

using SOHO/LASCO (Gopalswamy et al., 2009) and is consistent with an estimation of the ICME mass in Jackson and Leinert (1985). Therefore, this analysis corroborates our expectation in Subsection 2.5 that ICMEs detected by the IPS observations are probably massive events.

Borgazzi et al. (2008) also showed that the drag force is described by $F = -(1/2)\mathrm{C_d} A\rho(V - V_{\mathrm{bg}})^2$ for $\mathrm{Re} \gg 1$, where $\mathrm{C_d}$ and A are the dimensionless drag coefficient and cross section of ICMEs, respectively. By applying this expression to the quadratic term in Equation (3.3) with $A = \pi(d/2)^2$, we can estimate the value of $\mathrm{C_d}$. Using the equation

$$\frac{\mathrm{C_d}\rho_{\mathrm{SW}}\pi d^2}{8m} = 2.07 \times 10^{-12}\ \mathrm{m}^{-1}, \tag{3.5}$$

and the above values of m, d, and ρ_{SW}, we find $\mathrm{C_d} = 27$. This value is almost three orders of magnitude smaller than the estimation by Lara et al. (2011); they reported $\mathrm{C_d} = 2.63 \times 10^3$ (from the speed-matching method) and 1.08×10^4 (from the time-matching method). Borgazzi et al. (2009) reported that $\mathrm{C_d}$ is $0.6 \times 10^5 - 1.6 \times 10^5$ (considering the variation in radius) or $2 \times 10^4 - 8 \times 10^4$ (considering the density variation) for the turbulent regime. Cargill (2004) showed by numerical simulations that $\mathrm{C_d}$ varies slowly between the Sun and the Earth, and is roughly unity for dense ICMEs. He also showed that when the ICME and solar wind densities are similar, $\mathrm{C_d}$ is larger than unity (between 3 and 10), but remains approximately constant with the radial distance. As shown here, each researcher reports different values of $\mathrm{C_d}$, and so it is difficult to determine its real value.

Chapter 4

Summary and Conclusions

4.1 Dissertation Summary

We investigated radial evolutions of propagation speeds for 46 ICMEs identified by SOHO/LASCO, IPS at 327 MHz, and in situ observations during 1997 – 2011 covering nearly the whole of Solar Cycle 23 and the ascending phase of Solar Cycle 24. we were left with 46 ICMEs; they traveled from the Sun to the Earth and were detected at three locations between the Sun and the Earth's orbit, i.e. the near-Sun, interplanetary space, and near-Earth. For these ICMEs, we determined reference distances and derive the propagation speeds and accelerations in the SOHO–IPS and IPS–Earth regions. Our examinations yielded the following results.

1. Fast ICMEs (with $V_{\rm SOHO} - V_{\rm bg} > 500$ km s^{-1}) rapidly decelerated, moderate ICMEs (with 0 km s^{-1} $\leq V_{\rm SOHO} - V_{\rm bg} \leq 500$ km s^{-1}) showed a little deceleration, while slow ICMEs (with $V_{\rm SOHO} - V_{\rm bg} < 0$ km s^{-1}) accelerated, where $V_{\rm SOHO}$ and $V_{\rm bg}$ are the initial speed of ICME and the speed of the background solar wind, respectively. Consequently, radial speeds converged to the speed of the background solar wind during their outward propagation, as shown in Figure 3.6. Thus, the distribution of ICME propagation speeds in the near-Earth region was narrower than in the near-Sun region. This was consistent with the earlier study by Lindsay et al. (1999).

2. The ICME deceleration was nearly complete by 0.79 ± 0.04 AU; this is consistent with an earlier result obtained by Gopalswamy et al. (2001). On the other hand, the acceleration of slow ICMEs ceased by 0.34 ± 0.03 AU; Temmer et al. (2011), Rollett et al. (2012), and Vršnak et al. (2013) presented similar results for slow ICMEs. Critical ICME speeds of zero acceleration (where the ICME acceleration

becomes zero) were derived from our analysis, i.e. 471 ± 19 km s^{-1} and 480 ± 21 km s^{-1} for a group of the fast and moderate ICMEs, and 479 ± 126 km s^{-1} for the slow ICMEs. These were somewhat higher than the values reported by Manoharan (2006) and Gopalswamy et al. (2000). However, this discrepancy was most likely explained by differences of data collection periods and criteria for the ICME identification from earlier studies. Critical ICME speeds in our result did not differ much from the typical speed of the solar wind, and we adopted the mean value of 480 km s^{-1} as the critical ICME speed for zero acceleration. This was close to the speed of the background solar wind, $V_{\rm bg} = 445 \pm 95$ km s^{-1}, during this period of study.

These results supported our assumption that ICMEs were accelerated or decelerated by a drag force caused by an interaction with the solar wind; the magnitude of the drag force acting upon ICMEs depended on the difference in speed, and, thus, ICMEs attained final speeds close to the solar wind speed when the force becomes zero.

4.1.1 Kinematics of Slow ICMEs

Our analyses for the slow ICMEs showed the following results: i) They accelerated toward the speed of the background solar wind during their propagation, and attain their final speed by 0.34 ± 0.03 AU. ii) The acceleration ended when they reach 479 ± 126 km s^{-1}; this was close to the typical speed of the solar wind during the period of this study. Examinations of the relationship between the difference in speed and the acceleration and the assessment of significance level for them showed that iii) Equation (2.2) with $\gamma_2 = 2.36\ (\pm 1.03) \times 10^{-11}$ m^{-1} was more suitable than Equation (2.1) to describe the kinematics of slow ICMEs. The result iii) was consistent with earlier studies by Maloney and Gallagher (2010) and Byrne et al. (2010).

However, six events of slow ICMEs in our sample are not sufficient to investigate their kinematics more precisely. Therefore, we need to identify more slow ICMEs and then examine their kinematics carefully.

4.1.2 Kinematics of Fast and Moderate ICMEs

For ICMEs with $V_{\rm SOHO} - V_{\rm bg} \geq 0$ km s^{-1}, Equation (2.1) with $\gamma_1 = 6.58(\pm 0.23) \times 10^{-6}$ s^{-1} was more appropriate than Equation (2.2) to describe their kinematics, because the reduced χ^2 for the linear equation satisfied the statistical significance level at 0.05, while the quadratic one did not. We found that this linear equation gave a good approximation for describing the motion of ICMEs with 0 km s^{-1} $\leq V - V_{\rm bg} <$ 1000 km s^{-1}.

We also found from detailed examinations of fast and moderate ICMEs that the value of coefficient γ_1 had a speed-dependence described by Equation (3.2). On the basis of these, we found a modified equation, $a = -2.07\times10^{-12}(V-V_{\rm bg})|V-V_{\rm bg}| -4.84\times10^{-6}(V-V_{\rm bg})$, for the ICME motion. We interpreted this equation as indicating that ICMEs with 0 km s^{-1} $\leq V - V_{\rm bg} \leq$ 2300 km s^{-1} were controlled mainly by the Stokes drag force, while the aerodynamic drag force was a predominant factor for the propagation of ICMEs with $V - V_{\rm bg} >$ 2300 km s^{-1}. Because such extremely fast ICMEs are very rare, we conclude that the Stokes drag force will play the key role for almost all of the fast and moderate ICMEs.

4.1.3 Properties of ICMEs Detected by IPS Observations and the ICME–Solar Wind Interaction

From the characteristics of IPS observations and the result of Cargill (2004) discussed in Section 2.5, we conclude that the ICMEs detected by IPS observations are probably massive events. Low-density ICMEs may not be detected by our system because radio scintillations are proportional to the solar wind density and we use a threshold g-value more severe than that used in earlier studies. We estimated the mass of ICMEs identified by our IPS observations to be 10^{12} – 10^{13} kg.

We also estimated the effective kinematic viscosity of the solar wind $\nu_{\rm SW}$ and the dimensionless drag coefficient $C_{\rm d}$ in the ICME–solar wind interaction system. Combining the linear term in Equation (3.3) and $F = -6\pi\nu\rho d(V - V_{\rm bg})$, we obtained $\nu_{\rm SW} = 5.8 \times 10^{16}$ m^2 s^{-1}; this was an order of magnitude smaller than the value in an earlier study by Lara et al. (2011). By comparing the quadratic term in Equation (3.3) with $F = -(1/2)C_{\rm d}A\rho(V - V_{\rm bg})^2$, we found $C_{\rm d} = 27$ for the value of drag coefficient.

4.2 Future Study

We investigated the kinematics of the 46 ICMEs using SOHO/LASCO, STEL IPS, and in situ observations and showed that the radial motion of ICMEs with $V_{\rm SOHO} - V_{\rm bg} \geq 0$ km s^{-1} was well described by the linear drag equation $a = -\gamma_1(V - V_{\rm bg})$ as shown in Figure 3.5. We find from Figure 3.5 that two of the fast ICMEs, which are the 8 November 2000 and 17 November 2001 events (see No. 18 and No. 25 in Table 2.1, respectively), have larger values of deceleration than the others in the SOHO–IPS region. We also find that not only the linear drag equation but also the quadratic equation $a = -\gamma_2(V - V_{\rm bg})|V - V_{\rm bg}|$ describe well the relationship between ICME accelerations and differences in speed for these two events. Figure 4.1 shows a comparison between

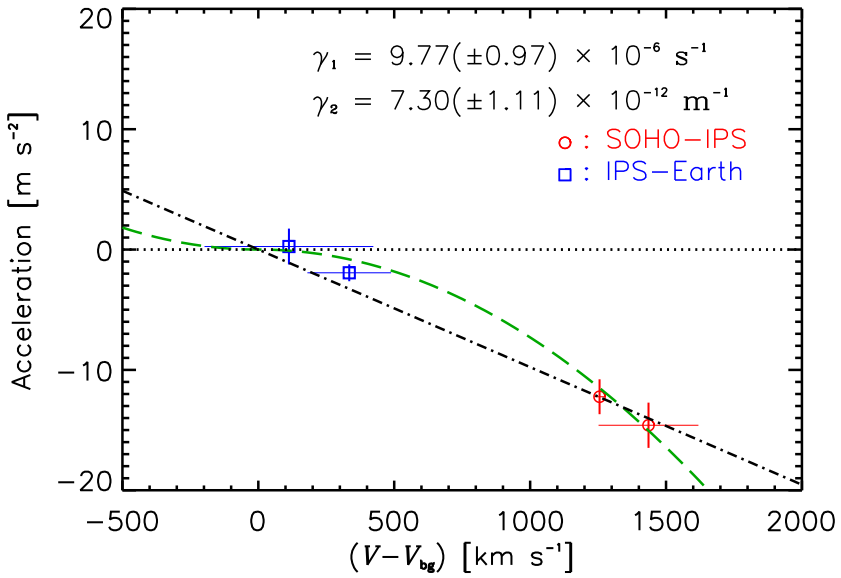

FIGURE 4.1: Relationship between acceleration a and difference in speed $(V - V_{\rm bg})$ for the 8 November 2000 and 17 November 2001 ICMEs. Circles (red) and squares (blue) denote data points in the SOHO–IPS and IPS–Earth regions, respectively. The dotted line shows the zero-acceleration line. The dash–dotted (black) line and the dashed (green) line denote acceleration–speed profiles of Equation (2.1) with $\gamma_1 = 9.77 \times 10^{-6}$ s^{-1} and Equation (2.2) with $\gamma_2 = 7.30 \times 10^{-12}$ m^{-1}, respectively.

two drag-force models for the 8 November 2000 and 17 November 2001 ICMEs. This result implies that there are some fast ICMEs whose dynamics are represented by the aerodynamic drag equation rather than the linear drag equation. It is an interesting topic whether drag forces acting predominantly on ICMEs are different depending on not only the velocity but also other properties of ICMEs. We find that the values of γ_1 and γ_2 for the above two ICMEs are larger than those for a group of fast and moderate ICMEs listed in Table 3.7. The larger γ_1 and γ_2 are obtained from the lower ICME density ($\propto m/d^3$) or/and larger $\rho_{\rm SW}$ because $\gamma_1 \propto \rho_{\rm SW} d/m$ and $\gamma_2 \propto \rho_{\rm SW} d^2/m$ from Borgazzi et al. (2008). Therefore, we consider that ICMEs controlled mainly by the aerodynamic drag force with $V - V_{\rm bg} < 2300$ km s^{-1} have the lower density than the others governed by Stokes drag force. However, we can not bring a conclusive result for this question because of a few samples at present. We need to identify more fast ICMEs to study this subject.

A combination of the space-borne coronagraph, ground-based IPS, and satellite in-situ observations serves to detect many ICMEs between the Sun and the Earth, and is a useful means to study their kinematics. Joint observations of ICMEs by IPS and STEREO/HI will enable us to estimate the mass and volume of ICMEs more accurately. Most of Earth-reached ICMEs are observed as halo CMEs in the SOHO/LASCO FOV. Their mass has not been estimated accurately because of some difficulties to make measurements of their electron density from coronagraph observations. Determination of

the ICME mass is very important for a study of the ICME kinematics with drag-force models.

In this study, we disregarded the contribution of magnetic field to the ICME propagation. Richardson and Cane (2010) pointed out that at least 30% of ICMEs had a magnetic flux rope. Manoharan and Mujiber Rahman (2011) investigated the relationship between the propagation speed and internal energy of ICMEs. They suggested that the magnetic energy stored in ICMEs was utilized to overcome the drag force. Therefore, a more precise examination of the ICME dynamics requires to include the magnetic effect(s) in drag-force models. Shiota et al. (2013) developed a three-dimensional MHD model for ICMEs, which could evaluate both a drag force by the interaction with the solar wind and a driving force due to the internal magnetic field on the ICME propagation. An investigation of the ICME kinematics using IPS and STEREO/HI observations with this MHD model would be very interesting.

Appendix A

IPS g-maps for the 46 ICMEs

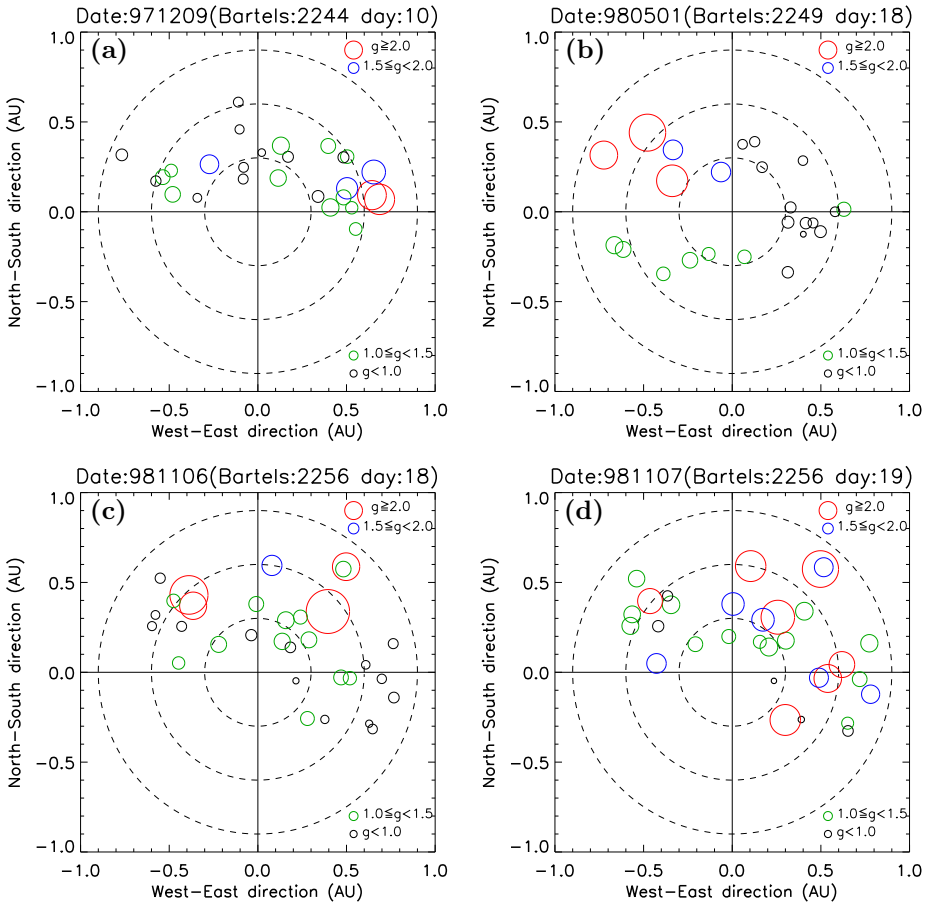

FIGURE A.1: The g-maps on (a) 9 April 1997, (b) 1 May 1998, (c) 6 November 1998, and (d) 7 November 1998. In each panel, the g-map center corresponds to the location of the Sun, and concentric circles indicate radial distances of 0.3 AU, 0.6 AU, and 0.9 AU. Colored open solid circles indicate the locations of the closest point to the Sun (the P-point) on the LOS for the radio sources in the sky plane. The center of the colored circle indicates the heliocentric distance of the P-point on the LOS, and color and diameter represent the g-value level for each source; $g < 1.0$ (black), $1.0 \leq g < 1.5$ (green), $1.5 \leq g < 2.0$ (blue), and $g \geq 2.0$ (red).

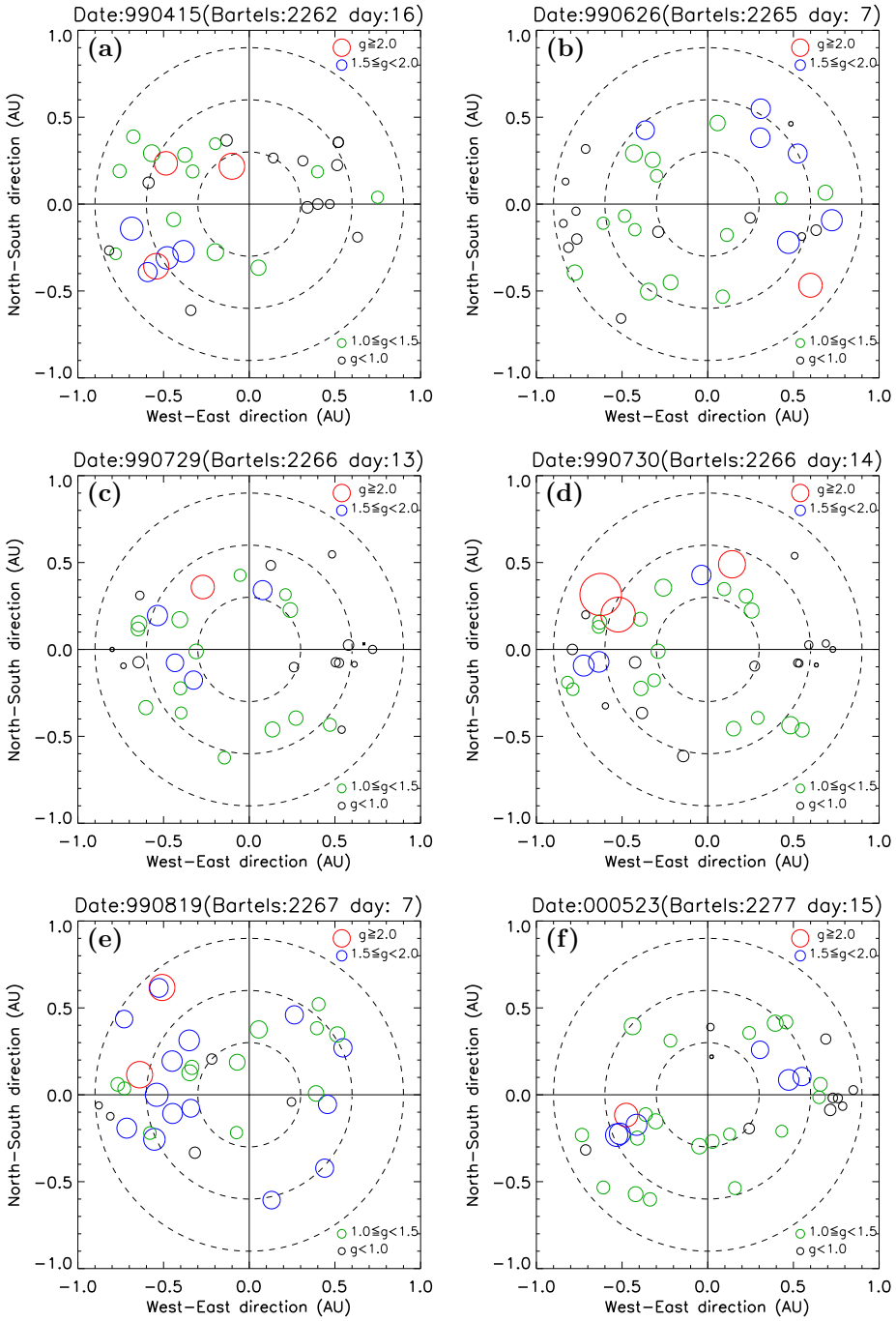

FIGURE A.2: The *g*-maps on (a) 15 April 1999, (b) 26 June 1999, (c) 29 July 1999, (d) 30 July 1999, (e) 19 August 1999, and (f) 23 May 2000.

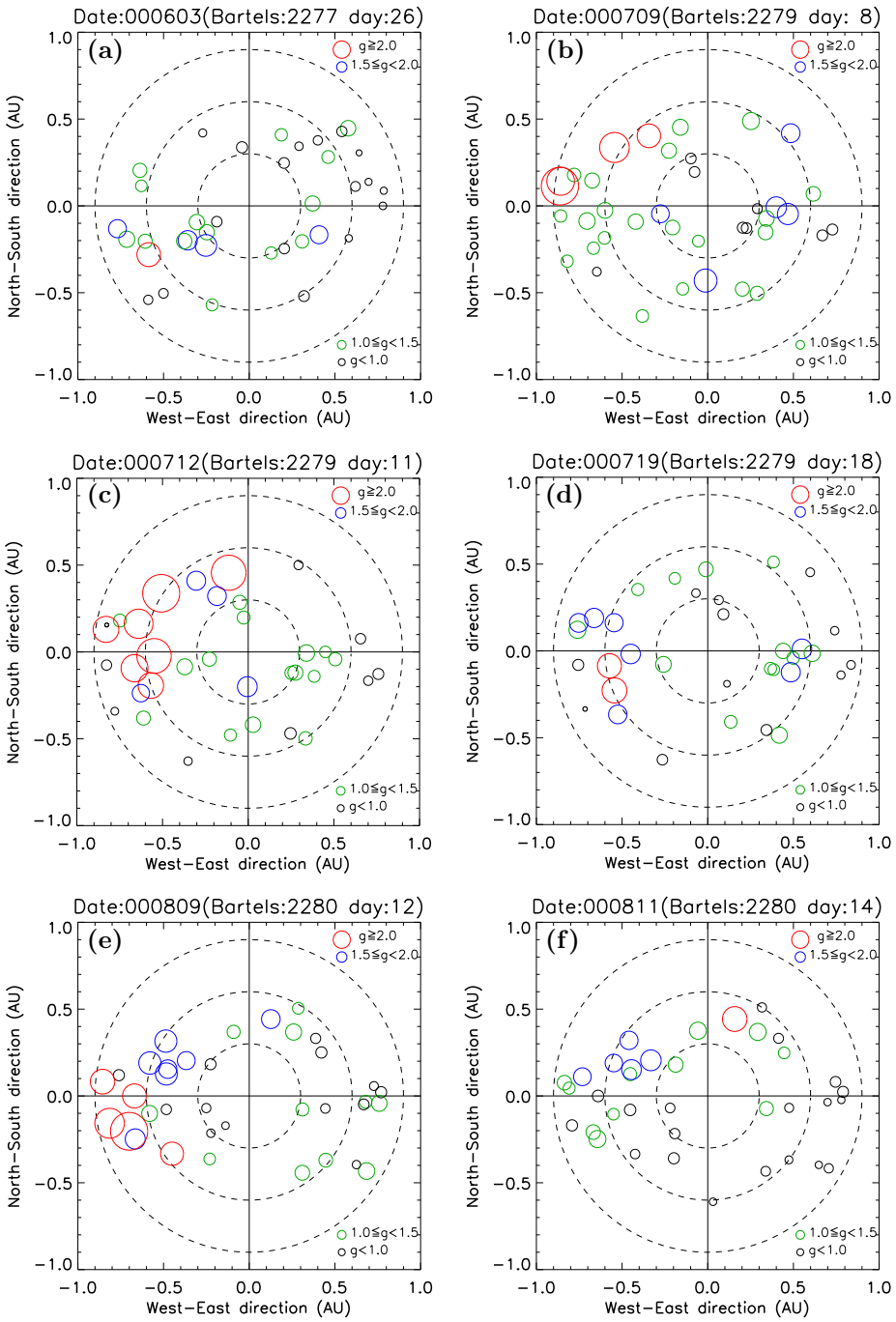

FIGURE A.3: The *g*-maps on (a) 3 June 2000, (b) 9 July 2000, (c) 12 July 2000, (d) 19 July 2000, (e) 9 August 2000, and (f) 11 August 2000.

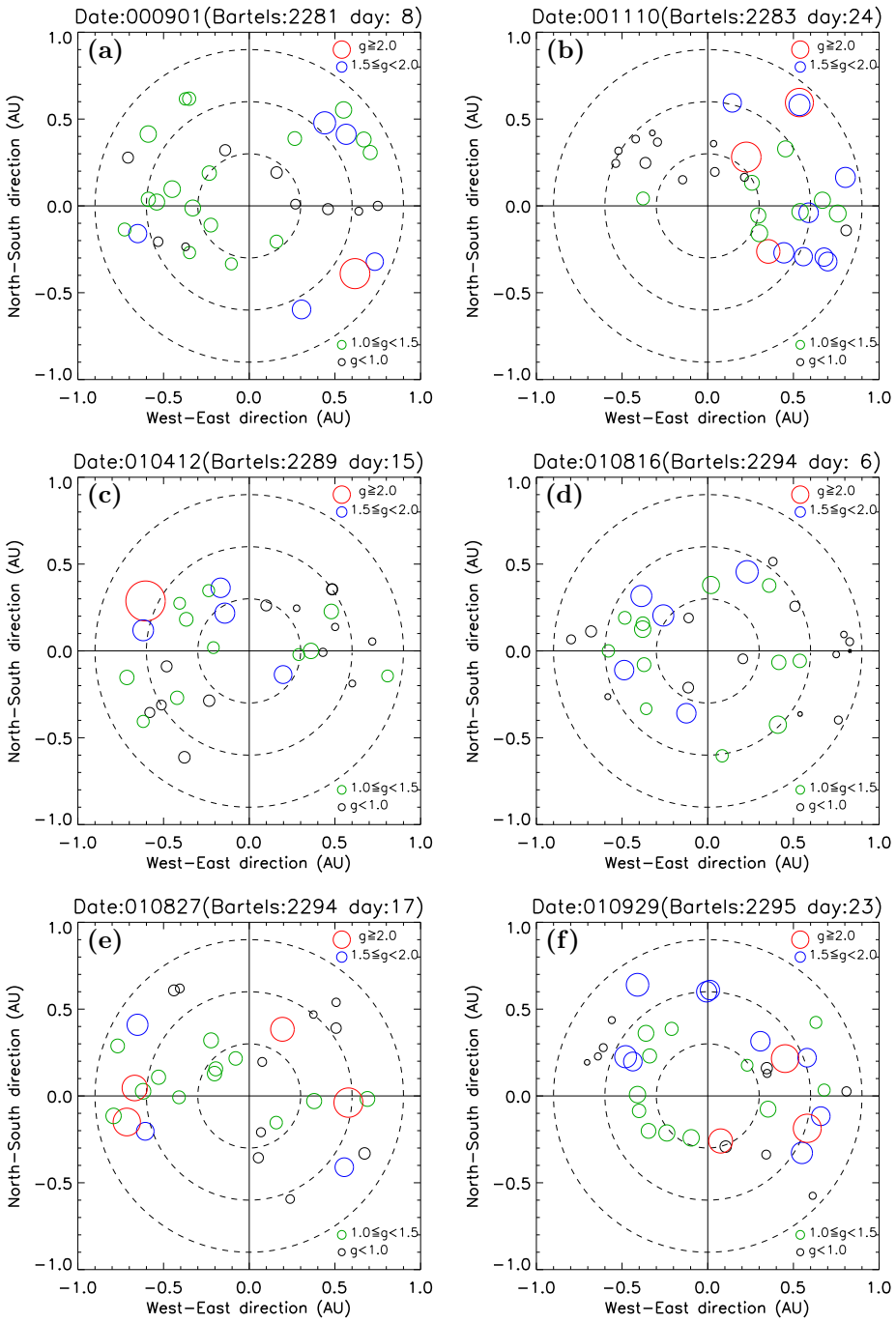

FIGURE A.4: The *g*-maps on (a) 1 September 2000, (b) 10 November 2000, (c) 12 April 2001, (d) 16 August 2001, (e) 27 August 2001, and (f) 29 September 2001.

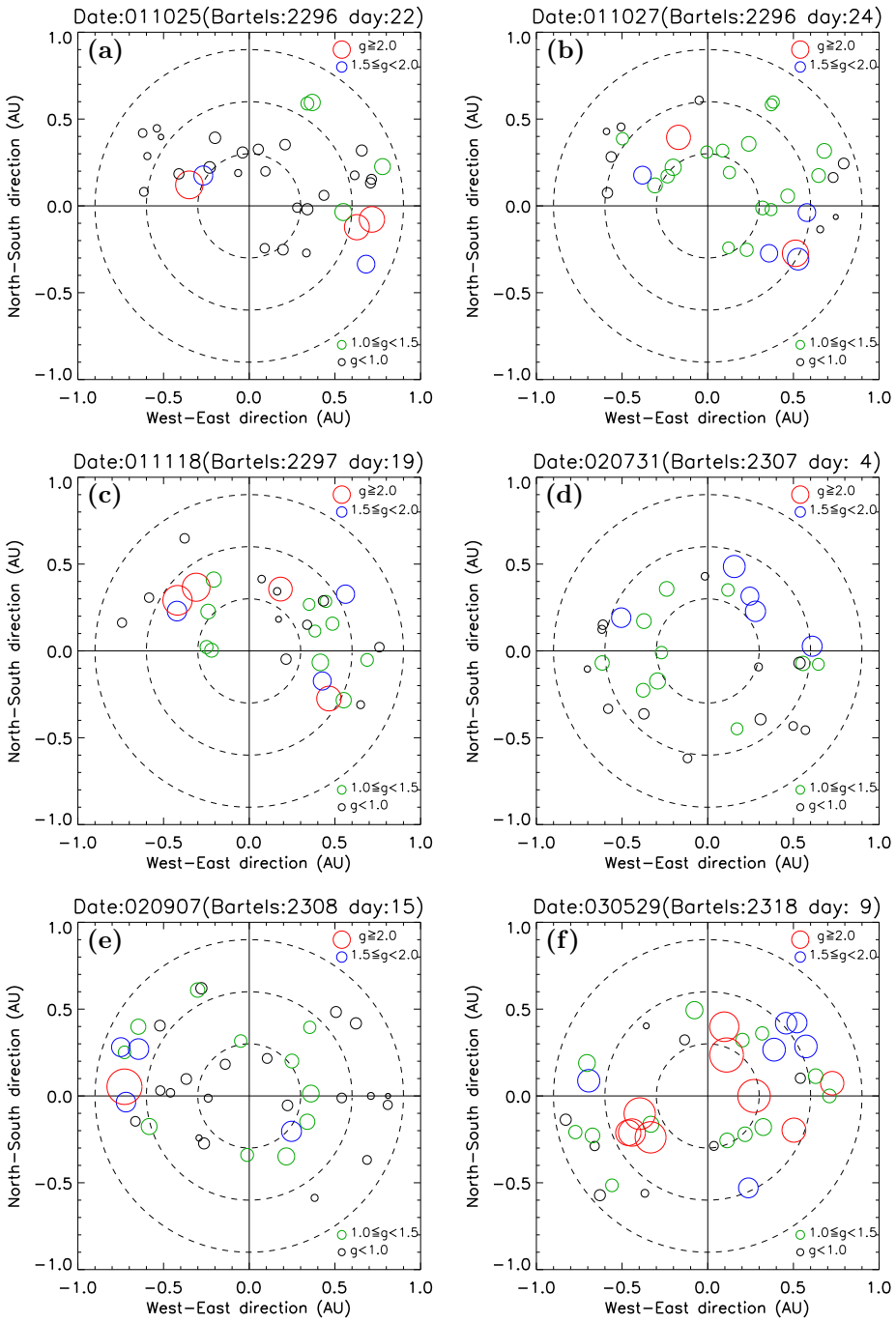

FIGURE A.5: The *g*-maps on (a) 25 October 2001, (b) 27 October 2001, (c) 18 November 2001, (d) 31 July 2002, (e) 7 September 2002, and (f) 29 May 2003.

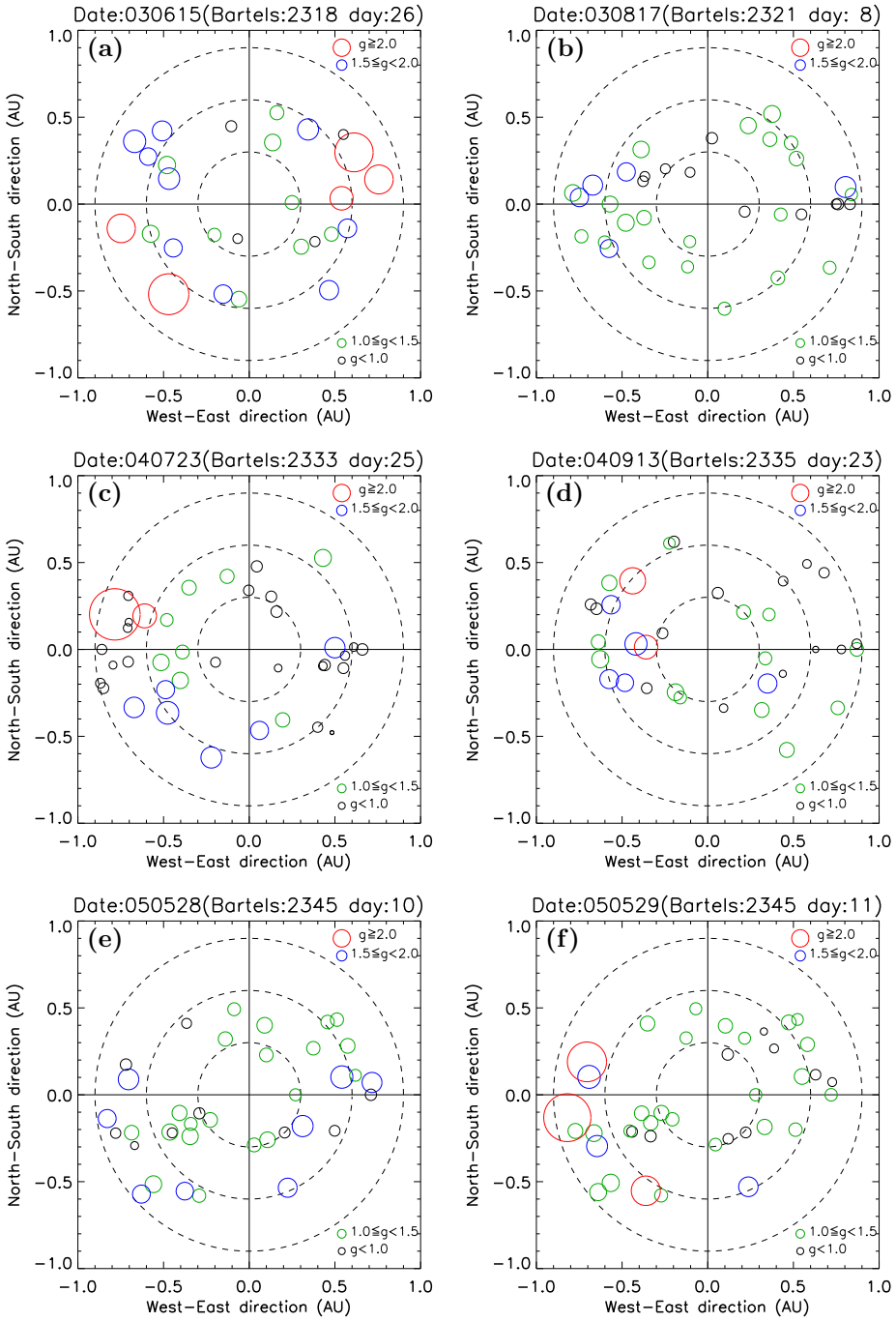

FIGURE A.6: The *g*-maps on (a) 15 June 2003, (b) 17 August 2003, (c) 23 July 2004, (d) 13 September 2004, (e) 28 May 2005, and (f) 29 May 2005.

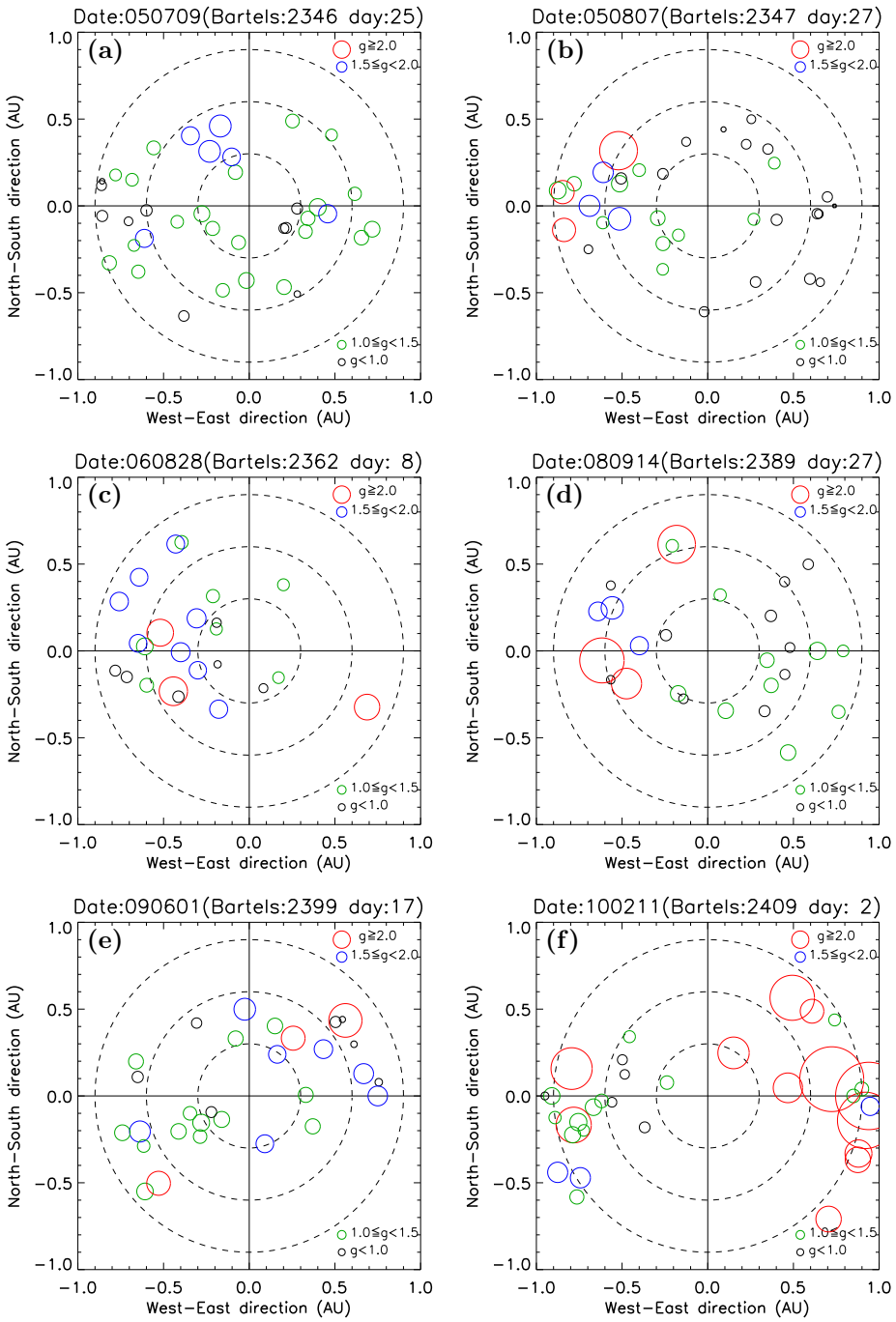

FIGURE A.7: The *g*-maps on (a) 9 July 2005, (b) 7 August 2005, (c) 28 August 2006, (d) 14 September 2008, (e) 1 June 2009, and (f) 11 February 2010.

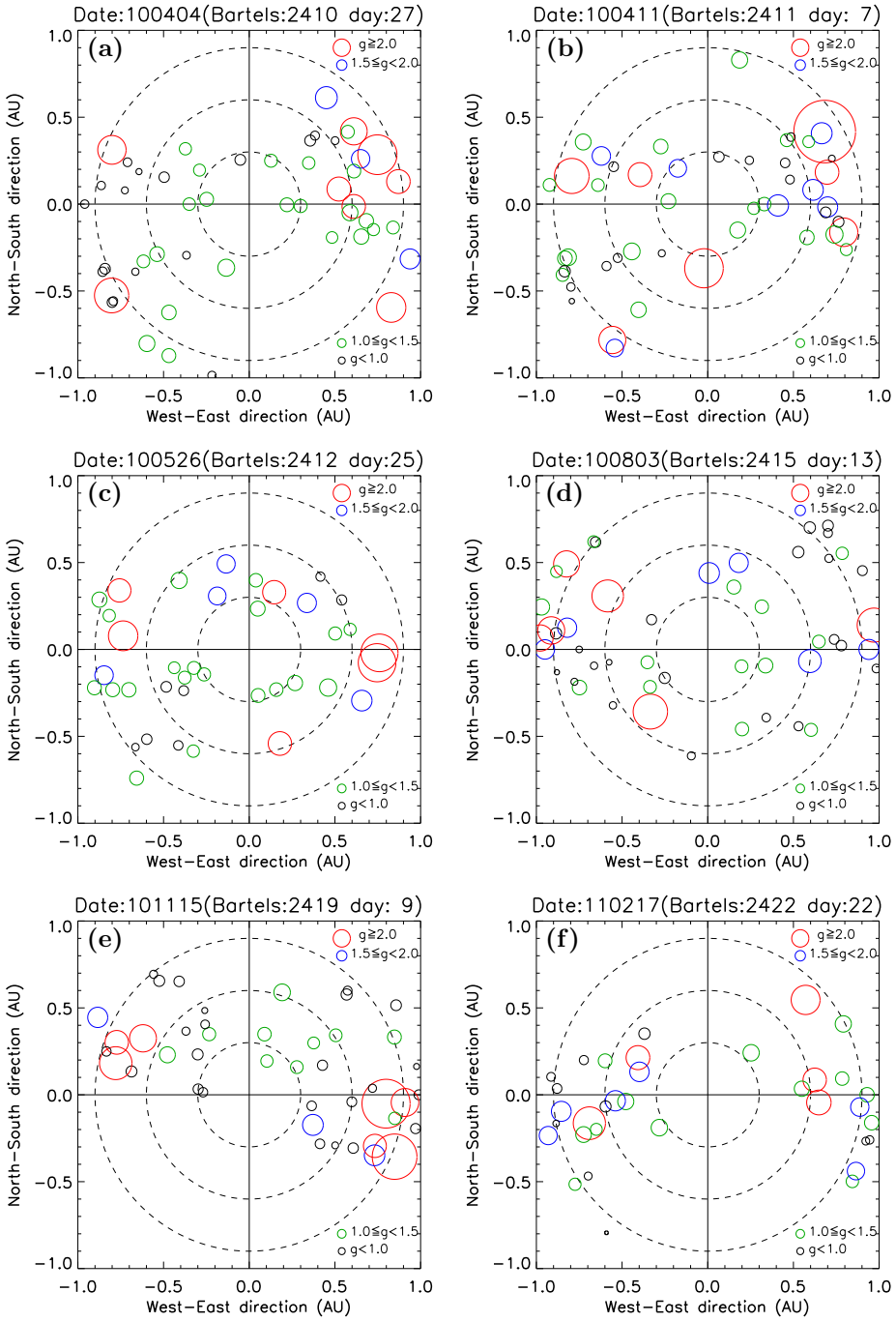

FIGURE A.8: The *g*-maps on (a) 4 April 2010, (b) 11 April 2010, (c) 26 May 2010, (d) 3 August 2010, (e) 15 November 2010, and (f) 17 February 2011.

References

M. H. Acuña, K. W. Ogilvie, D. N. Baker, S. A. Curtis, D. H. Fairfield, and W. H. Mish. The global geospace science program and its investigations. *Space Sci. Rev.*, 71(1-4): 5–21, 1995. doi: 10.1007/BF00751323.

K. A. Anderson and J. R. Winckler. Solar flare X-ray burst on September 28, 1961. *J. Geophys. Res.*, 67(11):4103–4117, 1962.

M. D. Andrews. Lasco and eit observations of the bastille day 2000 solar storm. *Solar Phys.*, 204(1):179–196, 2001. doi: 10.1023/A:1014215923912.

T. D. Antonova and V. V. Vitkevich. Results of radio observations of irregularities in the interplanetary plasma, 1965-1966. *Soviet Astron.*, 12:788–795, 1969.

D. Antrack, L. Biermann, and R. Lüst. Some statistical properties of comets with plasma tails. *Ann. Rev. Astron. Astrophys.*, 2:327–340, 1964. doi: 10.1146/annurev.aa.02.090164.001551.

U. Anzer. Can coronal loop transients be driven magnetically? *Solar Phys.*, 57(1): 111–118, 1978. doi: 10.1007/BF00152048.

J. W. Armstrong and W. A. Coles. Analysis of three-station interplanetary scintillation. *J. Geophys. Res.*, 77(25):4602–4610, 1972.

K. Asai, Y. Ishida, M. Kojima, K. Maruyama, H. Misawa, and N. Yoshimi. Multi-station system for solar wind observations using the interplanetary scintillation method. *J. Geomagn. Geoelectr.*, 47(11):1107–1112, 1995.

S. J. Bame, J. R. Asbridge, W. C. Feldman, and J. T. Gosling. Solar cycle evolution of high-speed solar wind streams. *Astrophys. J.*, 207:977–980, 1976. doi: 10.1086/154566.

S. J. Bame, J. R. Asbridge, W. C. Feldman, and J. T. Gosling. Evidence for a structure-free state at high solar wind speeds. *J. Geophys. Res.*, 82(10):1487–1492, 1977.

S. J. Bame, J. R. Asbridge, W. C. Feldman, E. E. Fenimore, and J. T. Gosling. Solar wind heavy ions from flare-heated coronal plasma. *Solar Phys.*, 62(1):179–201, 1979. doi: 10.1007/BF00150143.

J. Bartels. Terrestrial-magnetic activity and its relations to solar phenomena. *Terr. Magn. Atmos. Electr.*, 37(1):1–52, 1932.

A. Bellomo and A. Mavretic. MIT plasma experiment on IMP H and J Earth orbited satellites. *MIT Center for Space Research Technical Report CSR MIT TR-78–2*, page 51, 1978.

L. Biermann. Kometenschweife und solare korpuskularstrahlung. *Z. Astrophys.*, 29: 274–286, 1951.

K. Birkeland. *The Norwegian aurora polaris expedition 1902–1903*, volume 1. H. Aschehoug & Company, Christiania, 1908.

M. M. Bisi, A. R. Breen, B. V. Jackson, R. A. Fallows, A. P. Walsh, Z. Mikić, P. Riley, C. J. Owen, A. Gonzalez-Esparza, E. Aguilar-Rodriguez, et al. From the Sun to the Earth: the 13 May 2005 coronal mass ejection. *Solar Phys.*, 265(1–2):49–127, 2010.

J. D. Bohlin, K. J. Frost, P. T. Burr, A. K. Guha, and G. L. Withbroe. Solar Maximum Mission. *Solar Phys.*, 65(1):5–14, 1980.

A. Borgazzi, A. Lara, L. Romero-Salazar, and A. Ventura. Transport in the interplanetary medium of coronal mass ejections. *Geofis. int.*, 47(3):301–310, 2008.

A. Borgazzi, A. Lara, E. Echer, and M. V. Alves. Dynamics of coronal mass ejections in the interplanetary medium. *Astron. Astrophys.*, 498(3):885–889, 2009. doi: 10.1051/0004-6361/200811171.

G. Borrini, J. T. Gosling, S. J. Bame, and W. C. Feldman. Helium abundance enhancements in the solar wind. *J. Geophys. Res.*, 87(A9):7370–7378, 1982. doi: 10.1029/JA087iA09p07370.

G. E. Brueckner, R. A. Howard, M. J. Koomen, C. M. Korendyke, D. J. Michels, J. D. Moses, D. G. Socker, K. P. Dere, P. L. Lamy, A. Llebaria, M. V. Bout, R. Schwenn, G. M. Simnett, D. K. Bedford, and C. J. Eyles. The large angle spectroscopic coronagraph (LASCO). *Solar Phys.*, 162(1):357–402, 1995. doi: 10.1007/BF00733434.

G. E. Brueckner, J. P. Delaboudiniere, R. A. Howard, S. E. Paswaters, O. C. St. Cyr, R Schwenn, P Lamy, G. M. Simnett, B. Thompson, and D. Wang. Geomagnetic storms caused by coronal mass ejections(CMEs): March 1996 through June 1997. *Geophys. Res. Lett.*, 25(15):3019–3022, 1998. doi: 10.1029/98GL00704.

L. F. Burlaga, L. Klein, N. R. Sheeley, D. J. Michels, R. A. Howard, M. J. Koomen, R. Schwenn, and H. Rosenbauer. A magnetic cloud and a coronal mass ejection. *Geophys. Res. Lett.*, 9(12):1317–1320, 1982. doi: 10.1029/GL009i012p01317.

L. F. Burlaga, E. R. Lepping, and J. A. Jones. Coronal mass ejections and magnetic flux ropes in interplanetary space. In C. T. Russell, E. R. Priest, and L. C. Lee, editors, *Physics of Magnetic Flux Ropes*, volume 58 of *Geophysical Monograph*, pages 373–377, Washington, DC, 1990. American Geophysical Union. doi: 10.1029/GM058p0373.

J. Burnell. Enhancements of interplanetary scintillation, corotating streams and forbush decreases. *Nature*, 224:356–357, 1969. doi: 10.1038/224356a0.

J. P. Byrne, S. A. Maloney, R. T. J. McAteer, J. M. Refojo, and P. T. Gallagher. Propagation of an Earth-directed coronal mass ejection in three dimensions. *Nat. Commun.*, 1:74, 2010.

H. V. Cane and I. G. Richardson. Interplanetary coronal mass ejections in the near-Earth solar wind during 1996–2002. *J. Geophys. Res.*, 108(A4), 2003. doi: 10.1029/2002JA009817.

H. V. Cane, I. G. Richardson, and O. C. St. Cyr. Coronal mass ejections, interplanetary ejecta and geomagnetic storms. *Geophys. Res. Lett.*, 27(21):3591–3594, 2000. doi: 10.1029/2000GL000111.

P. J. Cargill. On the aerodynamic drag force acting on interplanetary coronal mass ejections. *Solar Phys.*, 221(1):135–149, 2004. doi: 10.1023/B:SOLA.0000033366.10725.a2.

P. J. Cargill, J. Chen, D. S. Spicer, and S. T. Zalesak. Geometry of interplanetary magnetic clouds. *Geophys. Res. Lett.*, 22(5):647–650, 1995. doi: 10.1029/95GL00013.

H. Carmichael. A process for flares. In W. N. Hess, editor, *The Physics of Solar Flares*, volume SP-50 of *NASA spacial pulications*, pages 451–456, Washington, DC., 1964. NASA Scientific and Technical Information Division.

R. C. Carrington. Description of a singular appearance seen in the sun on September 1, 1859. *Mon. Not. Roy. Astron. Soc.*, 20:13–15, 1859. doi: 10.1093/mnras/20.1.13.

S. Chapman. Corpuscular influences upon the upper atmosphere. *J. Geophys. Res.*, 55 (4):361–372, 1950.

S. Chapman and V. C. A. Ferraro. A new theory of magnetic storms. *Terr. Magn. Atmos. Electr.*, 36(2):77–97, 1931a.

S. Chapman and V. C. A. Ferraro. A new theory of magnetic storms. *Terr. Magn. Atmos. Electr.*, 36(3):171–186, 1931b.

S. Chapman and H. Zirin. Notes on the solar corona and the terrestrial ionosphere. *Smithsonian Contributions to Astrophysics*, 2:1, 1957.

J. Chen. Effects of toroidal forces in current loops embedded in a background plasma. *Astrophys. J.*, 338:453–470, 1989. doi: 10.1086/167211.

J. Chen. Theory of prominence eruption and propagation: Interplanetary consequences. *J. Geophys. Res.*, 101(A12):27499–27, 1996. doi: 10.1029/96JA02644.

J. Chen and D. A. Garren. Interplanetary magnetic clouds: Topology and driving mechanism. *Geophys. Res. Lett.*, 20(21):2319–2322, 1993. doi: 10.1029/93GL02426.

P. F. Chen. Coronal mass ejections: Models and their observational basis. *Living Rev. Solar Phys.*, 8:1, 2011. doi: 10.12942/lrsp-2011-1. URL http://www.livingreviews.org/lrsp-2011-1.

E. W. Cliver and L. Svalgaard. The 1859 solar–terrestrial disturbance and the current limits of extreme space weather activity. *Solar Phys.*, 224(1-2):407–422, 2004. doi: 10.1007/s11207-005-4980-z.

W. A. Coles, J. K. Harmon, A. J. Lazarus, and J. D. Sullivan. Comparison of 74-MHz interplanetary scintillation and IMP 7 observations of the solar wind during 1973. *J. Geophys. Res.*, 83(A7):3337–3341, 1978. doi: 10.1029/JA083iA07p03337.

C. Collinson and T. Roper. *Particle Mechanics*. Butterworth-Heinemann, 1995. ISBN 978-0340610466.

H. L. DeMastus, W. J. Wagner, and R. D. Robinson. Coronal disturbances. *Solar Phys.*, 31(2):449–459, 1973. doi: 10.1007/BF00152820.

P. A. Dennison and A. Hewish. The solar wind outside the plane of the ecliptic. *Nature*, 213:343–346, 1967.

M. Dryer, H. Pérez-de Tejada, H. A. Taylor, D. S. Intriligator, J. D. Mihalov, and B. Rompolt. Compression of the venusian ionosphere on May 10, 1979, by the interplanetary shock generated by the solar eruption of May 8, 1979. *J. Geophys. Res.*, 87(A11):9035–9044, 1982. doi: 10.1029/JA087iA11p09035.

P. J. Duffett-Smith, A. Purvis, and A. Hewish. A statistical study of faint radio sources at 81.5 MHz–I. The data. *Mon. Not. Roy. Astron. Soc.*, 190(4):891–901, 1980. doi: 10.1093/mnras/190.4.891.

B. Edlén. Die deutung der emissionslinien im spektrum der sonnenkorona. *Z. Astrophys.*, 22:30–64, 1943.

A. Egeland. Kristian Birkeland: The first space scientist. *J. Atmos. Solar-Terr. Phys.*, 71(17):1749–1755, 2009.

C. J. Eyles, G. M. Simnett, M. P. Cooke, B. V. Jackson, A. Buffington, P. P. Hick, N. R. Waltham, J. M. King, P. A. Anderson, and P. E. Holladay. The solar mass ejection imager (SMEI). *Solar Phys.*, 217(2):319–347, 2003. doi: 10.1023/B:SOLA.0000006903.75671.49.

C. J. Eyles, R. A. Harrison, C. J. Davis, N. R. Waltham, B. M. Shaughnessy, H. C. A. Mapson-Menard, D. Bewsher, S. R. Crothers, J. A. Davies, G. M. Simnett, et al. The Heliospheric Imagers onboard the STEREO mission. *Solar Phys.*, 254(2):387–445, 2009. doi: 10.1007/s11207-008-9299-0.

L. A. Frank, K. L. Ackerson, W. R. Paterson, J. A. Lee, M. R. English, and G. L. Pickett. The comprehensive plasma instrumentation (CPI) for the GEOTAIL spacecraft. *J. Geomagn. Geoelectr.*, 46(1):23–37, 1994.

G. R. Gapper, A. Hewish, A. Purvis, and P. J. Duffett-Smith. Observing interplanetary disturbances from the ground. *Nature*, 296:633–636, 1982. doi: 10.1038/296633a0.

G. Gloeckler, J. Cain, F. M. Ipavich, E. O. Tums, P. Bedini, L. A. Fisk, T. H. Zurbuchen, P. Bochsler, J. Fischer, R. F. Wimmer-Schweingruber, J. Geiss, and R. Kallenbach. Investigation of the composition of solar and interstellar matter using solar wind and pickup ion measurements with SWICS and SWIMS on the ACE spacecraft. *Space Sci. Rev.*, 86(1):497–539, 1998. doi: 10.1023/A:1005036131689.

T. Gold. Plasma and magnetic fields in the solar system. *J. Geophys. Res.*, 64(11): 1665–1674, 1959. doi: 10.1029/JZ064i011p01665.

W. D. Gonzalez, J. A. Joselyn, Y. Kamide, H. W. Kroehl, G. Rostoker, B. T. Tsurutani, and V. M. Vasyliunas. What is a geomagnetic storm? *J. Geophys. Res.*, 99(A4): 5771–5792, 1994. doi: 10.1029/93JA02867.

N. Gopalswamy. A global picture of cmes in the inner heliosphere. In G. Pletto and S. T. Suess, editors, *The sun and the heliosphere as an integrated system*, volume 317 of *Astrophysics and Space Science Library*, pages 201–251. Kluwer Academic Publishers, Dordrecht, 2004.

N. Gopalswamy, A. Lara, R. P. Lepping, M. L. Kaiser, D. Berdichevsky, and O. C. St. Cyr. Interplanetary acceleration of coronal mass ejections. *Geophys. Res. Lett.*, 27 (2):145–148, 2000. doi: 10.1029/1999GL003639.

N. Gopalswamy, A. Lara, S. Yashiro, M. L. Kaiser, and R. A. Howard. Predicting the 1-AU arrival times of coronal mass ejections. *J. Geophys. Res.*, 106(A12):29–207, 2001. doi: 10.1029/2001JA000177.

N. Gopalswamy, M. Shimojo, W. Lu, S. Yashiro, K. Shibasaki, and R. A. Howard. Prominence eruptions and coronal mass ejection: a statistical study using microwave observations. *Astrophys. J.*, 586(1):562–578, 2003. doi: 10.1086/367614.

N. Gopalswamy, S. Yashiro, Y. Liu, G. Michalek, A. Vourlidas, M. L. Kaiser, and R. A. Howard. Coronal mass ejections and other extreme characteristics of the 2003 October–November solar eruptions. *J. Geophys. Res.*, 110:A09S15, 2005. doi: 10.1029/2004JA010958.

N. Gopalswamy, S. Yashiro, G. Michalek, G. Stenborg, A. Vourlidas, S. Freeland, and R. Howard. The SOHO/LASCO CME catalog. *Earth Moon Planets*, 104(1):295–313, 2009. doi: 10.1007/s11038-008-9282-7.

J. T. Gosling. Coronal mass ejections and magnetic flux ropes in interplanetary space. In C. T. Russell, E. R. Priest, and L. C. Lee, editors, *Physics of Magnetic Flux Ropes*, volume 58 of *Geophysical Monograph*, pages 343–364, Washington, DC, 1990. American Geophysical Union. doi: 10.1029/GM058p0343.

J. T. Gosling, J. R. Asbridge, S. J. Bame, A. J. Hundhausen, and I. B. Strong. Satellite observations of interplanetary shock waves. *J. Geophys. Res.*, 73(1):43–50, 1968. doi: 10.1029/JA073i001p00043.

J. T. Gosling, R. T. Hansen, and S. J. Bame. Solar wind speed distributions: 1962–1970. *J. Geophys. Res.*, 76:1811–1814, 1971. doi: 10.1029/JA076i007p01811.

J. T. Gosling, E. Hildner, R. M. MacQueen, R. H. Munro, A. I. Poland, and C. L. Ross. Mass ejections from the sun: A view from Skylab. *J. Geophys. Res.*, 79(31):4581–4587, 1974. doi: 10.1029/JA079i031p04581.

J. T. Gosling, E. Hildner, R. M. MacQueen, R. H. Munro, A. I. Poland, and C. L. Ross. Direct observations of a flare related coronal and solar wind disturbance. *Solar Phys.*, 40(2):439–448, 1975.

J. T. Gosling, E. Hildner, R. M. MacQueen, R. H. Munro, A. I. Poland, and C. L. Ross. The speeds of coronal mass ejection events. *Solar Phys.*, 48(2):389–397, 1976. doi: 10.1007/BF00152004.

J. T. Gosling, D. N. Baker, S. J. Bame, W. C. Feldman, R. D. Zwickl, and E. J. Smith. Bidirectional solar wind electron heat flux events. *J. Geophys. Res.*, 92(A8):8519–8535, 1987. doi: 10.1029/JA092iA08p08519.

J. T. Gosling, S. J. Bame, D. J. McComas, and J. L. Phillips. Coronal mass ejections and large geomagnetic storms. *Geophys. Res. Lett.*, 17(7):901–904, 1990. doi: 10.1029/GL017i007p00901.

J. T. Gosling, D. J. McComas, J. L. Phillips, and S. J. Bame. Geomagnetic activity associated with earth passage of interplanetary shock disturbances and coronal mass ejections. *J. Geophys. Res.*, 96(A5):7831–7839, 1991. doi: 10.1029/91JA00316.

W. M. H. Greaves and H. W. Newton. On the recurrence of magnetic storms. *Mon. Not. Roy. Astron. Soc.*, 89:641–646, 1929. doi: 10.1093/mnras/89.7.641.

K. I. Gringauz, V. V. Bezrukikh, V. D. Ozerov, and R. E. Rybchinskii. Investigation of interplanetary ionized gas, high energy electrons and solar corpuscular radiation by means of three-electrode traps for charge-carrying particles installed on the second Soviet space rocket. *Doklady Akad. Nauk SSSR*, 131:1301, 1960.

W. Grotrian. Ergebnisse der potsdamer expedition zur beobachtung der sonnenfinsternis am 9. Mai 1929 in Takengon (Nordsumatra). 8. Mitteilung. über den intensitätsverlauf und das intensitätsverhältnis der koronalinien. Mit 12 abbildungen. *Z. Astrophys.*, 7: 26–45, 1933.

W. Grotrian. Zur frage der deutung der linien im spektrum der sonnenkorona. *Naturwissenschaften*, 27(13):214–214, 1939.

M. Guhathakurta and R. Fisher. Solar wind consequences of a coronal hole density profile: Spartan 201-03 coronagraph and Ulysses observations from 1.15 $R_{\odot}$ to 4 AU. *Astrophys. J. Lett.*, 499(2):L215, 1998. doi: 10.1086/311371.

G. E. Hale. A remarkable solar disturbance. *Astron. Astrophys.*, 11:611–613, 1892.

G. E. Hale. The spectrohelioscope and its work. Part III. Solar erruptions an their apparent terrestrial effects. *Astrophys. J.*, 73:379–412, 1931. doi: 10.1086/143316.

A. Hewish and S. Bravo. The sources of large-scale heliospheric disturbances. *Solar Phys.*, 106(1):185–200, 1986. doi: 10.1007/BF00161362.

A. Hewish, P. F. Scott, and D. Wills. Interplanetary scintillation of small diameter radio sources. *Nature*, 203(4951):1214–1217, 1964. doi: 10.1038/2031214a0.

A. Hewish, S. J. Bell, J. D. H Pilkington, P. F. Scott, and R. A. Collins. Observation of a rapidly pulsating radio source. *Nature*, 217(5130):709–713, 1968.

T. Hirayama. Theoretical model of flares and prominences. *Solar Phys.*, 34(2):323–338, 1974. doi: 10.1007/BF00153671.

T. Hirayama. Modern observations of solar prominences. *Solar Phys.*, 100(1-2):415–434, 1985. doi: 10.1007/BF00158439.

C. Hoffmeister. Physikalische untersuchungen an kometen. I. Die beziehungen des primären schweifstrahls zum radiusvektor. Mit 2 abbildungen. *Z. Astrophys.*, 22: 265–285, 1943.

Z. Houminer. Flare-associated shock waves observed by interplanetary scintillation. *Planet. Space Sci.*, 24(10):951–954, 1976.

T. Howard. *Coronal Mass Ejections: An Introduction*. Springer, New York, 2011. doi: 10.1007/978-1-4419-8789-1.

T. A. Howard and C. E. DeForest. Inner heliospheric flux rope evolution via imaging of coronal mass ejections. *Astrophys. J.*, 746(1):64, 2012.

H. S. Hudson, L. E. Peterson, and D. A. Schwartz. Solar and cosmic X-rays above 7.7 keV. *Solar Phys.*, 6(2):205–215, 1969.

A. J. Hundhausen. The origin and propagation of coronal mass ejections (R). In V. J. Pizzo, T. Holzer, and D. G. Sime, editors, *Proceedings of the Sixth International Solar Wind Conference*, volume 1 of *NCAR Thechnical Note*, pages 181–214, Colorado, 1987. National Center for Atmospheric Research.

A. J. Hundhausen. The solar wind. In M. G. Kivelson and C. T. Russell, editors, *Introduction to space physics*, pages 91–128, Cambridge, 1995. Cambridge University Press.

A. J. Hundhausen, S. J. Bame, and M. D. Montgomery. Large-scale characteristics of flare-associated solar wind disturbances. *J. Geophys. Res.*, 75(25):4631–4642, 1970. doi: 10.1029/JA075i025p04631.

B. V. Jackson. Helios observations of the earthward-directed mass ejection of 27 November, 1979. *Solar Phys.*, 95(2):363–370, 1985a. doi: 10.1007/BF00152413.

B. V. Jackson. Imaging of coronal mass ejections by the Helios spacecraft. *Solar Phys.*, 100(1-2):563–574, 1985b. doi: 10.1007/BF00158445.

B. V. Jackson and P. P. Hick. Corotational tomography of heliospheric features using global thomson scattering data. *Solar Phys.*, 211(1):345–356, 2002. doi: 10.1023/A:1022409530466.

B. V. Jackson and C. H. Leinert. Helios images of solar mass ejections. *J. Geophys. Res.*, 90(A11):10759–10764, 1985. doi: 10.1029/JA090iA11p10759.

B. V. Jackson, A. Buffington, P. P. Hick, X. Wang, and D. Webb. Preliminary three-dimensional analysis of the heliospheric response to the 28 October 2003 cme using SMEI white-light observations. *J. Geophys. Res.*, 111(A4), 2006. doi: 10.1029/2004JA010942.

B. V. Jackson, P. P. Hick, A. Buffington, M. M. Bisi, J. M. Clover, M. Tokumaru, M. Kojima, and K. Fujiki. Three-dimensional reconstruction of heliospheric structure using iterative tomography: A review. *J. Atmos. Solar-Terr. Phys.*, 73(10):1214–1227, 2011. doi: 10.1016/j.jastp.2010.10.007.

P. Janardhan, V. Balasubramanian, S. Ananthakrishnan, M. Dryer, A. Bhatnagar, and P. S. McIntosh. Travelling interplanetary disturbances detected using interplanetary scintillation at 327 MHz. *Solar Phys.*, 166(2):379–401, 1996. doi: 10.1007/BF00149405.

L. Jian, C. T. Russell, J. G. Luhmann, and R. M. Skoug. Properties of stream interactions at one AU during 1995–2004. *Solar Phys.*, 239(1-2):337–392, 2006a. doi: 10.1007/s11207-006-0132-3.

L. Jian, C. T. Russell, J. G. Luhmann, and R. M. Skoug. Properties of interplanetary coronal mass ejections at one AU during 1995–2004. *Solar Phys.*, 239(1-2):393–436, 2006b. doi: 10.1007/s11207-006-0133-2.

S. Kahler. The morphological and statistical properties of solar X-ray events with long decay times. *Astrophys. J.*, 214:891–897, 1977. doi: 10.1086/155319.

M. L. Kaiser, T. A. Kucera, J. M. Davila, O. C. St. Cyr, M. Guhathakurta, and E. Christian. The STEREO mission: An introduction. In *The STEREO Mission*, pages 5–16. Springer, 2008.

T. Kakinuma, H. Washimi, and M. Kojima. On the analysis of the observations of interplanetary scintillations obtained with three spaced receivers. *Pub. Astron. Soc. Japan*, 25:271–280, 1973.

M. Kojima and T. Kakinuma. Solar cycle dependence of global distribution of solar wind speed. *Space Sci. Rev.*, 53(3):173–222, 1990. doi: 10.1007/BF00212754.

M. Kojima, Y. Ishida, K. Maruyama, and T. Kakinuma. An observation system of interplanetary scintillation at UHF. *Proc. Res. Inst. Atmos. Nagoya Univ.*, 29:61–83, 1982.

M. Kojima, K. Fujiki, T. Ohmi, M. Tokumaru, A. Yokobe, and K. Hakamada. Low-speed solar wind from the vicinity of solar active regions. *J. Geophys. Res.*, 104(A8): 16993–17003, 1999. doi: 10.1029/1999JA900177.

M. J. Koomen, C. R. Detwiler, G. E. Brueckner, H. W. Cooper, and R. Tousey. White light coronagraph in OSO-7. *Applied Optics*, 14(3):743–751, 1975.

R. A. Kopp and G. W. Pneuman. Magnetic reconnection in the corona and the loop prominence phenomenon. *Solar Phys.*, 50(1):85–98, 1976.

A. S. Krieger, A. F. Timothy, and E. C. Roelof. A coronal hole and its identification as the source of a high velocity solar wind stream. *Solar Phys.*, 29(2):505–525, 1973. doi: 10.1007/BF00150828.

P. K. Kundu, I. M. Cohen, and D. R. Dowling. *Fluid Mechanics Fifth Edition*. Elsevier Academic Press, Waltham, 2012. ISBN 978-0-12-382100-3.

A. Lara, A. Flandes, A. Borgazzi, P. Subramanian, and C. U. México. Velocity profile of interplanetary coronal mass ejections beyond 1 AU. *J. Geophys. Res.*, 116(A15): 12102, 2011. doi: 10.1029/2011JA016807.

A. J. Lazarus, K. W. Ogilvie, and L. F. Burlaga. Interplanetary shock observations by Mariner 5 and Explorer 34. *Solar Phys.*, 13(1):232–239, 1970. doi: 10.1007/BF00963957.

G. M. Lindsay, J. G. Luhmann, C. T. Russell, and J. T. Gosling. Relationships between coronal mass ejection speeds from coronagraph images and interplanetary characteristics of associated interplanetary coronal mass ejections. *J. Geophys. Res.*, 104(A6): 12515–12, 1999. doi: 10.1029/1999JA900051.

B. C. Low. Coronal mass ejections, magnetic flux ropes, and solar magnetism. *J. Geophys. Res.*, 106(A11):25141–25163, 2001. doi: 10.1029/2000JA004015.

R. Lüst. Aktivität von kometenschweifen in perioden geomagnetischer ruhe. *Z. Astrophys.*, 51:163–176, 1961.

R. Lüst. Beobachtungen am Kometen Abell 1953 g im zusammenhang mit dem solaren wind. *Z. Astrophys.*, 57:192–196, 1963.

B. J. Lynch, Y. Li, A. F. R. Thernisien, E. Robbrecht, G. H. Fisher, J. G. Luhmann, and A. Vourlidas. Sun to 1 AU propagation and evolution of a slow streamer-blowout coronal mass ejection. *J. Geophys. Res.*, 115(A7):A07106, 2010. doi: 10.1029/2009JA015099,2010.

B. Lyot. Planetary and solar observations on the pic du midi in 1941, 1942, and 1943. *Astrophys. J.*, 101:255, 1945. doi: 10.1086/144713.

R. M. MacQueen and R. R. Fisher. The kinematics of solar inner coronal transients. *Solar Phys.*, 89(1):89–102, 1983. doi: 10.1007/BF00211955.

R. M. MacQueen, J. A. Eddy, J. T. Gosling, E. Hildner, R. H. Munro, G. A. Newkirk, Jr., A. I. Poland, and C. L. Ross. The outer solar corona as observed from Skylab: Preliminary results. *Astrophys. J. Lett.*, 187:L85, 1974. doi: 10.1086/181402.

R. M. MacQueen, A. Csoeke-Poeckh, E. Hildner, L. House, R. Reynolds, A. Stanger, H. Tepoel, and W. Wagner. The high altitude observatory Coronagraph/Polarimeter on the Solar Maximum Mission. *Solar Phys.*, 65:91–107, 1980. doi: 10.1007/BF00151386.

S. A. Maloney and P. T. Gallagher. Solar wind drag and the kinematics of interplanetary coronal mass ejections. *Astrophys. J. Lett.*, 724:L127, 2010. doi: 10.1088/2041-8205/724/2/L127.

P. K. Manoharan. Evolution of coronal mass ejections in the inner heliosphere: A study using white-light and scintillation images. *Solar Phys.*, 235(1):345–368, 2006. doi: 10.1007/s11207-006-0100-y.

P. K. Manoharan. Ooty interplanetary scintillation–remote-sensing observations and analysis of coronal mass ejections in the heliosphere. *Solar Phys.*, 265(1):137–157, 2010. doi: 10.1007/s11207-010-9593-5.

P. K. Manoharan and S. Ananthakrishnan. Determination of solar-wind velocities using single-station measurements of interplanetary scintillation. *Mon. Not. Roy. Astron. Soc.*, 244:691–695, 1990.

P. K. Manoharan and A. Mujiber Rahman. Coronal mass ejections–Propagation time and associated internal energy. *J. Atmos. Solar-Terr. Phys.*, 73(5-6):671–677, 2011. doi: 10.1016/j.jastp.2011.01.017.

P. K. Manoharan, M. Kojima, N. Gopalswamy, T. Kondo, and Z. Smith. Radial evolution and turbulence characteristics of a coronal mass ejection. *Astrophys. J.*, 530:1061, 2000. doi: 10.1086/308378.

P. K. Manoharan, M. Tokumaru, M. Pick, P. Subramanian, F. M. Ipavich, K. Schenk, M. L. Kaiser, R. P. Lepping, and A. Vourlidas. Coronal mass ejection of 2000 July 14 flare event: Imaging from near-sun to earth environment. *Astrophys. J.*, 559: 1180–1189, 2001. doi: 10.1086/322332.

E. W. Maunder. Magnetic disturbances, 1882 to 1903, as recorded at the Royal Observatory, Grreenwich, and their association with sun-spots. *Mon. Not. Roy. Astron. Soc.*, 65(1):2–18, 1904a. doi: 10.1093/mnras/65.1.2.

E. W. Maunder. Demonstration of the solar origin of the magnetic disturbances. *Mon. Not. Roy. Astron. Soc.*, 65(1):18–34, 1904b. doi: 10.1093/mnras/65.1.18.

D. J. McComas, S. J. Bame, P. Barker, W. C. Feldman, J. L. Phillips, P. Riley, and J. W. Griffee. Solar wind electron proton alpha monitor (SWEPAM) for

the Advanced Composition Explorer. *Space Sci. Rev.*, 86(1):563–612, 1998. doi: 10.1023/A:1005040232597.

J. C. Mejia-Ambriz, P. Villanueva-Hernandez, J. A. Gonzalez-Esparza, E. Aguilar-Rodriguez, and S. Jeyakumar. Observations of interplanetary scintillation (IPS) using the Mexican Array Radio Telescope (MEXART). *Solar Phys.*, 265(1-2):309–320, 2010. doi: 10.1007/s11207-010-9562-z.

N. Meyer-Vernet. *Basics of the Solar Wind*. Cambridge University Press, New York, 2007.

G. Michalek, N. Gopalswamy, and S. Yashiro. A new method for estimating widths, velocities, and source location of halo coronal mass ejections. *Astrophys. J.*, 584:472, 2003. doi: 10.1086/345526.

S. Miyamoto. Ionization theory of solar corona. *Pub. Astron. Soc. Japan*, 1:10–13, 1949.

Y.-J. Moon, G. S. Choe, H. Wang, Y. D. Park, N. Gopalswamy, G. Yang, and S. Yashiro. A statistical study of two classes of coronal mass ejections. *Astrophys. J.*, 581(1): 694–702, 2002. doi: 10.1086/344088.

T. C. Mouschovias and A. I. Poland. Expansion and broadening of coronal loop transients - A theoretical explanation. *Astrophys. J.*, 220:675–682, 1978. doi: 10.1086/155951.

R. H. Munro and G. L. Withbroe. Properties of a coronal "hole" derived from extreme-ultraviolet observations. *Astrophys. J.*, 176:511–520, 1972. doi: 10.1086/151653.

R. H. Munro, J. T. Gosling, E. Hildner, R. M. MacQueen, A. I. Poland, and C. L. Ross. The association of coronal mass ejection transients with other forms of solar activity. *Solar Phys.*, 61(1):201–215, 1979.

M. Neugebauer. Large-scale and solar-cycle variations of the solar wind. *Space Sci. Rev.*, 17(2):221–254, 1975. doi: 10.1007/BF00718575.

M. Neugebauer and C. W. Snyder. Solar plasma experiment. *Science*, 138(3545): 1095–1097, 1962.

M. Neugebauer and C. W. Snyder. Mariner 2 observations of the solar wind: 1. Average properties. *J. Geophys. Res.*, 71(19):4469–4484, 1966.

H. W. Newton. Solar flares and magnetic storms. *Mon. Not. Roy. Astron. Soc.*, 103: 244–257, 1943. doi: 10.1093/mnras/103.5.244.

K. W. Ogilvie, D. J. Chornay, R. J. Fritzenreiter, F. Hunsaker, J. Keller, J. Lobell, G. Miller, J. D. Scudder, E. C. Sittler, R. B. Torbert, et al. SWE, a comprehensive plasma instrument for the Wind spacecraft. *Space Sci. Rev.*, 71(1):55–77, 1995. doi: 10.1007/BF00751326.

V. Ontiveros and A. Vourlidas. Quantitative measurements of coronal mass ejection-driven shocks from LASCO observations. *Astrophys. J.*, 693:267, 2009. doi: 10.1088/0004-637X/693/1/267.

E. N. Parker. Dynamics of the interplanetary gas and magnetic fields. *Astrophys. J.*, 128:664–676, 1958a. doi: 10.1086/146579.

E. N. Parker. Interaction of the solar wind with the geomagnetic field. *Phys. Fluids*, 1: 171–187, 1958b. doi: 10.1063/1.1724339.

E. N. Parker. Sudden expansion of the corona following a large solar flare and the attendant magnetic field and cosmic-ray effects. *Astrophys. J.*, 133:1014, 1961. doi: 10.1086/147105.

K. I. Paularena and J. H. King. NASA's IMP 8 spacecraft. In D. G. Sibeck and K. Kudela, editors, *Interball in the ISTP Program*, volume 537 of *NATO Science Series*, pages 145–154. Springer, 1999. doi: 10.1007/978-94-011-4487-2_11.

S. Pintér. Experimental study of flare-generated collisionless interplanetary shock wave propagation. *Space Sci. Rev.*, 32(1-2):145–168, 1982. doi: 10.1007/BF00225182.

V. Pizzo. A three-dimensional model of corotating streams in the solar wind, 1. Theoretical foundations. *J. Geophys. Res.*, 83(A12):5563–5572, 1978.

A. I. Poland, R. A. Howard, M. J. Koomen, D. J. Michels, and N. R. Sheeley, Jr. Coronal transients near sunspot maximum. *Solar Phys.*, 69(1):169–175, 1981. doi: 10.1007/BF00151264.

M. J. Reiner, M. L. Kaiser, and J. L. Bougeret. On the deceleration of cmes in the corona and interplanetary medium deduced from radio and white-light observations. *Solar Wind Ten: Proceedings of the Tenth International Solar Wind Conference*, 679: 152, 2003.

M. J. Reiner, M. L. Kaiser, and J. L. Bougeret. Coronal and interplanetary propagation of cme/shocks from radio, in situ and white-light observations. *Astrophys. J.*, 663: 1369, 2007. doi: 10.1086/518683.

I. G. Richardson and H. V. Cane. Identification of interplanetary coronal mass ejections at 1 AU using multiple solar wind plasma composition anomalies. *J. Geophys. Res.*, 109:A09104, 2004. doi: 10.1029/2004JA010598.

I. G. Richardson and H. V. Cane. Near-earth interplanetary coronal mass ejections during solar cycle 23 (1996–2009): Catalog and summary of properties. *Solar Phys.*, 264(1):189–237, 2010. doi: 10.1007/s11207-010-9568-6.

B. J. Rickett. Disturbances in the solar wind from IPS measurements in August 1972. *Solar Phys.*, 43(1):237–247, 1975. doi: 10.1007/BF00155155.

T. Rollett, C. Möstl, M. Temmer, A. M. Veronig, C. J. Farrugia, and H. K. Biernat. Constraining the kinematics of coronal mass ejections in the inner heliosphere with in-situ signatures. *Solar Phys.*, pages 1–22, 2012. doi: 10.1007/s11207-011-9897-0.

T. Sakao, R. Kano, N. Narukage, J. Kotoku, T. Bando, E. E. DeLuca, L. L. Lundquist, S. Tsuneta, L. K. Harra, Y. Katsukawa, et al. Continuous plasma outflows from the edge of a solar active region as a possible source of solar wind. *Science*, 318(5856): 1585–1588, 2007. doi: 10.1126/science.1147292.

G. Schubert and W. D. Cummings. The double shock wave structure in the solar wind. *J. Geophys. Res.*, 72(21):5275–5286, 1967. doi: 10.1029/JZ072i021p05275.

R. Schwenn. Direct correlations between coronal transients and interplanetary disturbances. *Space Sci. Rev.*, 34(1):85–99, 1983. doi: 10.1007/BF00221199.

R. Schwenn, K.H. Mühlhäuser, E. Marsch, and H. Rosenbauer. Two states of the solar wind at the time of solar activity minimum, II, Radial gradient of plasma parameters in fast and slow streams. In H. Rosenbauer, editor, *Solar Wind Four*, pages 126–130, Katlenburg-Lindau, 1981. Max-Plank-Institute für Aeronomie.

A. Shanmugaraju, Y.-J. Moon, B. Vrsnak, and D. Vrbanec. Radial evolution of well-observed slow cmes in the distance range 2–30 $R_{\odot}$. *Solar Phys.*, 257(2):351–361, 2009. doi: 10.1007/s11207-009-9379-9.

L. E. Sharp and D. E. Harris. Enhanced interplanetary scintillations associated with solar flares. *Nature*, 213:377–378, 1967. doi: 10.1038/213377a0.

N. R. Sheeley, Jr., J. W. Harvey, and W. C. Feldman. Coronal holes, solar wind streams, and recurrent geomagnetic disturbances: 1973–1976. *Solar Phys.*, 49(2):271–278, 1976.

N. R. Sheeley, Jr., R. A. Howard, M. J. Koomen, and D. J. Michels. Associations between coronal mass ejections and soft X-ray events. *Astrophys. J.*, 272:349–354, 1983. doi: 10.1086/161298.

N. R. Sheeley, Jr., Y.-M. Wang, S. H. Hawley, G. E. Brueckner, K. P. Dere, R. A. Howard, M. J. Koomen, C. M. Korendyke, D. J. Michels, S. E. Paswaters, et al. Measurements of flow speeds in the corona between 2 and 30 $R_{\odot}$. *Astrophys. J.*, 484 (1):472, 1997. doi: 10.1086/304338.

C. Shen, Y. Wang, B. Gui, P. Ye, and S. Wang. Kinematic evolution of a slow cme in corona viewed by STEREO-B on 8 October 2007. *Solar Phys.*, 269(2):389–400, 2011. doi: 10.1007/s11207-011-9715-8.

K. Shibata and T. Magara. Solar flares: magnetohydrodynamic processes. *Living Rev. Solar Phys.*, 8:6, 2011. doi: 10.12942/lrsp-2011-6. URL http://www.livingreviews.org/lrsp-2011-6.

D. Shiota, H. Isobe, P. F. Chen, T. Yamamoto, T. Sakajiri, and K. Shibata. Self-consistent magnetohydrodynamic modeling of a coronal mass ejection, coronal dimming, and a giant cusp-shaped arcade formation. *Astrophys. J.*, 634(1):663–678, 2005.

D. Shiota, R. Kataoka, Y. Miyoshi, and C. Tao. Development of automatic daily MHD simulation of solar wind and coronal mass ejections in inner heliosphere. In *Japan Geoscience Union Meeting 2013*, number PEM05-38 in JpGU Meeting, 2013. URL www2.jpgu.org/meeting/2013/session/PDF/P-EM05/PEM05-38_E.pdf.

G. L. Siscoe. Structure and orientations of solar-wind interaction fronts: Pioneer 6. *J. Geophys. Res.*, 77(1):27–34, 1972. doi: 10.1029/JA077i001p00027.

S. F. Smerd and G. A. Dulk. 80 MHz radioheliograph evidence on moving type IV bursts and coronal magnetic fields. In R. Howard, editor, *Solar Magnetic Fields*, volume 43 of *IAU Symposium*, page 616, 1971.

E. J. Smith and J. H. Wolfe. Observations of interaction regions and corotating shocks between one and five AU: Pioneers 10 and 11. *Geophys. Res. Lett.*, 3(3):137–140, 1976. doi: 10.1029/GL003i003p00137.

C. P. Sonett, D. S. Colburn, L. Davis, Jr., E. J. Smith, and P. J. Coleman. Jr. Evidence for a collision-free magnetohydrodynamic shock in interplanetary space. *Phys. Rev. Lett.*, 13(5):153–156, 1964. doi: 10.1103/PhysRevLett.13.153.

L. Spitzer, Jr. The dynamics of the interstellar medium. I. Local equilibrium. *Astrophys. J.*, 93:369–379, 1941. doi: 10.1086/144273.

E.C. Stone, A.M. Frandsen, R.A. Mewaldt, E.R. Christian, D. Margolies, J.F. Ormes, and F. Snow. The Advanced Composition Explorer. *Space Sci. Rev.*, 86(1):1–22, 1998. doi: 10.1023/A:1005082526237.

P. A. Sturrock. Model of the high-energy phase of solar flares. *Nature*, 211:695–697, 1966. doi: 10.1038/211695a0.

Z. Švestka and E. W. Cliver. History and basic characteristics of eruptive flares. In Z. Švestka, B. V. Jackson, and M. E. Machado, editors, *Eruptive Solar Flares*, volume 399 of *Lecture Notes in Physics*, pages 1–11. Springer, 1992. doi: 10.1007/3-540-55246-4_70.

G. Swarup, N. V. G. Sarma, M. N. Joshi, V. K. Kapahi, D. S. Bagri, S. H. Damle, S. Ananthakrishnan, V. Balasubramanian, S. S. Bhave, and R. P. Sinha. Large steerable radio telescope at ootacamund, India. *Nat. Phys. Sci.*, 230:185–188, 1971. doi: 10.1038/physci230185a0.

P. A. Sweet. Mechanisms of solar flares. *Ann. Rev. Astron. Astrophys.*, 7:149–176, 1969. doi: 10.1146/annurev.aa.07.090169.001053.

E. Tandberg-Hanssen, S. F. Martin, and R. T. Hansen. Dynamics of flare sprays. *Solar Phys.*, 65(2):357–368, 1980. doi: 10.1007/BF00152799.

S. J. Tappin. *Transient disturbances in the solar wind.* PhD thesis, University of Cambridge, 1984.

S. J. Tappin. The deceleration of an interplanetary transient from the sun to 5 AU. *Solar Phys.*, 233(2):233–248, 2006. doi: 10.1007/s11207-006-2065-2.

S. J. Tappin, A. Hewish, and G. R. Gapper. Tracking a major interplanetary disturbance. *Planet. Space Sci.*, 31(10):1171–1176, 1983. doi: 10.1016/0032-0633(83)90106-X.

M. Temmer, T. Rollett, C. Möstl, A.M. Veronig, B. Vršnak, and D. Odstrčil. Influence of the ambient solar wind flow on the propagation behavior of interplanetary coronal mass ejections. *Astrophys. J.*, 743(2):101, 2011. doi: 10.1088/0004-637X/743/2/101.

B. T. Thomas and E. J. Smith. The structure and dynamics of the heliospheric current sheet. *J. Geophys. Res.*, 86(A13):11105–11110, 1981. doi: 10.1029/JA086iA13p11105.

M. Tokumaru, M. Kojima, K. Fujiki, and A. Yokobe. Three-dimensional propagation of interplanetary disturbances detected with radio scintillation measurements at 327 MHz. *J. Geophys. Res.*, 105:10, 2000a. doi: 10.1029/2000JA900001.

M. Tokumaru, M. Kojima, Y. Ishida, A. Yokobe, and T. Ohmi. Large-scale structure of solar wind turbulence near solar activity minimum. *Adv. Space Res.*, 25(9):1943–1946, 2000b. doi: 10.1016/S0273-1177(99)00630-4.

M. Tokumaru, M. Kojima, K. Fujiki, M. Yamashita, and A. Yokobe. Toroidal-shaped interplanetary disturbance associated with the halo coronal mass ejection event on 14 July 2000. *J. Geophys. Res.*, 108:1220, 2003. doi: 10.1029/2002JA009574.

M. Tokumaru, M. Kojima, K. Fujiki, and M. Yamashita. Tracking heliospheric disturbances by interplanetary scintillation. *Nonlin. Processes Geophys.*, 13(3):329–338, 2006.

M. Tokumaru, M. Kojima, K. Fujiki, K. Maruyama, Y. Maruyama, H. Ito, and T. Iju. A newly developed UHF radiotelescope for interplanetary scintillation observations: Solar Wind Imaging Facility. *Radio Sci.*, 46(null):RS0F02, 2011. doi: 10.1029/2011RS004694.

R. Tousey. The solar corona. In M. J. Rycroft and S. K. Runcorn, editors, *Space Research Conference*, pages 713–730, 1973.

R. Tousey, R. A. Howard, and M. J. Koomen. The frequency and nature of coronal transient events observed by OSO-7. In *Bulletin of the American Astronomical Society*, volume 6 of *Bulletin of the American Astronomical Society*, page 295, 1974.

B. T. Tsurutani, W. D. Gonzalez, F. Tang, S. I. Akasofu, and E. J. Smith. Origin of interplanetary southward magnetic fields responsible for major magnetic storms near solar maximum (1978–1979). *J. Geophys. Res.*, 93(A8):8519–8531, 1988. doi: 10.1029/JA093iA08p08519.

A. A. van Ballegooijen and P. C. H. Martens. Formation and eruption of solar prominences. *Astrophys. J.*, 343:971–984, 1989. doi: 10.1086/167766.

V. V. Vitkevich and V. I. Vlasov. Radioastronomical investigations of the drift of the inhomogeneous interplanetary plasma. *Soviet Astron.*, 13:669, 1970.

V. V. Vitkevich, A. A. Glushaev, Y. P. Ilyasov, S. M. Kutuzov, A. D. Kuz'min, I. A. Alekseev, V. D. Bunin, G. F. Novozhenov, G. A. Pavlov, N. S. Solomin, et al. Antenna-A perture complex of the VLPA FIAN radio telescope. *Radiophys. Quantum Electr.*, 19(11):1107–1115, 1976.

V. I. Vlasov. Velocity of interplanetary shock waves according to radioastronomical data. *Geomagn. Aèron.*, 28(1):1–8, 1988.

V. I. Vlasov. Travelling interplanetary disturbances from radioastronomical data. In E. Marsch and R. Schwenn, editors, *Solar Wind Seven; Proc. 3rd COSPAR*, volume 1, pages 301–310, New York, 1992. Pergamon.

A. Vourlidas, P. Subramanian, K. P. Dere, and R. A. Howard. Large-angle spectrometric coronagraph measurements of the energetics of coronal mass ejections. *Astrophys. J.*, 534(1):456–467, 2000. doi: 10.1086/308747.

A. Vourlidas, D. Buzasi, R. A. Howard, and E. Esfandiari. Mass and energy properties of LASCO CMEs. In A. Wilson, editor, *Solar Variability: From Core to Outer Frontiers,ESA SP-506*, volume 506, pages 91–94, Noordwijk, 2002.

A. Vourlidas, B. J. Lynch, R. A. Howard, and Y. Li. How many cmes have flux ropes? deciphering the signatures of shocks, flux ropes, and prominences in coronagraph observations of cmes. *Solar Phys.*, pages 1–23, 2012. doi: 10.1007/s11207-012-0084-8.

B. Vršnak. Dynamics of solar coronal eruptions. *J. Geophys. Res.*, 106(A11):25249–25259, 2001a. doi: 10.1029/2000JA004007.

B. Vršnak. Deceleration of coronal mass ejections. *Solar Phys.*, 202(1):173–189, 2001b. doi: 10.1023/A:1011833114104.

B. Vršnak and N. Gopalswamy. Influence of the aerodynamic drag on the motion of interplanetary ejecta. *J. Geophys. Res.*, 107:1019, 2002. doi: 10.1029/2001JA000120.

B. Vršnak, T. Žic, T.V. Falkenberg, C. Möstl, S. Vennerstrom, and D. Vrbanec. The role of aerodynamic drag in propagation of interplanetary coronal mass ejections. *Astron. Astrophys.*, 512, 2010. doi: 10.1051/0004-6361/200913482.

B. Vršnak, T. Žic, D. Vrbanec, M. Temmer, T. Rollett, C. Möstl, A. Veronig, J. Čalogović, M. Dumbović, S. Lulić, et al. Propagation of interplanetary coronal mass ejections: the drag-based model. *Solar Phys.*, 285:295–315, 2013. doi: 10.1007/s11207-012-0035-4.

B. D. Ward. Interplanetary scintillation and flare-produced disturbances. *Proc. Astron. Soc. Aust.*, 2:378–379, 1975.

T. Watanabe and T. Kakinuma. Radio-scintillation observations of interplanetary disturbances. *Adv. Space Res.*, 4(7):331–341, 1984.

T. Watanabe and T. Kakinuma. Three-dimensional properties of interplanetary disturbances in 1978–1981. *Astrophys. Space Sci.*, 118(1):153–157, 1986. doi: 10.1007/BF00651120.

T. Watanabe and R. Schwenn. Large-scale propagation properties of interplanetary disturbances revealed from ips and spacecraft observations. *Space Sci. Rev.*, 51(1):147–173, 1989. doi: 10.1007/BF00226272.

T. Watanabe, T. Kakinuma, M. Kojima, and R. Schwenn. Large-scale propagation properties of an interplanetary disturbance in association with a “halo” coronal mass ejection on 27 november 1979. *Proc. Res. Inst. Atmos. Nagoya Univ.*, 36:11–28, 1989.

D. F. Webb and A. J. Hundhausen. Activity associated with the solar origin of coronal mass ejections. *Solar Phys.*, 108(2):383–401, 1987. doi: 10.1007/BF00214170.

F. L. Whipple and J. L. Gossner. An upper limit to the electron density near the Earth's orbit. *Astrophys. J.*, 109:380–390, 1949.

J. M. Wilcox. The interplanetary magnetic field. Solar origin and terrestrial effects. *Space Sci. Rev.*, 8(2):258–328, 1968.

R. F. Wimmer-Schweingruber, N. U. Crooker, A. Balogh, V. Bothmer, R. J. Forsyth, P. Gazis, J. T. Gosling, T. Horbury, A. Kilchenmann, I. G. Richardson, et al. Understanding interplanetary coronal mass ejection signatures. In H. Kunow, N. U. Crooker, J. A. Linker, R. Schwenn, and R. Von Steiger, editors, *Coronal Mass Ejections*, volume 21 of *Space Sciences Series of ISSI*, pages 177–216, Dordrecht, 2006. Springer. doi: 10.1007/978-0-387-45088-9_10.

M. Wiseman and P. A. Dennison. Flare induced shocks and corotating streams in the interplanetary medium. *Proc. Astron. Soc. Aust.*, 2:79–81, 1972.

G. L. Withbroe and R. W. Noyes. Mass and energy flow in the solar chromosphere and corona. *Ann. Rev. Astron. Astrophys.*, 15:363–387, 1977. doi: 10.1146/annurev.aa.15.090177.002051.

J. H. Wolfe, R. W. Silva, and M. A. Myers. Observations of the solar wind during the flight of IMP 1. *J. Geophys. Res.*, 71(5):1319–1340, 1966.

R. Woo. A synoptic study of doppler scintillation transients in the solar wind. *J. Geophys. Res.*, 93(A5):3919–3926, 1988. doi: 10.1029/JA093iA05p03919.

K. Wurm. Structure and kinematics of cometary type I tails. *Icarus*, 8(1):287–300, 1968.

M. Yamashita, M. Tokumaru, and M. Kojima. Radial dependence of propagation speed of solar wind disturbance. In M. Velli, R. Bruno, and F. Malara, editors, *The Tenth International Solar Wind Conference, AIP Conf. Proc.*, volume 679, pages 754–757, New York, 2003. AIP Publishing LLC. doi: 10.1063/1.1618702.

S. Yashiro, N. Gopalswamy, G. Michalek, O.C. St. Cyr, S.P. Plunkett, N.B. Rich, and R.A. Howard. A catalog of white light coronal mass ejections observed by the soho spacecraft. *J. Geophys. Res.*, 109:A07105, 2004. doi: 10.1029/2003JA010282.

A.T. Young. Interpretation of interplanetary scintillations. *Astrophys. J.*, 168:543, 1971. doi: 10.1086/151108.

List of Publications

T. Iju, M. Tokumaru, and K. Fujiki. Kinematics of interplanetary coronal mss ejections in the inner heliosphere. In G. P. Zank, J. Borovsky, R. Bruno, J. Cirtain, S. Cranmer, H. Elliott, J. Giacalone, W. Gonzalez, G. Li, E. Marsch, E. Moebius, N. Pogorelov, J. Spann, and O. Verkhoglyadova, editors, *The Thirteenth International Solar Wind Conference, AIP Conf. Proc.*, volume 1539, pages 183–186, New York, 2013a. AIP Publishing LLC. doi: 10.1063/1.4811018.

T. Iju, M. Tokumaru, and K. Fujiki. Radial speed evolution of coronal mass ejections during solar cycle 23. *Solar Phys.*, 288(1):331–353, 2013b. doi: 10.1007/s11207-013-0297-5.

T. Iju, M. Tokumaru, and K. Fujiki. Kinematic properties of slow icmes and an interpretation of a modified drag equation for fast and moderate icmes. *Solar Phys.*, 289(6):2157–2175, 2014. doi: 10.1007/s11207-014-0472-3.